Spring 5-15-2023

Spectro-Polarimetric and Time Domain Characteristics of Dynamically Evolving Accretion Flows from the General Relativistic Raytracing of General Relativistic Magneto-Hydrodynamical Simulations

Andrew West

WASHINGTON UNIVERSITY IN ST. LOUIS
DEPARTMENT OF PHYSICS

Dissertation Examination Committee:
Henric Krawczynski, Chair
Ramanath Cowsik, Co-Chair
Michael Nowak
James Steiner
Yajie Yuan

Spectro-Polarimetric and Time Domain Characteristics of Dynamically Evolving Accretion Flows from the General Relativistic Raytracing of General Relativistic Magneto-Hydrodynamical Simulations

by
Andrew Thomas West

A dissertation presented to
Washington University in St. Louis
partial fullfillment of the
requirements for the degree
of Doctor of Philosophy

St. Louis, Missouri
May 2023

Contents

List of Figures

List of Tables

Acknowledgements

I am fortunate to have a wealth of close friends and family who have contributed to my success over the course of many years. The list is too long to name them all here.

First and foremost I need to thank my advisor Henric Krawczynski, without whom this work would not be possible. Henric has shown me the patience of a mountain range as I have molded myself from a blunt instrument into something more refined and purposeful. He has provided me with more opportunities to learn and grow as a scientist, a thinker, a teacher, a leader, and a human being than I could have ever asked for. There are not words or numbers that can adequately convey my gratitude to him for the trust he has placed in me and the experiences he has made possible for me.

Next on the list is Fabian Kislat, without whom I would not even know how to spell c^{++}. Fabian has taught me the value of clean code and that complexity is sometimes a necessity. Most of all, he has taught me by his own example the value in taking a step back so that someone else can lead the way, even if - perhaps especially if - you already know the fastest way to get there. I undoubtedly owe thanks to the entire XL-Calibur team. Although none of my work related to XL-Calibur is contained in this thesis, being a part of this collaboration has been one of most rewarding (and challenging) experiences of my life. I need to thank Matthew Liska for trusting me with leading the project contained in this thesis, for his incredible patience as I have taken my time quintuple checking everything, and for the numerous opportunities he has catalyzed for me. I would like to thank Mike Nowak and Jack Steiner, who have both individually gone out of their way to expose me to new people and my work to broader audiences, to share their analytical expertise (which was instrumental to the completion of the work in this thesis), and for being real humans and treating me like a peer. I'd also like to thank the McDonnell Center for the Space Sciences

at Washington University in St. Louis, without whose financial support these works would not have been possible.

I'd like to thank Brian Rauch for his friendship, his support, and for providing me with opportunities to step into extraordinary situations. I've known very few people who so consistently do the right thing regardless of the cost, and the example you have set has made me a better person. I am grateful to my peers, without whom I would not have survived the first few years of graduate school. In no particular order - Dawson Huth, Kiandokht Amiri, Wolfgang von Zober, Arman Hossen, Jonah Hoffman, Ali Arra, Luis Perez, Chen Hao Lin, Nicole Rodriguez, Quin Abarr, Banafsheh Beheshtipour, Ephraim Gau, Yashika Kapoor, Maryam Abassi, Natalia Calleya, Augusto Medeiros da Rosa, and Furqan Dar. I am especially grateful to Lindsey Lisalda, for often being the voice of reason and for showing me grace.

I want to thank Sean Grover for leading by example and encouraging me to always do the hard things. I am not sure I would have been able to get back in the game without your support, and I'll never be able to thank you enough for that. I need to thank Acadia Reynolds, who has shown me unwavering support and patience. Acadia has always encouraged me to do the most, even when that meant months long absences from home. She has endured me in every state I can exist in, and by proxy has sacrificed as I have sacrificed for this experience, and she has never once complained. I hope everyone alive finds a partner and friend like you, for you give this Universe meaning. I also need to thank my sister, Kelli West, for always believing in me and always supporting me. From a very young age you encouraged me to embrace myself and to pursue that which stirs me most. Your steadfast spirit, humility, sense of self, and fearlessness inspire me every single day, and I become a better man every time I am in your presence. I must also thank Sophie West, who taught me patience, how to enjoy the simple things in life, and showed me that being kind and

doing good do not always mean talking softly. I wish you were here to see me now. I also must thank my parents, who fostered my creativity and curiosity from a very young age. In particular I would like to thank my father Craig, who may not have understood why I set the goals that I did but never stopped supporting my pursuit of them.

From as far back as I can remember I have wanted to be a scientist, to know how the Universe works and to be able to hold the majesty of its truth in my head. But life often gets in the way of our goals, and things don't always progress as smoothly as one would hope. So in closing, I'd like to thank me, for not giving up on myself, for not letting the doubt take over, for choosing to do the hard things and for sacrificing what was necessary to realize this. It was worth it.

Andrew Thomas West

Washington University in St. Louis

May 2023

ABSTRACT OF THE DISSERTATION

Spectro-Polarimetric and Time Domain Characteristics of Dynamically Evolving Accretion Flows from the General Relativistic Raytracing of General Relativistic Magneto-Hydrodynamical Simulations

by

Andrew Thomas West

Doctor of Philosophy in Physics

Washington University in St.Louis, 2023

Professor Henric Krawczynski (Chair)

Black holes are among the most exotic phenomena in our universe, physical objects so dense and compact that within their horizon not even light can escape. In binary systems, black holes can accrete material from their companion star, forming an accretion disk that is subjected to extreme physical conditions. Often, these disks are accompanied by jets - highly relativistic outflows of material moving at significant fractions of the speed of light. This extreme environment is the source of some of the most luminous and energetic processes in our universe. Black hole accretion disks are often modeled as a steady state, razor thin disk aligned in the equatorial plane of the black hole spin. In reality, however, this approximation is not always valid as these systems are highly dynamic, with their energy spectra varying as the state of the accretion flow changes. These changes of state occur on timescales of days to weeks to months, during which the luminosity can increase or decrease by orders of magnitude. Simultaneously, variations in the luminosity are also observed on sub-second timescales, a phenomenon known as quasi-periodic oscillations (QPOs). While the characteristics of these state transitions and QPOs have been well typified by modern observations,

the physical mechanisms underlying them are only beginning to be understood.

This thesis contains work I have completed in to better understand and explain the observational characteristics of accretion disks which deviate from the thin disk model. In the first part of this thesis I explore the effect of finite geometric thickness on the polarization spectra produced by accreting black holes, achieved by introducing a modified geometry to the raytracing code xTrack. I find that, in general, disks of geometric thickness produce higher polarization signatures than thinner disks. The remainder of the thesis focuses on the time domain characteristics, reflection spectra, and polarization spectra of a dynamically evolving accretion disk undergoing tearing events. To achieve this, I developed a raytracing code based on xTrack that utilizes the output of the General Relativistic Magneto-Hydrodynamical simulation H-AMR as initial conditions and raytraces the spectral emission through the evolving geometry. I show, for the first time, spectral high frequency QPOs that result from tearing events in the disk itself. Additionally, I show that precession of an inner, quasi- Bardeen-Petterson aligned disk produces low frequency QPOs. I also explore the dynamic behavior of the both the polarization and Fe-Kα line emission during these tearing events. These novel results lay the groundwork for developing new methods for measuring the spin of accreting black holes and are an important step toward explaining the dynamics of the accreting plasma during the state transitions observed in stellar mass black holes.

The most beautiful thing we can experience is the mysterious. It is the source of all true art and science. He to whom the emotion is a stranger, who can no longer pause to wonder and stand wrapped in awe, is as good as dead - his eyes are closed.

—Albert Einstein

Chapter 1

Introduction

1.1 Motivation

Black holes are the most exotic and arguably the most intriguing consequence of Einstein's Theory of General Relativity [3], the result of the core collapse of very massive stars. Shortly after Einstein published his work, Karl Schwarzchild discovered the simplest black hole solution to Einstein's field equations - that of a non-rotating, charge free black hole [4]. The subtlies of this solution were not well understood until more than 40 years later. It was Finkelstein who first realized that the Schwarzchild solution described an object with an event horizon, a boundary of causality from within which all futures have the same ending: the singularity of the black hole [5, 6]. Then, in 1963, Roy Kerr [7] derived the solution of the field equations for a rotating black hole. The Kerr solution requires only two quantities to fully describe the spacetime of a rotating black hole - the mass M and the spin, a (which in conjunction give the angular momentum of the black hole).

In the years that followed, the idea of astrophysical black holes gained more traction and legitimacy, and in 1970 the first black hole candidate was discovered - Cyg X-1 [8, 9]. In the fifty years since, the list of black hole candidates has grown significantly, with 80 [10] stellar mass black holes having been discovered thanks to the advent of ever more powerful

telescopes. In 2015, the first binary black hole merger was detected with LIGO [11], providing one of the strongest confirmations to date of the validity of Einstein's Theory of General Relativity and marking the beginning of a new era of high energy astrophysics.

Accreting black holes are the brightest objects in our universe and are capable of generating emission across nearly all wavelengths, from radio, infrared, visible/UV, and up to X-rays and γ rays. The mechanisms producing the observed emission vary, but are all deeply connected to the high gravity regime produced by the black hole through the dynamism of the plasma accreting onto it. But it is not only the energy of the light produced in these systems that is of scientific interest, for nature has encoded far more subtle clues about these extreme objects in their spectra. The emission, particularly the high energy emission, is encrypted with the features of the spacetime geometry, the dynamics of the plasma, the mechanisms of emission, and the evolution of the system through polarization and long term (days/weeks/months) and short term (subsecond) variability. Understanding these extreme objects and the exotic physics that occurs in the high gravity that they produce is essential to our understanding of the universe - its origin, its fate, and humanity's place within it.

1.2 Observational Characteristics

The bulk of the work in this thesis is focused on emission from stellar mass black holes. With that in mind, emphasis will be given in the following sections to stellar mass systems, with some of the differences between stellar mass and supermassive spectra and properties being pointed out along the way.

1.2.1 Spectra

The majority of stellar mass black holes spend their lives in a state of quiescence, with luminosities well below 1% of the Eddington limit [12], though there are a few persisent emitters, notably the first black hole discovered - Cyg X-1. Periodically, transient systems erupt in violent outbursts during which their luminosities can increase by many orders of magnitude. During these outburts, stellar mass black hole spectra are characterized by two component X-ray emission consisting of 'soft' thermal emission peaking between a few hundred eV to a few keV followed by a 'hard' powerlaw component extending up to $\sim$ 100keV or more. These phases of outburst are dynamic, with the spectra varying between soft and hard emission (and some combination thereof) on very long (days/weeks/months) timescales as they cycle through different accretion states. In some cases, variation is observed on *very* short (sub-second) timescales, which will be discussed in Section 1.2.3. The long timescale variability is associated with changes of state in the accretion flow (and thus, the spectra) itself.

In the high-soft and low-soft states, the emission spectrum is dominated by a quasi-black body spectrum, peaking in stellar mass black holes at $\sim 1 - 2$keV (and in the optical/UV for supermassive black holes). As a source moves higher on the hardness scale (to the right on Figure 1.1), its spectra develop a powerlaw component characterized by a photon index Γ between 1 and 2, such that $dN/dE \propto E^{-(1+\Gamma)}$. This emission is associated with the development of a corona, a hot ($T_e \simeq 100$keV), optically thin electron dominated atmosphere. As the virial temperature of the electrons is significantly above the effective temperature of the photons thermally emitted from the disk, these photons inverse Compton scatter (Comptonize) in the corona. Provided the photon energy $\ll 4k_bT_e$ and the corona is non-relativistic ($k_bT_e \ll m_ec^2$), the rate that energy is imparted on the photons through comptonization in

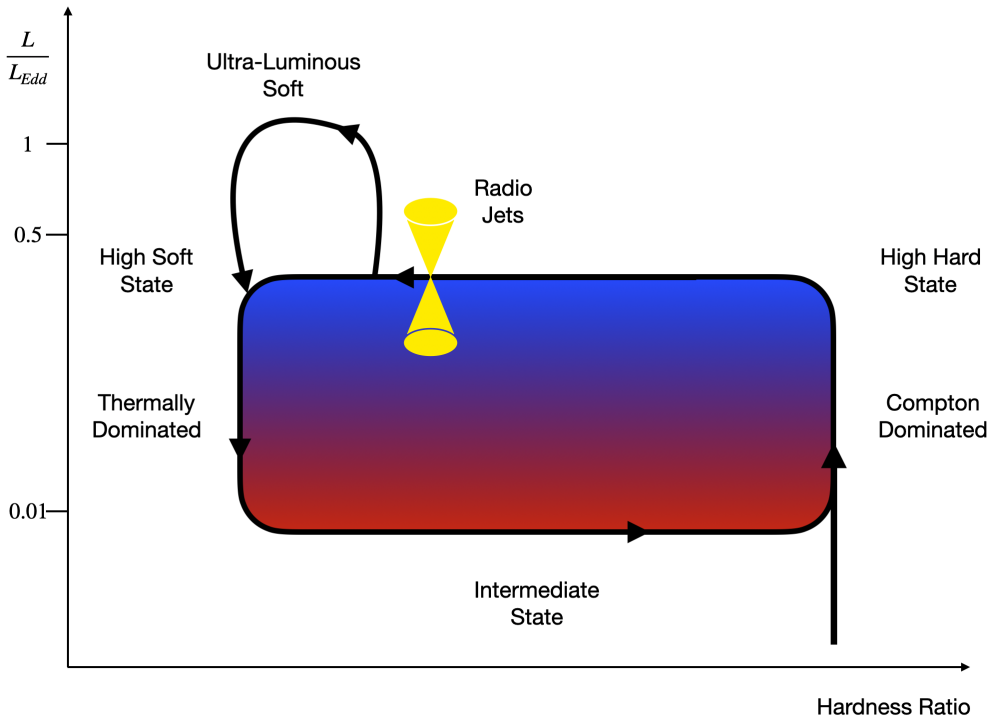

Fig. 1.1: Hardness-Intensity Diagram Adapted from [1, 2]. Sources cycle counter clockwise. As a source moves to the right, the amount of Comptonized powerlaw emission increases, and as sources move up the Luminosity increases.

the corona is given by

$$\frac{dE}{dt} = \frac{4}{3}\sigma_T c\beta^2\gamma^2 U. \tag{1.1}$$

Here, σ_t is the Thompson cross section. γ is the Lorentz factor of the electron (prior to interaction) and $\beta^2 = v_e^2/c^2$, where v_e is the velocity of the electron and c is the speed of light. Finally, U is the energy density of the incident radiation. [13]. From here, the average energy change of a single interaction, and the maximum energy change given N interactions [14, 13], is

$$\langle \Delta E \rangle = (4k_b T_e - E)\frac{E}{m_e c^2} \rightarrow E_f \simeq E_i e^{N\frac{4k_b T_e}{m_e c^2}}. \tag{1.2}$$

As photons interact and gain energy, the energy imparted from each subsequent inter-

action goes down, yielding a step cut-off in the spectra known as the power-law tail. As these high energy comptonized photons leave the corona, they may reflect back off of the disk and spur fluorescence from the cooler accreting plasma. The most notable of these fluorescence lines is the Fe-Kα line, which is relativistically broadened from its very narrow rest frame energy of 6.4keV after emission due to the orbital motion of the gas and the gravitational potential near the compact object. The Fe-Kα has become a standard benchmark for estimating black hole spin and inclination.

The geometry and location of the corona is the subject of much debate. Microlensing ([15, 16, 17]) and X-ray reverberation studies ([18, 19, 20]) of Active Galactic Nuclei (AGN) have shown that the corona is compact and located close to the black hole (within a few gravitational radii, $r_g = GM/c^2$). A 2018 study by Kara et al. using the same techniques showed the corona dynamically evolving and contracting [21], while remaining in a region very close to the black hole. These indications of compactness and close proximity to the central object have led to the corona being associated with the base of a jet, and are the source of the common 'lamppost' corona model. Recently, however, observations with the *Imaging X-Ray Polarimetry Explorer* (*IXPE*) have deviated from this jet-corona association, indicating that the corona in Cyg X-1 - at least in the state it was observed in - is spatially extended and perpendicular to the jet [22]. In reality, there is likely not one singular geometry of the corona. Long term observations of X-ray sources reveal their emission to meander from state-to-state, and the changes in both the intensity and hardness of the comptonized emission are likely to be due to the formation, evolution, and dissipation of the corona.

1.2.2 Polarization

Polarization is a measure of the alignment of the electric fields of the photons in a beam of light. In most cases, light is unpolarized - that is, all of the electric fields amongst all the photons are distributed in all directions evenly. There are many processes that will polarize an otherwise unpolarized beam of light, the most common of which, and the only process that will be addressed in this thesis, is scattering. When light scatters off of a surface, it is preferentially endowed with a polarization angle perpendicular to the plane of scattering. The more scattered photons that reach an observer, the higher the polarization degree. The degree and angle, commonly denoted Π and χ, are the two observables of polarization,measuring the relative intensity of the polarization emission and electric field direction (relative to some reference direction), respectively. A formal definition of Π and χ requires the introduction of the Stokes parameters: I, Q, U, and V [23], which can be defined as follows

$$\begin{aligned} I &= \langle E_x^2 + E_y^2 \rangle \\ Q &= \langle E_x^2 - E_y^2 \rangle \\ U &= \langle 2E_x E_y \cos\delta \rangle \\ V &= \langle 2E_x E_y \sin\delta \rangle. \end{aligned} \tag{1.3}$$

Here, the brackets $\langle\rangle$ denote the time average. I represents the total intensity of of the radiation (both polarized and unpolarized). Q is a measure of the intensity of the polarized emission perpendicular or parallel to the reference plane - be that the detector, or the detector signal transformed into sky coordinates. U is a measure of the intensity of the polarized radiation in the 45° direction to the reference plane. V is a measure of circular polarization, which is not relevant to the work that follows but is included for completeness. δ is a measure

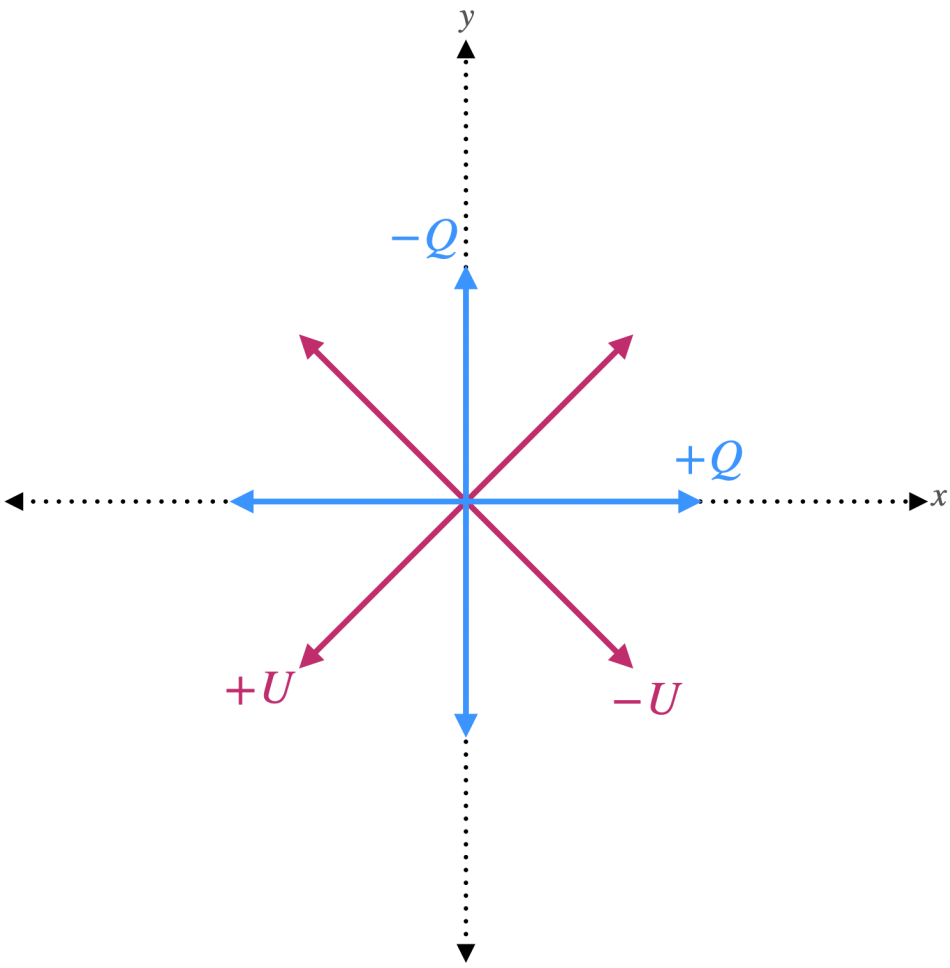

Fig. 1.2: Stokes Parameters Q and U

of the phase, or the lag of E_y behind E_x. The Stokes parameters Q and U are schematically drawn in Figure 1.2. From the Stokes parameters, the polarization fraction and angle are defined as

$$\Pi = \sqrt{\left(\frac{Q}{I}\right)^2 + \left(\frac{U}{I}\right)^2} \quad \text{and} \quad \chi = \frac{1}{2} arctan\left(\frac{U}{Q}\right). \tag{1.4}$$

The treatment of polarization in this thesis follows the formalism of Chandrasekhar [24] and his calculations of the polarization induced for scattering off an indefinitely thick electron atmosphere. The strong gravity environment around a black hole can impact the polarization

of X-rays emitted from the accreting plasma and corona. One of the predictions of General Relativity is that light does not travel in a straight line as it is perceived to in our every day lives, but in fact follows a path determined by the curvature of the spacetime through which it travels. Observation of this phenomena was one of the first experimental verifications of General Relativity when Sir Arthur Eddingonton and Andrew Crommelin measured the gravitational lensing of a star around the sun during a solar eclipse in 1919 [25]. X-rays emitted from near the black hole are bent by the curvature it induces in the spacetime which has two consequences on the polarization. The first consequence is that these photons can be bent back onto the disk from which they emitted and scatter, inducing a polarization angle perpendicular to the plane of scattering and a polarization degree proportional to the intensity of the incident radiation and the incoming and outgoing angles of the interaction.

The second consequence has to due with the orthogonality of the photon's polarization four vector, $\mathbf{f}^{\mu}$ and its wave vector $\mathbf{k}^{\mu}$. Light is a transverse electromagnetic wave - the direction of its propagation, encoded in $\mathbf{k}^{\mu}$, and the direction of its electric (and magnetic) field, encoded in $\mathbf{f}^{\mu}$, must remain - by definition - orthogonal, such that $f_{\mu}k^{\nu} = 0$. As the photon moves forward, the polarization vector is 'parallel transported' along with it. As the photon's path is bent around the black hole, the direction of its electric fields must also necessarily change to maintain this relationship.

Both of these effects - scattering and propogation through curved spacetime - have an effect on the polarization spectra, as shown in the simulated spectra of a stellar mass black hole in the soft state in Figure 1.3. As the spin (a) increases, the inner edge of the accretion disk moves to smaller radii where the curvature of the spacetime is higher. The swing in polarization angle from horizontal to vertical is due to the effect of this curvature on the trajectory of the photons. As the path of light emitted closer to the black hole moves through this highly curved spacetime the polarization vector rotates relative to the wave vector to

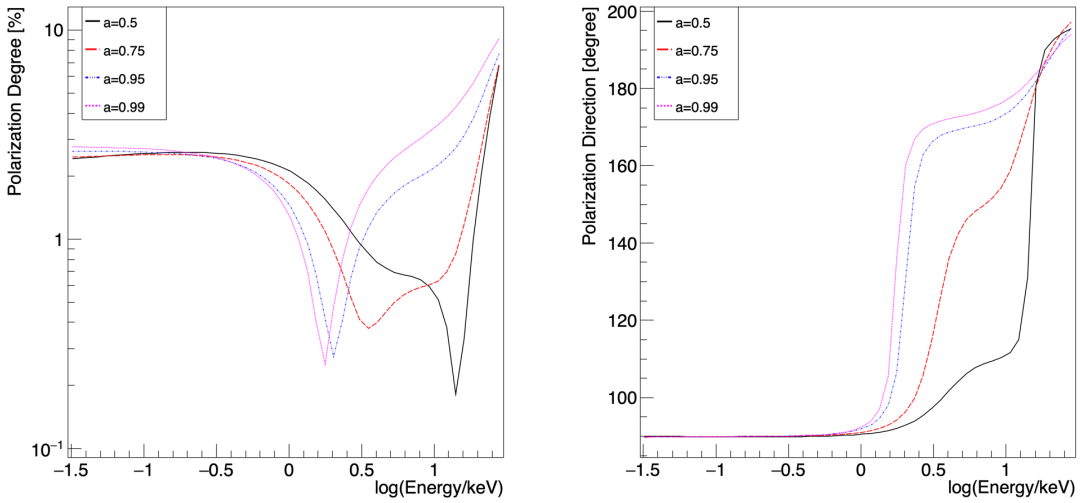

Fig. 1.3: Simulated spectra for polarization degree (left) and angle (right) for thin disks with various values of spin.

maintain orthogonality. Additionally, light emitted from these smaller radii at higher spins have a higher chance of scattering, again due to the curvature, raising the polarization fraction at high energies. The polarization induced by both lensing and scattering increases with increasing inclination - with the lowest values measured when the disk is viewed face on, and the highest values measured when it is viewed edge on. This trend allows X-ray polarization to be utitlized to measure the spin [26] and inclination [27] of accreting stellar mass black holes.

X-ray polarization has long been studied theoretically, but is a very young field experimentally. The first X-ray polarization measurements of an accreting black hole were of Cyg X-1 in 1976, showing low polarizations - 2.4% and 5.3% at 2.6keV and 5.2keV, respectively [28]. Though these were low significance detections, they are inline with theoretical models. More recently, the field of X-ray polarimetry has been burgeoning, with balloon borne missions like *X-Calibur*[29] and *XL-Calibur*[30], and space-borne missions like the *Imaging*

X-ray Polarimetry Explorer - *IXPE*[31] all launching within the last five years. *IXPE* is already producing exciting - and unexpected results - with observations of Cyg X-1 indicating that the corona is extended and perpendicular to the jet [22].

1.2.3 Quasi-Periodic Oscillations

In Section 1.2.1 the effect of state transitions on the spectra of accreting black holes were discussed. These transitions occur on timescales of days/weeks/months. There are, however, other variations in spectral output associated with these state transitions which occur on sub-second timescales, known as Quasi-Periodic Oscillations (QPOs). QPOs come in two flavors, low frequency (lfQPO) and high frequency (hfQPO), and both are relevant to the work that follows. While lfQPOs are common in stellar mass black holes, hfQPOs are exceedingly rare - having only been observed in a few sources. QPOs are identified by the behavior of the lightcurve in Fourier space, with the square magnitude of the transform giving the power spectral density, the amount of power in a signal at a given frequency.

1.2.3.1 Low Frequency Quasi-Periodic Oscillations

Low-frequency QPOs (lfQPO) are characterized as having a centroid frequency $\leq 30Hz$ and are classified into three types, Type A, B, and C. Type C and B QPOs are the strongest of the three, with narrow features and high power density, whereas Type A are broad and have lower power density [32]. There are two important distinctions between Type B and C QPOs, both of which give indications of their physical origin. Type C QPOs are often associated with broadband noise[32], a feature which may be due to fluctuations in the mass accretion rate $\dot{M}$ propagating through the disk [33], while this noise is absent in Type B QPOs. Secondly, Type C QPO signals tend to have higher power spectral density for high

inclination sources, whereas the opposite is true for Type B QPOs [34, 35]. This trending of power and inclination implies that Type C QPOs may have a geometric origin (e.g., precession of the inner disk [36]), as the boosting of emission would be stronger at higher inclinations. This is supported by observations of H1743-322 which showed a shift in the Fe-Kα centroid along the phase of a Type C QPO[37].

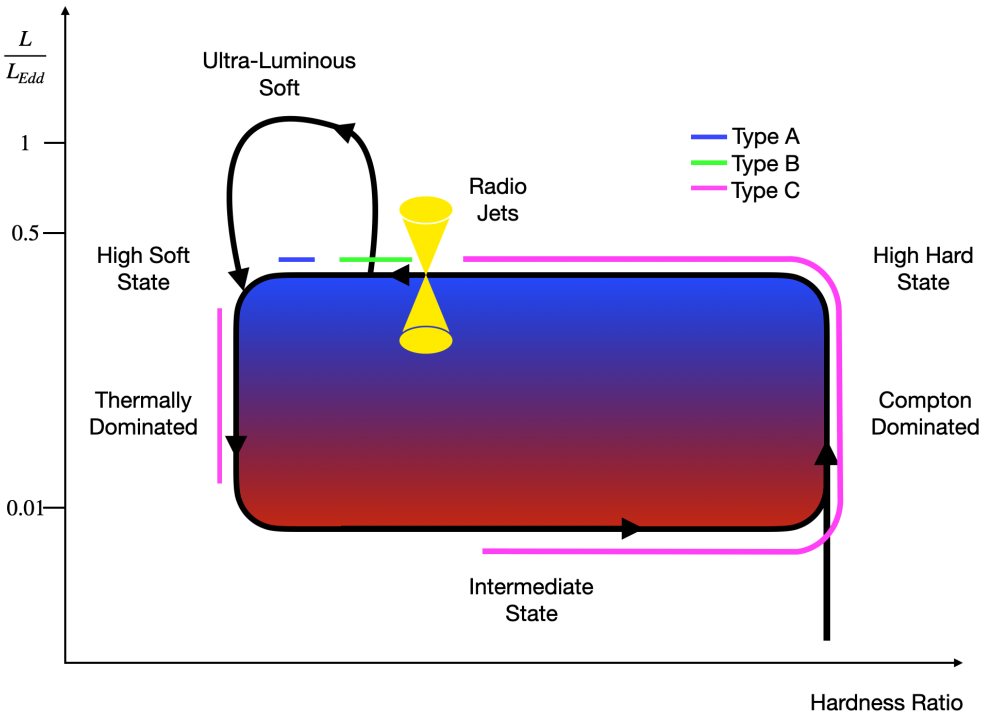

Fig. 1.4: Hardness-Intensity Diagram Adapted from [1, 2] with lfQPO associations added.

The occurence of these signals is tightly correlated to the state transitions discussed in Section 1.2.1, and so the figure is repeated here with the addition of the lfQPO types in their state of occurrence. Type C QPOs are by far the most common; a statistical study by Motta et al. in 2015 [34] identified 564 lfQPOS in archival RXTE data, with 400 being Type C. Most typically these signals are seen in the 'hard-intermediate' (bottom and top of loop) and low-hard to high-hard transition (right side of loop), though they have also been observed

in the low soft and ultra-luminous soft states [38]. The frequency of their oscillation tends to increase with increasing flux. Type C QPOs have also been observed in the infrared [39], optical [40], and ultra-violet [41]. In some of these cases the lfQPO frequencies across the infrared, optical, and ultraviolet bands correlated directly with the X-ray oscillation.

Some systems abruptly transition from the hard-intermediate state to the so called 'soft-intermediate' state (SIMS) (along the top of the H-I Diagram in Figure 1.4). In this state, the Type C QPOs disappear and Type B QPOs arise. These oscillations, which as mentioned previously tend to have more power at lower inclinations, may be associated with the production of radio jets [42], a phenomena which often occurs in the SIMS state. They typically have a frequency $1 - 6$Hz. Finally, Type A QPOs - the rarest of the three lfQPOs - are known only to occur in the high-soft state after the SIMS transition has completed. There have only been on the order 10 detected, and they are characterized by a very weak and broad signal [32]

1.2.3.2 High Frequency Quasi-Periodic Oscillations

High frequency QPOs have shown to be more elusive than lfQPOs, with detections in only < 10 sources. The first hfQPO detection [43] was in GRS1915+105 (GRS1915 hereafter) at 67Hz. Since then, multiple hfQPOs have been observed in GRS1915 at varying frequencies [44, 45], 34 Hz, 41 Hz, 113 Hz, and 166 Hz, and some of them - in particular the 67 Hz signal - have been observed numerous times. GRS1915 is a special case, with only one other source - IGR J17091-3642 showing an hfQPO near this frequency, at 66 Hz [46]. The rest of the hfQPOs detected have all been above 100 Hz, with the highest signal coming from GRO J1655-40 in which a 450 Hz signal was discovered [47].

The source of these signals is not known. Some of these frequencies - like the 450 Hz frequency in GRO J1655-40 - correspond to characteristic orbital frequencies in the inner

regions of the disk near or inside the innermost stable circular orbit. In sources that have shown multiple hfQPOs, the frequencies commonly appear in 2 : 1 and 3 : 2 harmonics (41 Hz and 67 Hz frequencies in GRS1915 [43, 44], 180 Hz and 280 Hz in XTE J1550-564 [48]). However, these harmonic pairs have only occurred simultaneously in one source, GRO J1655-40, with significance [47]. Given that, and the rarity of their detection, the apparent ratios exhibited may simply be coincidence.

There is an apparent energy and state dependence to these detections, with the strength of the signal typically increasing with increasing energy [47, 43, 48]. In XTE J1550-564, the majority of hfQPOs are detected while the system is in the SIMS state; prior to that particular detection, [49] noted that all significant detections had occurred in the high hard state. Also worth noting is that while many sources are repeaters, the frequencies of signals that appear over a single outburst do not seem to shift their frequency as the luminosity increases during state transitions [49]. This particular observation, combined with sources like GRS1915 that over years have repeated the same signal at approximately the same frequency, imply that the source of these signals is related directly to the mass and spin of the black hole (as those two characteristics are the only quantities which would be constant over such long time periods). With a better understanding of the production mechanism(s) behind hfQPOs, new methods for measuring the mass and spin of accretion black holes may be developed.

1.3 Accretion Disks Theory

The standard model of accretions disks - thin disk disk model - was originally introduced by Shakura & Sunyaev in 1973 [50], and that same year was given a relativistic treatment by Novikov and Thorne [51]. The model is that of a steady state, geometrically thin, optically

thick disk in equatorial plane of the black hole. It is assumed that the torque vanishes at the innermost stable circular orbit (r_{ISCO}), and thus the disk truncates at this radius. The symmetry of the thin disk allows it to be treated as a series of concentric annuli each of which is assumed to orbit with a Keplerian frequency $\Omega = \frac{1}{a+r^{3/2}}$, where r is the radius of the orbit and geometrized units of $G = c = 1$ and $M = 1$ have been adopted. This Keplerian nature of the disk requires that the orbital motion of the disk be differential; two adjacent annuli will orbit at different azimuthal speeds, inducing *shear* in the plasma. This shear in the presence of viscosity leads to dissipation, which they supposed would naturally shed angular momentum by generating heat, allowing the matter to slowly infall towards the black hole. The disk here is radiatively efficient, meaning the heat generated by viscosity is radiated away immediately, which keeps the disk cool (and thus, geometrically thin). As matter moves inward to smaller radii, orbital frequencies increase, and thus shear increases, generating more heat but over smaller and smaller volumes, which increase the luminosity and the temperature at these smaller radii. Page and Thorne derived the profile of this emission in 1974 [52], finding it to be a quasi-thermal blackbody proportional to the accretion rate, $\dot{M}$, and peaking in soft X-ray band. The highest energy emission in this profile, correlated with the highest disk temperatures, are generated in the innermost regions of the flow.

One of the strengths of this model is that it is agnostic of the details of the viscosity, parameterizing all of the possible viscosity mechanisms into the α parameter. The exact nature of the viscosity need not be known in order to make predictions based off of this model, and the predictions resulting from it have proven very successful. It correctly predicts the thermal components of emission in the soft state and with the addition of some coronal component, like the lamppost [53], seems to more or less predict the behavior of the Fe-Kα emission observed in stellar mass black hole and AGN.

The Fe-Kα is the most prominent fluorescence line in both active galacy nuclei (AGN) and stellar mass black holes. Emitted from the K-shell at a very narrow rest frame energy of 6.4keV, this line is spurred from Comptonized emission from the corona reflecting off of the cool, optically thick accretion disk. Gravitational redshifting as well as Doppler red and blue shifting broaden this line over $\sim 2 - 12$keV. The width of the line is correlated with both spin and inclination. As r_{ISCO} decreases with increasing spin, higher spinning black holes exhibit stronger relativistic boosts on emission from the inner-most regions. The boosts also have more of an effect at higher inclinations as the line of sight of the observer approaches the direction of motion, as shown in Figure 1.5.

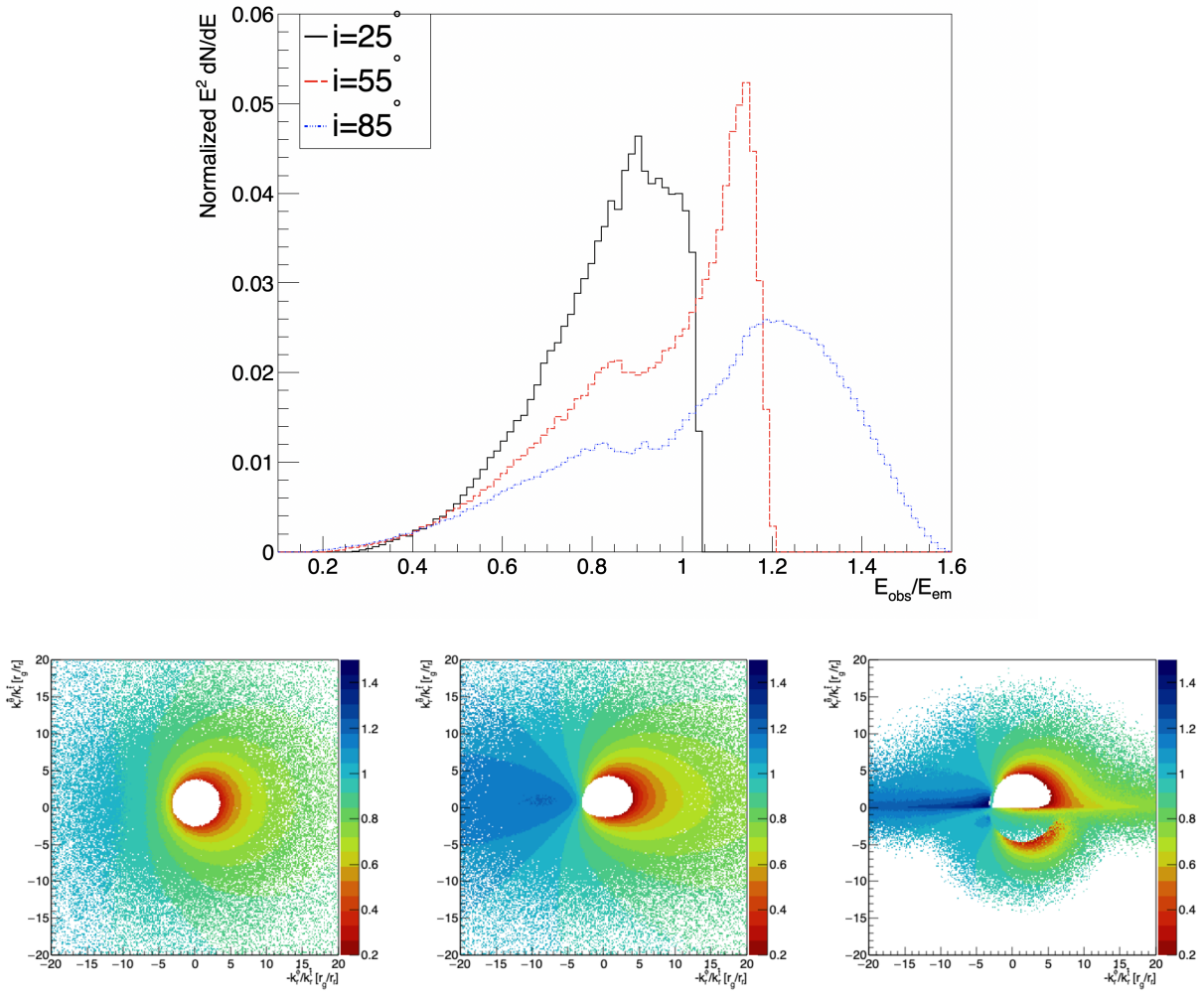

Fig. 1.5: Fe-Kα profiles and Doppler maps for a thin disk with a spin of $a = 0.9$ at inclination angles of $i = 25°$, $55°$, and $85°$. The top figure shows the boosting, or g-factor, of the Fe-Kα line with normalized flux. The bottom images are dopper maps of this boosting, with the inclination angle increasing as from left to right. At higher inclinations the blue shift increases, as more emission is boosting directly at the observer. The relativistic motion not only blue shifts the light, but *beams* it with an opening half angle $\theta_{1/2} \propto 1/\gamma$. This is the source of the higher flux observed as $E_{obs}/E_{em} > 1$. Also worth noting is that the red shifted emission extends farther than the blue - this is due to the combination of Doppler redshifting and gravitational redshifting.

There are, however, some obvious shortcomings to the thin disk model, foremost being that it is steady state - it does not allow for the state transitions, including the generation and evolution of a corona that is observed in nature. Coupled with these state transitions is a mounting body of observational evidence that suggests that the angular momentum vectors of the black hole and the binary system are misaligned [54, 55, 56, 57]. This misalignment can lead to a warped and, in some cases, dynamically unstable accretion flow geometry. The model is also only applicable to accretion rates between a few percent and a few tens of percent of the Eddington rate. For very low accretion rates $\dot{M} < 0.01\dot{M}_{Edd}$, disks no longer radiate efficiently (and thus their luminosities fall), inducing thermal pressures that cause an increase in thickness and catalyze advection as a mechanism for cooling. At very high accretion accretion rates, $\dot{M} \geq 0.3\dot{M}_{Edd}$, the infall of the matter becomes sufficiently high that the heat generated by viscosity cannot be radiated away fast enough to keep the disk cool. These disks continue to radiate, but advection becomes an additional method of cooling as the thermal pressures rise [58, 59, 60]. These two families of disks are known as Advection Dominated Accretion Flows (ADAFs) and 'slim' disks, respectively.

ADAFs are a popular candidate to explain the quiescent and low-hard state observed in stellar mass black holes and AGN [61]. As the radiative efficiency of the plasma falls, the electrons and ions thermally decouple, naturally leading to the generation of a hot, optically thin electron corona in the inner regions of the disk, which sets up the transition into the low-hard and high-hard states. The majority of accreting black holes spend most of their lives in this state of quiescence, outbursting into accretion episodes only periodically. Thus in order to truly understand the exotic physics that occurs in these systems an exploration of the parameter space beyond the standard thin disk is required. This effort is enacted through detailed and computationally expensive numerical simulations of the plasma in the high gravity regime.

1.4 General Relativistic Magneto-Hydrodynamical Simulations (GRMHD)

General Relativistic Magneto-Hydrodynamical simulations (GRMHD) are a powerful tool for exploring the dynamics of plasma in the high gravity regime. These simulations are based on the ideal MHD assumption that electrons and ions form a charge neutral inseparable medium. The predictive power is often limited by the finite resolutions and finite run times of the simulations. The latter render the outcome dependent on the usually idealized initial conditions. Nevertheless, GRMHD have already afforded us with new insights, revealing the mechanisms responsible for turbulence and viscosity, the validity of the inner boundary zero torque assumption, and indications of how different mechanisms can conspire to create jets. This section will provide a (very) brief overview of the numerical scheme involved in GRMHD calculations and the challenges involved therein, followed by a review of some important discoveries that have been made in these experiments in the past three decades. The section will close with a description of the current state of the art, and work in progress.

1.4.1 GRMHD Equations in Less Than Two Pages

In simplest terms, GRMHD simulations provide a numerical scheme over which to integrate the conservation laws for mass, momentum, and energy. Following the formalism of Misner, Wheeler, and Thorne [6], these equations can be written in a General Relativistic framework by utilizing the metric tensor and the stress energy tensor. The following aligns with the standard convention of using greek indices to refer to components of a four vector and roman indices to refer only to the spatial components. Depending on the purpose of the simulation the metric may take either the Kerr or Schwarzchild form. Often the metric is expressed

in the Kerr-Schild formulation, which has no coordinate singularity at the event horizon, allowing the trajectory of matter to be traced through the horizon. Mass conservation is given by

$$\partial_t(\sqrt{-g}\rho u^t) = -\partial_i(\sqrt{-g})\rho u^i, \tag{1.5}$$

where u^μ is the four velocity of the fluid, ρ is the rest-mass density, and $\sqrt{-g}$ is the determinant of the metric. Momentum and energy conservation have a very similar form, with the addition of the Christoffel symbol components required for covariant differentiation,

$$\partial_t(\sqrt{-g}T^t_\mu = -\partial_i(\sqrt{-g}T^i_\mu) + \sqrt{-g}T^\delta_\rho\Gamma^\rho_{\mu\delta}. \tag{1.6}$$

Here, T^δ_ρ is the stress energy tensor, and $\Gamma^\rho_{\mu\delta}$ are the aforementioned Christoffel symbols, which are composed of derivatives of the metric. The stress energy tensor contains the physical details of the fluid as defined in the fluid frame - its internal energy, pressure, magnetic field, etc. In ideal GRMHD, the internal energy is the thermal energy of an ideal gas, with each degree of freedom adding a factor $kT/2$ to the internal energy density u_g, where k is the Stefan Boltzmann constant and T is the temperature. The pressure is then given by the ideal gas law for a gas with an adiabitic index of γ as $p_g = (\gamma - 1)u_g$. Next, the induction equation is of the form

$$\partial_t(\sqrt{-g}B^i) = -\partial_j(\sqrt{-g}(b^j u^i - b^i u^j)), \tag{1.7}$$

where B^i are the spatial components of the magnetic field four vector $b^\mu = \frac{1}{2}\epsilon^{\mu\nu\delta\rho}u_\nu F_{\delta\rho}$ [6, 62].

These equations are the foundation of modern GRMHD but they are not the entire story. There are many assumptions which are requisite simply to make the computation technically

possible. The equation of state of the plasma, for example, is not known, and is often approximated as an ideal gas. Viscosity is also not commonly treated from first principles and is instead added artificially in accordance with the well understood microphysics [63] of MRI induced turbulence [64] (as will be discussed in the next section). These equations also do not account for radiation, so an additional layer of computation is added as a 'source' term to artificially cool the gas. This is typically an exponential function, the decay time of which is comparable to the Keplerian time scale of the disk at that point [65].

1.4.2 The Role of Magnetic Fields

Shakura & Sunyaev's thin disk model is based on the assumption that differential shear from the gradient in orbital velocity in concentric annuli of the disk was the source of the viscous stresses that transport angular momentum outward. It turns out that from a purely hydrodynamical standpoint, shear viscosity is incapable of generating sufficient turbulence to effectively transport angular momentum outward. However, Balbus and Hawley [66, 64] showed that the presence of a weak magnetic field in a differentially rotating fluid would naturally lead to what they called the magneto-rotational instability (MRI). The field threading the disk begins to twist due to the differential rotation of the plasma, and in so doing *amplifies* the perturbations and eddies induced by shear. These amplifications create the turbulence necessary to effectively shed angular momentum and allow the matter to accrete.

Seeding disks with poloidal magnetic fields has other benefits in addition to catalyzing the turbulence necessary to allow accretion. As the MRI develops, the magnetic field is stretched radially and begins to shear into a toroidal field. The magnetic field, particularly in the ergotic regions near the black hole and threading the horizon, coils up and is ejected due to magnetic pressure, forming a so called 'magnetic tower.' These towers drive conical

jets, funneling matter from the accretion flow along the field lines and away from the compact object [67, 68]. It has been shown that when a poloidal magnetic field threads the event horizon of a spinning black hole, the launching of a jet is inevitable [69]. Additionally, magnetic energy is dissipated in the upper regions of the disk, heating it and generating a hot corona that becomes trapped between the jet and the disk [70]. Recently, the mechanisms behind jets have been further refined by Liska et al. [71], who have shown that an initially seeded poloidal magnetic field is not a necessary condition for the launching of jets. Their results show that a toroidal field in the disk will naturally be converted via coriolis forces into a poloidal field, which in time launches a jet. This process also naturally truncates the disk into a magnetically arrested disk (MAD) state.

1.4.3 Recent Discoveries

Much work has been done to identify both the mechanisms of state transition and the source of QPOs in the accretion flow. With QPOs in particular, the congruence between Lense-Thirring precession frequencies and observed lfQPO frequencies have made precession a favored model to explain the source of this variability[36, 72]. Simulations of (thick) slightly tilted disks have been shown to precess due to the Lense-Thirring torques [73, 74, 75, 76, 77], but these simulations have so far only produced signatures of a possible lfQPO. This is due, in part, to the high computational cost of simulating tilted disks, which places a constraint on the runtime of the simulation itself and on the inclination of the disk in initialization.

Liska et al. have developed a GRMHD code, *H-AMR* [78], which incorporates adaptive mesh refinement and utitlizes GPU acceleration to effectively lower the computational cost while achieving significantly higher resolutions, allowing the simulation of long duration runs and thin disks. They have shown multiple tilted precessing thin disks which are sometimes

accompanied by precessing jets [79, 80]. In recent work utilizing this code, it has been shown that sufficiently tilted and thin disks undergo tearing events which not only produce an lfQPO like precession in the inner disk (spanning numerous precession cycles) but also induce hfQPO like features in the accretion rate [81]. This work forms the basis for this thesis and will be described in detail in Chapter 3. Some efforts have been made to explain hfQPO's through Rossby wave instabilities in the disk. Through post processing GRMHD data with raytracing, Varniere et al [82] have reproduced hfQPO like features in the power spectrum of the raytraced lightcurve from the RWI event. Though it must be said that the problem is still very much open, as the RWI in this case was artificially seeded and the disk was tuned to manifest its propagation.

As GRMHD simulations become more detailed and sophisticated, they allow for more powerful comparisons of simulated and observed signatures. The work described in this thesis contributed to this development by providing a radiation post-processor for the output of a GRMHD simulation. It will be shown that this post processing can be used to predict the temporal properties of the emitted X-rays. This is similar to those post processors utilized in the Event Horizon Telescope, but is specialized to raytrace X-rays rather than radio waves. This work compliments the development of simulations accounting for radiative pressure in the accretion flow and those that deviate from the ideal MHD assumption by allowing electrons and ions to have distinct temperatures (as will be described below). Such simulations may, with high enough temporal and spatial resolution, predict the location, temperature, and geometry of the coronal gas which is a major component of X-ray emission in accreting stellar mass black holes.

The inclusion of radiative transport in particular is non-trivial and very computationally expensive. Some efforts have approached the problem by implementing radiative transfer as a post-process applied to completed GRMHD simulations. Kinch and collaborators have

taken data produced with the *HARM3D* [62] and given it two stage iterative post processing to predict X-Ray spectra. This process feeds the GRMHD into the radiative transfer solver *PXTRANS* [83] and raytraces the predicted spectrum with *PANDURATA* [84] over many iterations to numerically predict the generated X-ray spectrum produced from the disk. Their work shows, at least for the spins and accretion rates considered, that the inner radius of Fe-Kα photon production is not always at r_{ISCO}, and the depth of the red shifted tail is more dependent upon $\dot{M}$ than on the spin, a. This is due to the brightness profile's extent depending both on spin and the density profile of the disk [85]. Another important observation to result from this work is the powerlaw component of the spectrum tended to harden with increasing spin. While much follow up is needed, these results could potentially allow refinements to models that currently are used to measure spin.

There are also fully radiative GRMHD (so called 'GRRMHD') codes that now exist, many unitilizing a radiation transfer scheme called "M1 Closure" [86] (which is well described in [87]). M1 closure defines the radiation stress tensor $R^{\mu\nu}$ with the radiation energy density and fluxes in the orthonormal 'rest frame' of the radiation under the assumption that the field is isotropic in this frame. Part of this simplification consequently demands that the net radiation flux be uni-directional; it is, in simplest terms, an approximation of averages. GRRMHD simulations have answered some fundamental questions that were previously out of reach, such as the thermal stability of sub-Eddington disks with moderate thickness [88], and shown that disks in a MAD state at moderate accretion rates [89] and during the super-Eddington to sub-Eddington transitions [90] remain stable.

The inclusion of two-temperature fluids brings GRRMHD even closer to reality. It is well known that the low densities and high temperatures in the corona lead to the thermal decoupling of electrons and ions, which prevents the corona from cooling. Treating the plasma with a radiative, two-temperature scheme will shed new light on the processes that

lead to the formation, evolution, and eventual dissipation of the corona observed in the state transitions of outbursting stellar mass black holes. In the past year, *H-AMR* has begun running the first fully radiative two-temperature GRMHD simulations of thin disks [91]. One of the models initialized was a geometrically thin disk threaded with a poloidal field, intended to simulate the hard intermediate state. This configuration naturally led to a build up of magnetic pressure, interrupting accretion and truncating the disk. The result was a magnetically supported hot inner corona and a radiatively supported cool outer disk, consistent with a MAD state. The simulation also showed the accretion of cold lumps of matter flowing from the truncation radius through the corona and into the black hole. This result shows for the first time that disks can naturally transition from a hard intermediate state to a hard state.

1.5 Thesis Outline

The work presented in this thesis is focused on the X-ray signatures of accretion disks which deviate from the standard thin disk. In Chapter 2, the polarization signatures of high luminosity 'slim' disks are explored, with an emphasis given to the effect of geometric thickness on the polarization over a range of disk scale heights. Chapters 3 - 5 focus on the raytracing of a GRMHD dataset representing a thin, misaligned disk in the soft-intermediate state as it undergoes tearing events, precession, and Bardeen-Petterson [92] alignment. Chapter 3 will review the GRMHD code *H-AMR*, the physics involved in disk tearing, and the details of the GRMHD dataset used in this thesis. Chapter 4 will review the details of the raytracing code utilized to create the spectral and timing signatures of this dynamically evolving disk. Chapter 5 will review the results of the raytracing, including the polarimetric, time domain, and Fe-Kα fluorescence behavior during the course of the disk's evolution. Chapter 6 will

review the works contained in this thesis and reflect on ways to build on these results.

Chapter 2

General Relativistic Raytracing Slim Accretion Disks

This chapter represents the earliest work of my graduate career, work which was completed with much help from my mentor Henric Krawczynski. This work is in the process of being submitted for publication, and this chapter follows the manuscript of the publication closely.

2.1 Introduction

The general relativistic raytracing code utilized in the following section was originally developed by Krawczynski [93] in 2012 to test the observational signatures of alternative metrics in General Relativity. In the years since it has been leveraged test the no-hair theorem using coronal emission [94], constrain the geometry of the corona using polarization and spectral timing [95], test the effect of microlensing on fluorescence lines [96, 97] and probe the location of the ISCO in AGN [98]. Most recently, it was adapted to explore the effect of Bardeen-Petterson alignment on the polarization spectra and Fe-Kα emission from accreting X-ray binaries [99, 100]. In this chapter, the code is adapted to explore the effect of disk thickness on the polarization spectra of accreting stellar mass black holes.

The standard model of accretion disks is a geometrically thin, optically thick disk isolated to the equatorial plane. While it is a good approximation, its applicability is limited to those radiatively efficient flows whose luminosities are between a few percent and a few tens of percent of the Eddington limit. However, as accretion rates rise, the heat generated by viscosity does not have enough to time radiate away efficiently, and advective cooling arises as a mechansism for energy dissipation. Thermal pressures and radiative pressures build in the disk, increasing the scale height of the disk and forming 'slim' disks [101, 102]. For rates close to the Eddington rate, the scale heights can reach as high as $H = 0.3$ [58]. At the highest luminosities, these disks have a lower efficiency than the standard thin disk [103] and can deviate from the thin disk in both their radial brightness profile and their radial extent, falling within the ISCO and up to the horizon. For cases where the radiative cooling remains dominant over advective cooling, these geometrically thick disks can remain optically thick.

In recent years much work has been done to explore the effect that geometric thickness has on reflection spectra - particularly the Fe-Kα line [104, 105, 106] and X-ray reverberation signatures [107, 108]. These works have noted that disks of sufficient thickness can effectively self-shadow their inner regions, truncating the blue-wing of the Fe-Kα line, leading to an under-estimation of spin. Geometric thickness can also cause an under-estimation of the height of the compact corona by shortening the signal delay of reverberation signals.

The effect of this geometric thickness on the reflection spectra in XRBs motivate the following chapter, which explores the effect that geometric thickness has on the polarization of thermal emission from stellar mass black holes.

2.2 Raytracing in xTrack

xTrack is a fully relativistic 'forward-shooting' raytracing code. Photon trajectories are tracked from the source - in this case, the plasma surrounding an accreting black hole - through the highly curved spacetime surrounding the black hole to an observer located sufficiently far away that space is flat. A photon is emitted as a 'packet,' a statistical ensemble which is smeared over the applicable energy range of the emitting region in analysis. Henceforth, the term 'photon' will refer to these photon packets.

The code emits photons in the rest frame of the plasma in $10,000$ logarithmically spaced radial bins at $\phi = 0$. The distribution of initial photon trajectories is isotropic, achieved by randomly drawing the photon's spatial wave vector components with equal probability per solid angle while ensuring $|\mathbf{k}^t| = |\mathbf{k}^i| = 0$, where $i = r, \theta, \phi$. The photons are initially unpolarized, with the $\mathbf{f}^r$ and $\mathbf{f}^\phi$ components being drawn at random and $\mathbf{f}^t$ and $\mathbf{f}^\theta$ being zero under the constraint $|\mathbf{f}^\mu| = 1$.

Once initialized, the photons are transformed from the plasma frame into the global frame (see 2.3). The trajectory of each photon is forward integrated using the Cash-Karp methodology [109], a fifth order Runga-Kutta numerical integration which allows for step-size adaptation during the integration. This is a requisite of general relativistic raytracing, as the highly curved spacetime around the black hole necessitates very small step-sizes to ensure accuracy. Photon trajectories are advanced by integrating the geodesic equation according to

$$\frac{d^2x^\mu}{d\lambda'^2} = -\Gamma^\mu_{\sigma\nu}\frac{dx^\sigma}{d\lambda'}\frac{dx^\nu}{d\lambda'} \tag{2.1}$$

and parallel transporting the polarization vector $\mathbf{f}^{\mu}$ according to

$$\frac{df^{\mu}}{d\lambda'} = -\Gamma^{\mu}_{\sigma\nu} f^{\sigma} \frac{dx^{\nu}}{d\lambda'}. \tag{2.2}$$

The code utilizes the Kerr metric in Boyer-Lindquist coordinates,

$$\begin{aligned} ds^2 = \frac{r^2 - 2Mr + a^2}{r^2 + a^2 cos^2\theta}(dt - asin^2\phi)^2 + \frac{sin^2\theta}{r^2 + a^2 cos^2\theta}((r^2 + a^2)d\phi - adt)^2 \\ + \frac{r^2 + a^2 cos^2\theta}{r^2 - 2Mr + a^2} dr^2 + (r^2 + a^2 cos^2\theta)d\theta^2, \end{aligned} \tag{2.3}$$

which describes the curved spacetime around a charge-free spinning black hole. Here, M is the black hole mass and a is the dimensionless spin parameter.

Photon geodesics have two possible fates: they either cross into the event horizon or reach an observer. Due to the coordinate singularity at the event horizon in Boyer-Lindquist coordinates, it is assumed that any photon whose trajectory comes within 2% of the event horizon is lost. An observer is defined as being in asymptotically flat spacetime, located at a distance of $10,000 R_g$. As this disk is axisymmetric, photons which reach the observer are integrated over all ϕ for a given inclination θ, and inclination windows are defined by as $x^{\theta}_{\gamma} \pm 4^{\circ}$. These observed photons are transformed into a coordinate stationary frame for analysis

2.2.1 Conserved Quantities - Parameterizing the Geodesic Equation

Killing vectors on a Reimannian manifold represent isometries (symmetries) of the manifold itself and are indicative of a conserved quantity within the metric describing the manifold.

These Killing vectors, and their associated conserved quatities, are a property of the space-time itself and thus are independent of the coordinate basis used to describe the metric [6, 25] In the Kerr metric, which is stationary and axially symmetric, the Killing vectors are $\xi_1 = (1, 0, 0, 0)$ and $\xi_2 = (0, 0, 0, 1)$. These vectors imply the conservation of the photon's energy and angular momentum at infinity,

$$g_{\mu\nu}\xi_1^\mu k^\nu = -E_\gamma = g_{tt}k^t + g_{t\phi}k^\phi \tag{2.4}$$

$$g_{\mu\nu}\xi_2^\mu k^\nu = L_\gamma = g_{t\phi}k^t + g_{\phi\phi}k^\phi \tag{2.5}$$

Taking $k^t = \frac{dt}{d\lambda}$, $k^\phi = \frac{d\phi}{d\lambda}$, $\lambda' = E_\gamma\lambda$, where λ is an affine parameter, and Equations 2.4 and 2.5, one can define

$$\frac{dt}{d\lambda'} = \frac{-g_{\phi\phi} - (L_\gamma)/(E_\gamma)g_{t\phi}}{g_{tt}g_{\phi\phi} - g_{t\phi}^2} \tag{2.6}$$

$$\frac{d\phi}{d\lambda'} = \frac{(L_\gamma)/(E_\gamma)g_{tt}g_{t\phi}}{g_{tt}g_{\phi\phi} - g_{t\phi}^2}. \tag{2.7}$$

This allows the calculation of the t and ϕ components of the geodesic equation (Equation 2.1) without needing to compute the integration, which reduces both the error on the calculation and the computational expense required [93].

2.3 The Torus Model

The model used is a simple, phenomenological toroidal disk similar to the 'slim' disk model introduced by Abramowicz in 1988 [101]. The parameterization ignores the accretion rate and thermal and radiative pressures in the disk, as this study is concerned only with the effect of the geometry on the polarization signatures. The thickness of the torus scales with

the root of the distance from $\rho - r_{ISCO}$, where ρ is the cylindrical radius.

$$z(\rho) = H\sqrt{\left(\frac{r_0}{2}\right)^2 - (\rho 1(\rho))^2}\sqrt{\rho 2(\rho)} \tag{2.8}$$

with

$$\rho 1(\rho) = \rho - r_{isco} - \frac{r_0}{2} \tag{2.9}$$

and

$$\rho 2(\rho) = \frac{\rho - r_{isco}}{r_0}. \tag{2.10}$$

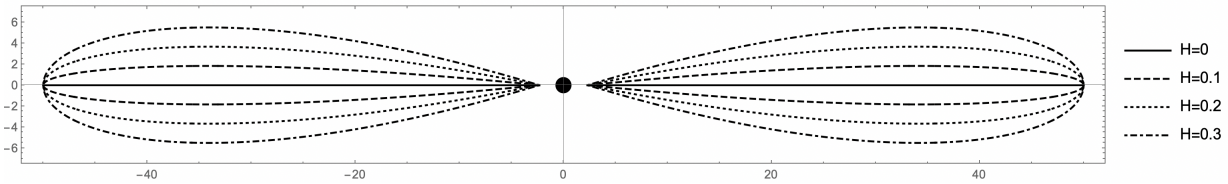

Fig. 2.1: Torus geometry for scale heights of 0.1 (dashed line), 0.2 (dotted line), 0.3 (dash-dotted line)

Here, $H = \frac{z}{\rho}$ is the scale height, r_0 is the outer edge of the disk, and $\rho 2(\rho)$ defines the convexity of the surface. This cylindrical parameterization can then be converted to Boyer-Lindquist coordinates as

$$\Theta(\rho) = \arctan\left(\frac{\rho}{z(\rho)}\right) \tag{2.11}$$

$$r(\rho) = \frac{\rho}{\sin(\Theta(\rho))} \tag{2.12}$$

yielding

$$T^{\mu}(r, \Theta) = \{0, r(\rho), \Theta(\rho), \phi\}. \tag{2.13}$$

Here, $\phi \in [0, 2\pi)$. Equation (2.13) is used to determine photon-disk interactions and to the calculate the tetrad of the disk at those locations. The disk is assumed to rotate rigidly at a given cyclindrical radius ρ, such that the material above or below any point in the equatorial plane has a Keplerian angular velocity of $\Omega_k = \frac{1}{a+\rho^{\frac{3}{2}}}$. With Boyer-Lindquist tangent vectors $\mathbf{e}_\mu = \partial_\mu$ and denoting the plasma frame with a tilde, the tetrad is formed by orthogonalizing the four velocity against the tangent vectors of the surface as described in Appendix A. The time-like basis vector of the tetrad is then given by

$$\mathbf{e}_{\tilde{t}} = \frac{1}{\sqrt{-g_{tt} - \Omega_k(2g_{t\phi} + g_{\phi\phi}\Omega_k)}}(\partial_t + \Omega_k \partial_\phi). \tag{2.14}$$

The radial tangent $\mathbf{e}_{\tilde{\mathbf{r}}}$ is proportional to $\frac{d}{dr}(T(r, \Theta))$ and normalized to unity. $\mathbf{e}_{\tilde{\theta}}$ is proportional to $\mathbf{e}_\mathbf{r}$ and $\mathbf{e}_\theta$ and orthogonal to $\mathbf{e}_{\tilde{\mathbf{r}}}$. The final component $\mathbf{e}_{\tilde{\phi}}$ will be proportional to $\mathbf{e}_\phi$ and orthogonal to $\mathbf{e}_{\tilde{\mathbf{t}}}$. This yields

$$\mathbf{e}_{\tilde{r}} = \frac{1}{\sqrt{g_{rr}(\frac{dr}{d\rho})^2 + g_{\theta\theta}(\frac{d\Theta}{d\rho})^2}}\left(\frac{dr}{d\rho}\partial_r + \frac{d\Theta}{d\rho}\partial_\theta\right) \tag{2.15}$$

$$\mathbf{e}_{\tilde{\theta}} = \alpha\left(\frac{\frac{d\Theta}{d\rho}}{(\frac{d\Theta}{d\rho} - \frac{dr}{d\rho})g_{rr}}\partial_r + \frac{\frac{dr}{d\rho}}{(\frac{dr}{d\rho} - \frac{d\Theta}{d\rho})g_{\theta\theta}}\partial_\theta\right) \tag{2.16}$$

$$\alpha = \sqrt{\frac{(\frac{dr}{d\rho} - \frac{d\Theta}{d\rho})^2 g_{rr} g_{\theta\theta}}{(\frac{dr}{d\rho})^2 g_{rr} + (\frac{d\Theta}{d\rho})^2 g_{\theta\theta}}} \tag{2.17}$$

and

$$\mathbf{e}_{\tilde{\phi}} = \beta\left(\frac{g_{t\phi} + g_{\phi\phi}\Omega_k}{g_{t\phi}^2 - g_{tt}g_{\phi\phi}}\partial_t + \frac{g_{tt} + g_{t\phi}\Omega_k}{g_{tt}g_{\phi\phi} - g_{t\phi}^2}\partial_\phi\right) \tag{2.18}$$

$$\beta = \frac{g_{tt} + g_{t\phi}\Omega_k}{(g_{t\phi}^2 - g_{tt}g_{\phi\phi})(\Omega_k - 1)}\sqrt{-\frac{(g_{t\phi}^2 - g_{tt}g_{\phi\phi})(\Omega_k - 1)^2}{g_{tt} + \Omega_k(2g_{t\phi} + g_{\phi\phi}\Omega_k)}} \tag{2.19}$$

In the limit $z/\rho \to 0$, the tetrad becomes the thin-disk tetrad used in [93]. These vectors

form the basis $e^{\nu}_{\widetilde{\mu}}$, where $\mathbf{e}_{\widetilde{\mu}} = e^{\nu}_{\widetilde{\mu}} \cdot \mathbf{e}_{\nu}$. Letting a bar denote the inverse transformation matrix, photon wave vectors $\mathbf{k}^{\mu}$ are transformed into and out of the plasma frame with

$$\mathbf{k}^{\widetilde{\mu}} = \bar{e}^{\widetilde{\mu}}_{\nu} \cdot \mathbf{k}^{\nu} \tag{2.20}$$

and

$$\mathbf{k}^{\nu} = e^{\nu}_{\widetilde{\mu}} \cdot \mathbf{k}^{\widetilde{\mu}}. \tag{2.21}$$

2.4 Thermal Emission

Thermal photons are emitted isotropically into the upper hemisphere of the disk from $10,000$ logarithmically spaced bins on the interval $r_{ISCO} \leq r \leq 50r_g$. Here, $r_g = \frac{GM}{c^2}$ is the gravitational radius with G being the gravitational constant, M being the black hole mass, and c being the speed of light. The energy dissipation of the toroidal disk over a given cyclindral radius $\delta\rho$ is assumed to be proportional to the dissipation over the same radial interval $\Delta r = \Delta\rho$ as derived by Page and Thorne [52]. They derive the effective temperature and time-average flux of radiant energy (time-average radiative energy dissipation) for a geometrically thin, quasi-Keplerian and optically thick accretion flow as

$$T_{eff} = \left(\frac{F(r)}{\sigma_{SB}}\right)^{\frac{1}{4}} \tag{2.22}$$

with

$$F(r) = \frac{\dot{M}}{4\pi} e^{-(\nu+\psi+\mu)} \frac{-p^{t}{}_{,r}}{p_{\phi}} \int_{r_{ISCO}}^{r} \frac{p_{\phi,r}}{p^{t}} dr \tag{2.23}$$

which is projected onto the surface of the toroid as $F(\rho)$.

The photons are weighted with the product of Equation 2.23 of Page and Thorne with

the limb brightening function for an indefinitely deep electron atmosphere as derived by Chandrasekhar [24]. It is assumed that photons do not interact with infalling matter in the plunging region $r_{EH} \leq r \leq r_{ISCO}$ (where r_{EH} is the event horizon).

Photons are allowed to repeatedly interact with the disk. When a geodesic intersects the disk, the integration is truncated such that the photon's trajectory ends exactly on the surface. From here, the tetrad $e^{\nu}_{\tilde{\mu}}$ and its inverse are calculated at the location of the photon interaction. The wave vector and polarization vector are transformed into the rest frame of the disk, and from f^{ν}_{PF} the incoming polarization angle and fraction are calculated. The outgoing Stokes parameters are then calculated from Chandrasekhar's Table XXV and Equation 164 (Chapter X, Section 70) [24] and subsequently used to calculate the outgoing polarization angle and fraction, the intensity of the reflected emission, and the statistical weight of the interaction according to

$$\omega_{sc} = \frac{2\mu I}{\mu_0 F} \tag{2.24}$$

The trajectory of the photon after reflection is drawn from a random probability per solid angle in the plasma frame, and subsequently both k^{μ} and f^{ν} are transformed back into the global Boyer-Lindquist frame where the integration and parallel transport of each, respectively, continues until the photon either falls into the event horizon or reaches an observer.

The observer is stationary and located in flat spacetime $10,000 r_g$ away from the compact object. Photons which reach $r = 10,000 r_g$ are transformed into the observer frame using a tetrad constructed such that

$$\mathbf{e}_{\tilde{t}} = \mathbf{p}_t = \frac{e_t}{\sqrt{g_{tt}}} \tag{2.25}$$

$$\mathbf{e}_{\tilde{r}} = \frac{e_r}{\sqrt{g_{rr}}} \tag{2.26}$$

$$\mathbf{e}_{\tilde{\theta}} = \frac{e_\theta}{\sqrt{g_{\theta\theta}}} \tag{2.27}$$

with $\mathbf{e}_{\tilde{\phi}}$ being a linear combination of $\mathbf{e}_t$ and $\mathbf{e}_\phi$ and orthogonal to $\mathbf{e}_{\tilde{t}}$. The vectors of this tetrad then satisfy

$$\mathbf{e}_{\tilde{\mu}} \cdot \mathbf{e}_{\tilde{\nu}} = \eta_{\mu\nu}, \tag{2.28}$$

where $\eta_{\mu\nu}$ is the metric of Minkowski. Due to the symmetry of the disk, photons arriving below the equator ($\theta_\gamma \geq \frac{\pi}{2}$) can be folded into the upper hemisphere with the following transformations

$$x^\theta_{\gamma\ new} = \pi - x^\theta_\gamma \tag{2.29}$$

$$k^\theta_{\gamma\ new} = -k^\theta_\gamma \tag{2.30}$$

$$f^\theta_{\gamma\ new} = -f^\theta_\gamma. \tag{2.31}$$

The code was vetted by comparing the polarization results for a torus with a scale height of zero against the standard thin disk model [93], shown in in Figure 2.2. Small deviations from the thin disk are expected with this torus model, particularly at lower energies, due to the truncation of the outer edge of the disk at $50r_g$. The maximum deviation in the polarization angle is $< 8°$ and the maximum deviation of the polarization degree is $\sim 14\%$ of the thin disk value (0.7% and 0.8% at 2keV).

2.5 Polarization Spectra of Toroidal Accretion Disks

In this section the polarization spectra of three toroids with scale heights $H = 0.1,\ 0.2,\ 0.3$ are compared, each having an outer radius $r_0 = 50r_g$ across a range of spins and observer

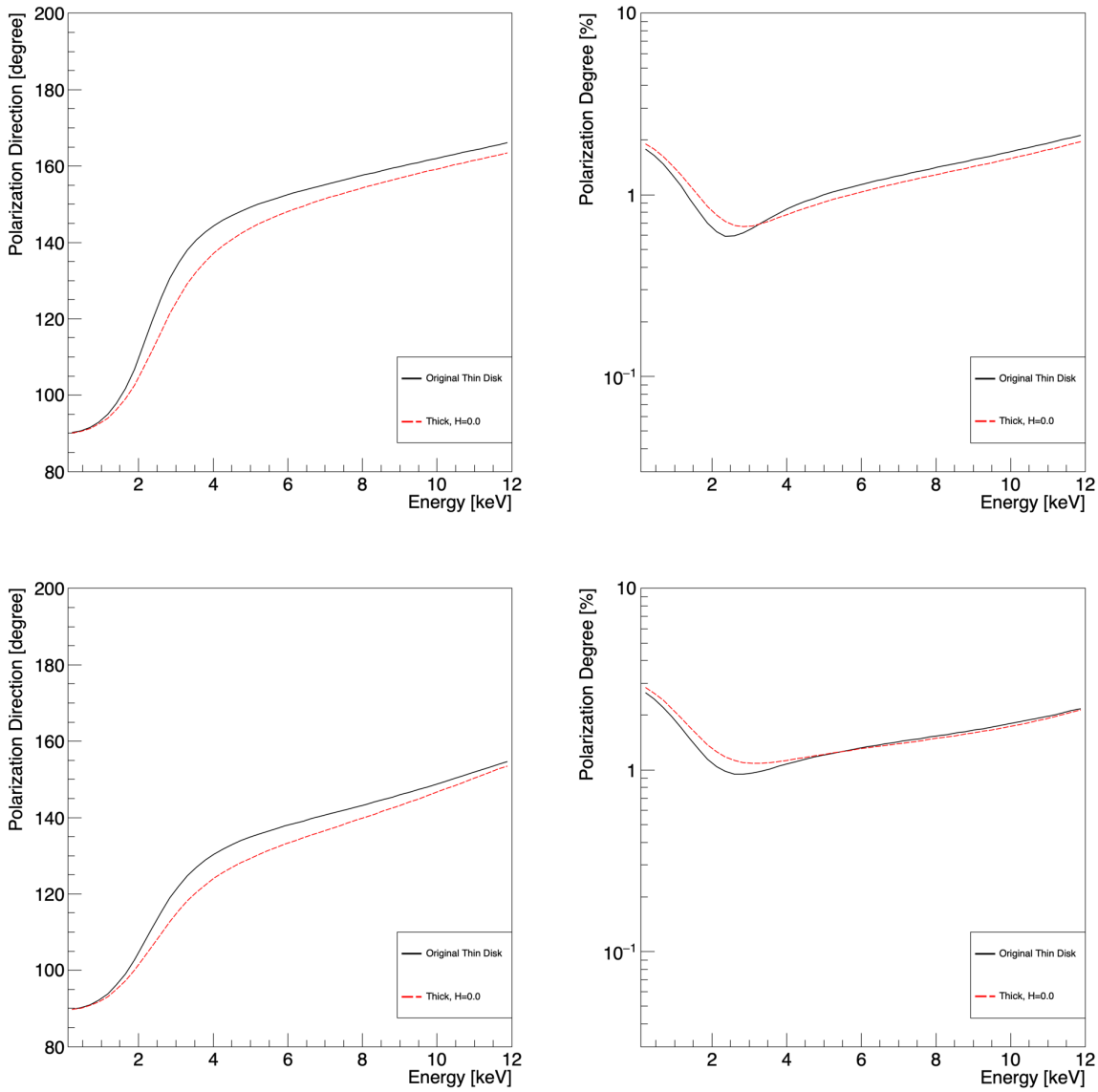

Fig. 2.2: Polarization angle (left) and degree (right) inclinations of 65° and (top) and 75° (bottom). The standard thin disk model is in black and the thick disk with a scale height of zero is in red.

inclinations. The results are compared to the spectra of a thin disk with the same outer radius and spin. Additionally, the spectra are explored over a range of luminosities expected to give rise to geometrically thick accretion flows. Unless otherwise stated, the spectra and images that follow are for a spin of $a = 0.9$ and luminosity $50\%L_{Edd}$. In each data set the black hole has a mass of $10\,M_{\odot}$ and 5×10^7 photons are generated for each configuration. Emission is assumed to follow a Planckian distribution of a dilute black body with $T = f_h\,T(\rho)$, where $T(\rho)$ is given by Equation 2.22 and $f_h = 1.8$ is the spectral hardening factor [110].

Images of the accretion disk are made by back projecting the wave vector in the coordinate stationary frame, $\mathbf{k}^{\mu}_{obs}$, into a plane perpendicular to the line of sight and intersecting the point $r = 0$. These images are composed of the total emission (both direct and reflected) and colored in log scale according to the intensity. The overlaid bars indicate the polarization, where the magnitude corresponds to polarization degree and the direction corresponds to polarization angle. In all images, the black hole spin axis is 'right-handed,' such that the angular momentum of the black hole points out of the page for an inclination of 0° and vertically in the page for an inclination of 90°. Accordingly, the material in the left side of the image is rotating towards the observer and receives a boost due to its relativistic motion, appearing brighter than the material on the right side of the images which is receding and thus boosted away from the observer. Note that the emission from the far side of the disk is lensed around the compact object both above and below the disk for high inclinations.

Figure 2.3 shows disk images with polarization overlaid for four values of inclination, $\theta = 25°, 45°, 65°$, and 85°, which increase from top to bottom. From left to right the scale height increases with the thin disk in the left-most column and $H = 0.1,\ 0.2,\ 0.3$ following. At low inclinations ($\theta = 25°, 45°$), there is a qualitative increase in the polarization degree as the scale height increases. At 65° the polarization angle, particularly on the approaching side of the disk, also begins to shift. At an inclination of 85°, the appearance of the disk

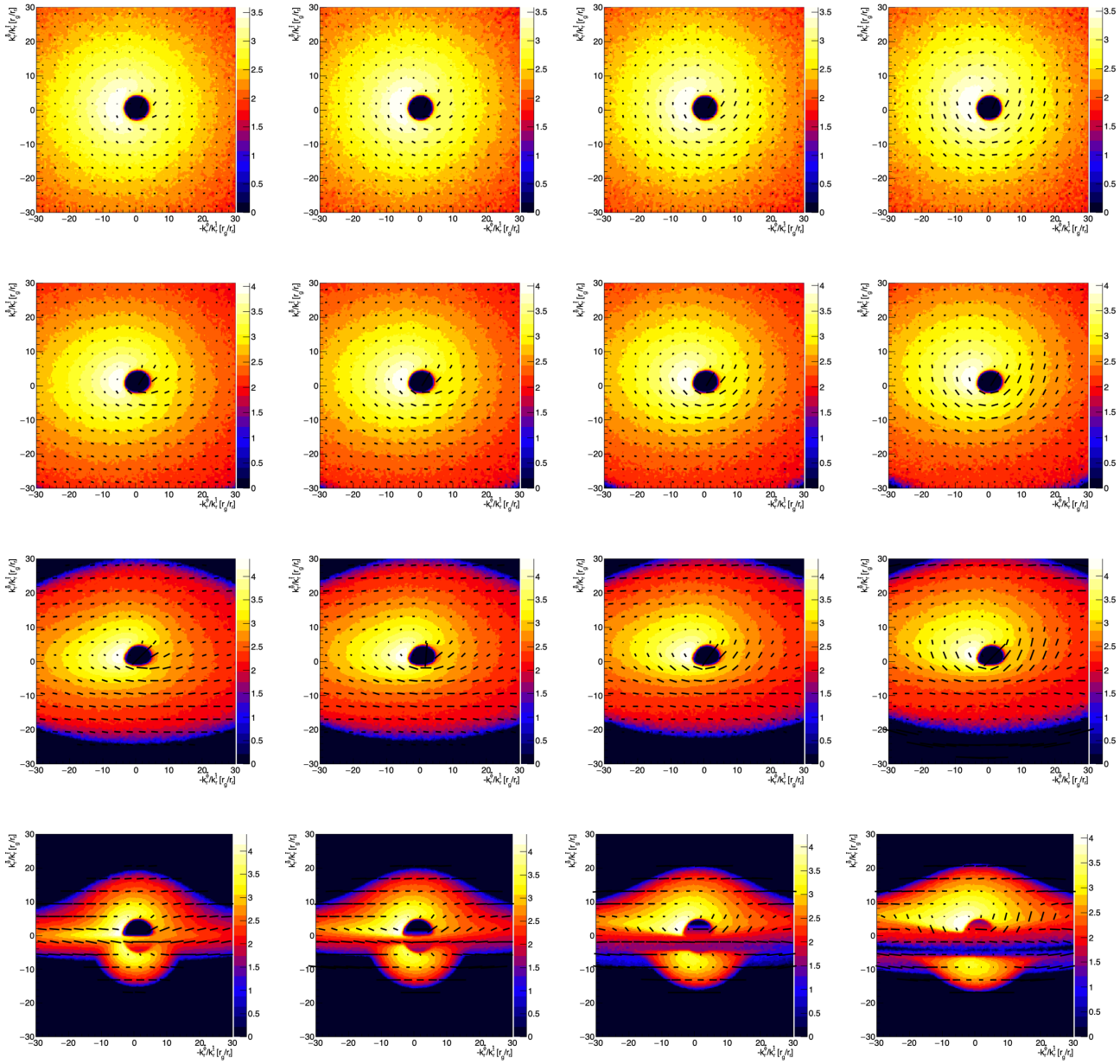

Fig. 2.3: Simulation results for different disk scale heights H (from left to right: H=0.0, 0.1, 0.2, 0.3) and different inclinations I (from top to bottom: i = 25°, 45°,65°, 85°). The color scale gives the total flux (direct and reflected) using a logarithmic color scale. The lengths and directions of the black bars give the linear polarization degree and angle, respectively. The overall polarization degrees increase with increasing inclinations. At the highest inclination, the disk shadows itself, the cooler outer edges (near $50R_g$) blocking some emission from the inner most regions of the disk, as well as some of the lensed emission from below the disk.

itself begins to change, along with the polarization degree and angle, as the scale height increases. The thickness of the torus self-shadows the inner-most regions and the strongly lensed emission from the back, underside of the disk.

Figure 2.4 shows the energy, polarization degree, and polarization angle spectra over four inclinations, $i = 25°, 45°, 65°$, and $85°$. In order to understand the effect that geometric thickness has on the spectra, first examine the case of the thin disk. At energies above ~ 0.5 keV, emitted from the inner regions of the disk, two phenomena in conjunction combine to change both the polarization degree and angle. Firstly, the highly curved spacetime induces a rotation in the polarization vector $\mathbf{f}^\mu$. As $\mathbf{f}^\mu$ is by definition orthogonal to $\mathbf{k}^\mu$, it must rotate as the geodesic transverses the highly curved spacetime near the compact object. At the same time, relativistic beaming due to the motion of the disk both raises and lowers the polarization depending on its emission relative to the observer. On the approaching side, the beaming *lowers* the polarization fraction as the photons are received at a lower effective inclination than they were emitted in the plasma frame; on the receding side the opposite is true, the beaming *raises* the polarization as photons are received at a higher effective inclination [26]. As the flux of returning radiation increases, an effect which is more pronounced in the inner regions of the disk where the curvature is highest, the net polarization begins to increase. The minima in polarization degree observed in these spectra are due to these competing effects between the direct and reflected emission.

Armed with this understanding, the obvious correspondence between the scale height of the torus and the polarization can be explained geometrically. First, due to the increase in surface area there is an increase in the lensed emission from the backside of the disk. This can be seen visually in Figure 2.3 comparing the left-most and right-most images for inclinations of 65° and 85°. An increase in the lower-energy emission being lensed causes the swing in polarization angle from horizontal to vertical to shift to lower energies.

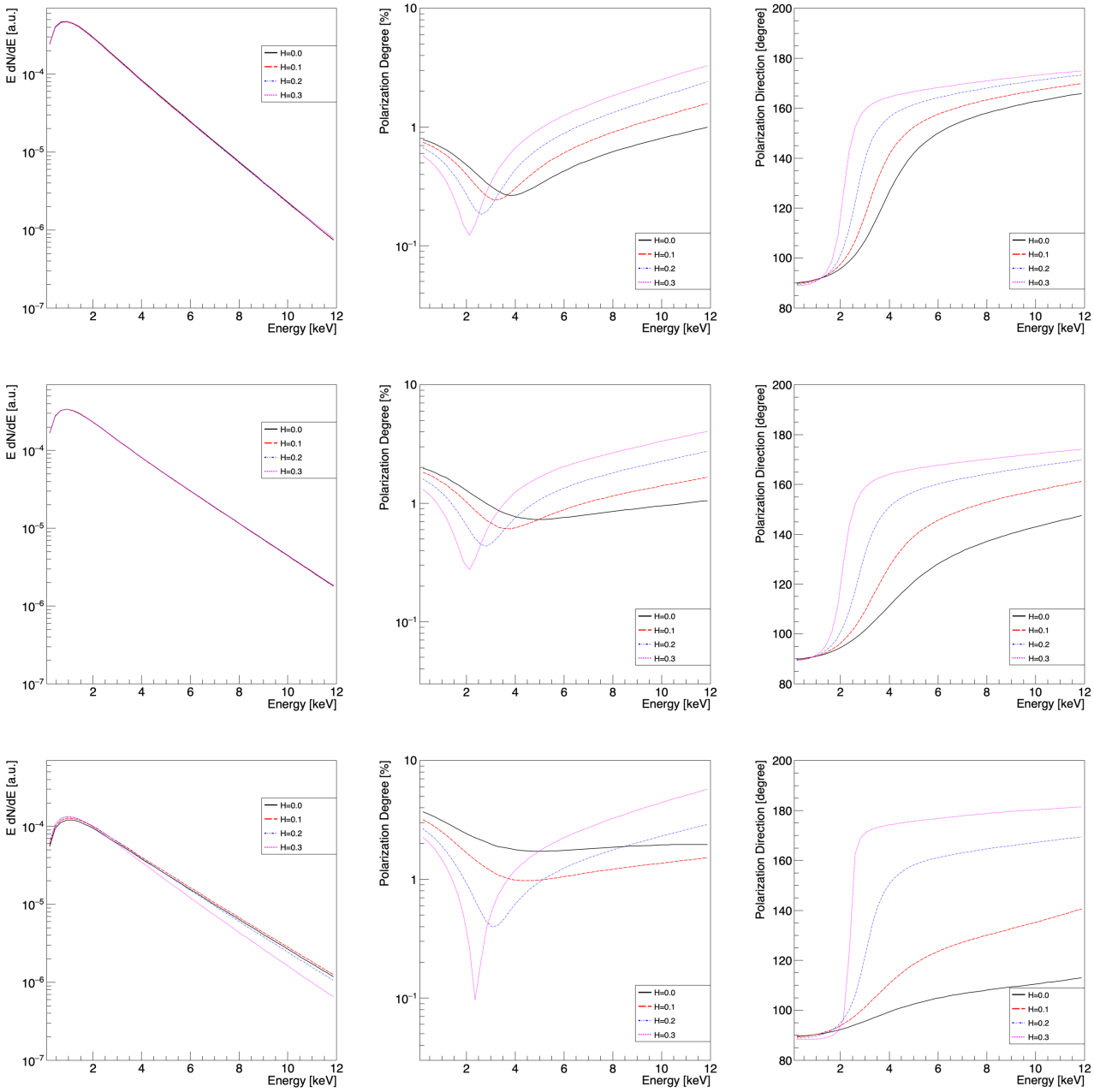

Fig. 2.4: Energy spectra (left), polarization degree (middle), and polarization angle (right) for inclinations of 45° (top row), 65° (middle row), and 85° (bottom row). Flux energy spectra are approximately uniform across scale heights for a given inclination, with the exception of very high - nearly edge on - inclinations where disk self-shadowing becomes apparent. Polarization degree minima shift to lower energies with increasing scale height, as the geometry leads lower energy emission to scatter that would otherwise have gone directly to the observer. This same effect causes the polarization angle to swing from horizontal to vertical at lower energies with increasing scale heights.

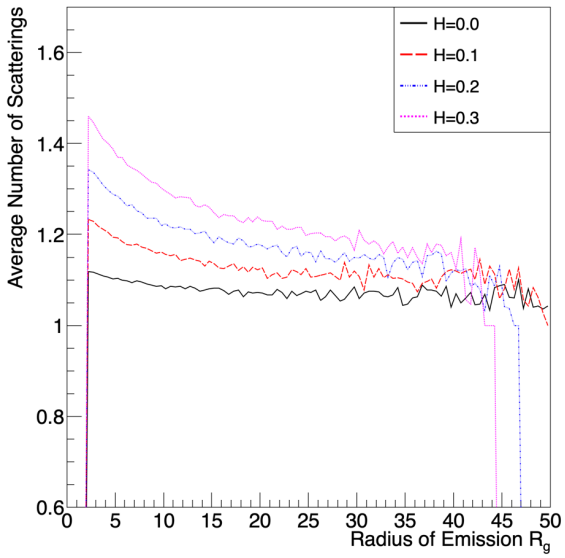

Fig. 2.5: Average number of scatterings for photons emitted from various radii for the thin disk and the three scale heights explored as received by an observer inclination of 65°. Photons launched at small radii, inside the 'doughnut hole' of the accretion flow, scatter more often than photons emitted further out, at the outward facing sides of the disk.

The shift in the minimum of polarization degree is similarly of geometric origin. The apparent minimum in polarization degree is caused by the competition of boosting, which lowers the polarization for high intensity emission, and scattering, which raises the polarization. Firstly, as the thickness increases, the innermost regions of the disk where boosting (both red and blue) has the strongest effect becomes shadowed. Thus, there is less emission from the approaching side, the source of unpolarized high energy emission. The increased lensing from the backside simultaneously adds more polarized high energy emission. Furthermore, as the disk thickness increases, so too does the surface area of the disk, leading to an increase in scattering as shown in Figure 2.5. Due to this geometry, a photon emitted from the inner regions at a very small inclination above the surface will be beamed nearly parallel with the surface. Such photons are effectively beamed back into the disk itself due

to its geometric thickness. This effect becomes more prominent at both larger scale heights and higher inclinations. This increase in scattering at all radii corresponds to a reduction in direct emission and an increase in scattered emission received by the observer, which together with the effect of lensing and self-shadowing pushes the minimum in the polarization degree down to lower energies while increasing the polarization degree at higher energies.

The spin affects the polarization spectra for disks with goemetric thickness similarly to thin disks. As spin increases, we see the minimum in polarization degree and the swing from horizontal to vertical in polarization angle shift to lower energies. Higher spins bring r_{ISCO} closer to the event horizon, which in turn adds returning vertically polarized photons at lower energies as evidenced in Figure 2.6. Overlaying multiple spins for a thin disk and one with a scale height of $H = 0.2$ reveals degeneracies in the polarization spectra. At an inclination of $\theta = 65°$, the polarization degree and angle for $H = 0.0, a = 0.9$ and $H = 0.2, a = 0.6$ are nearly identical below ~ 8 keV.

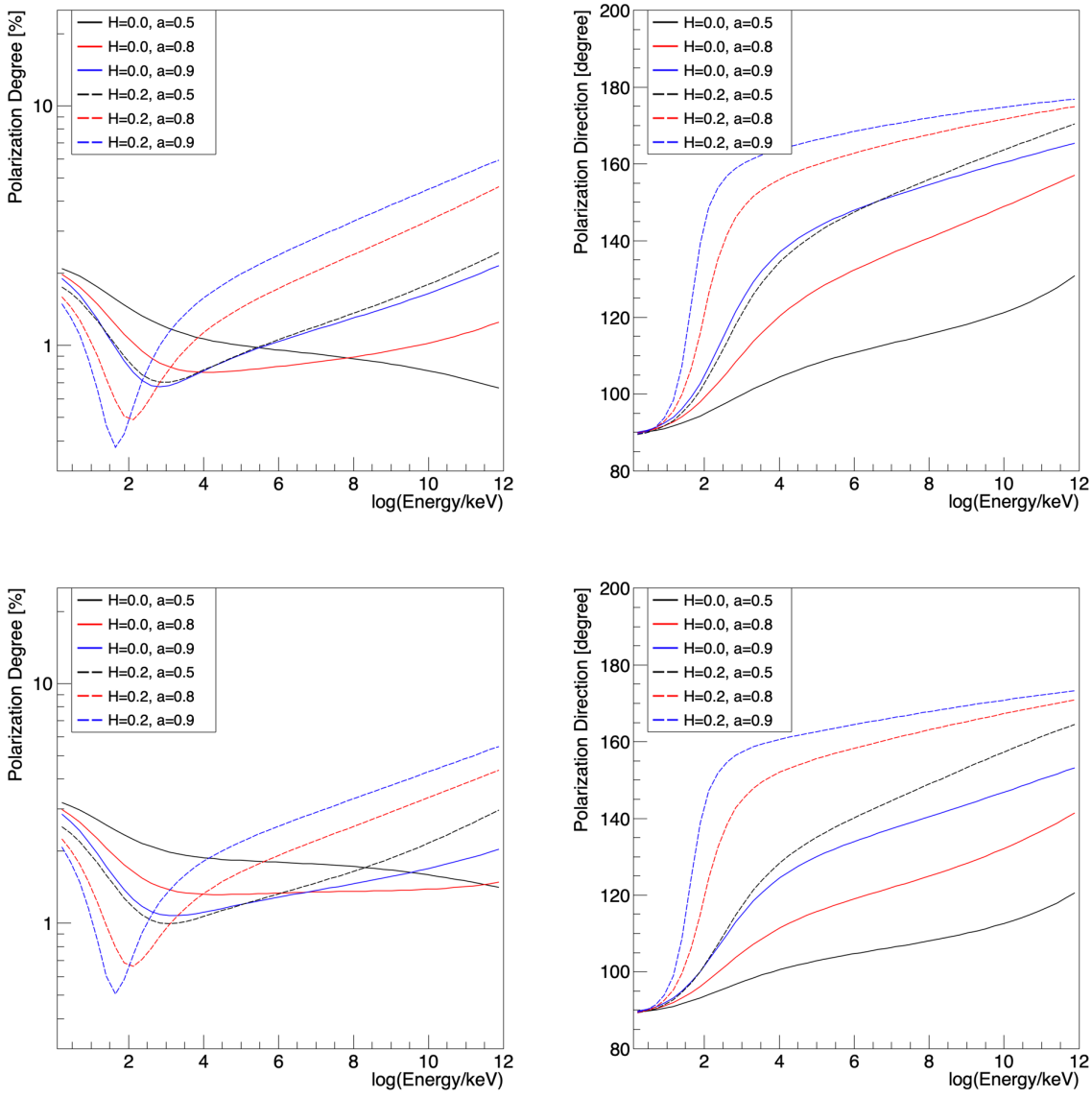

Fig. 2.6: Polarization degree (left) and polarization angle (right) for a thin disk (solid lines) and a toroid (dashed lines) with a scale height of $H = 0.2$ for spins of $a = 0.5, 0.8,$ and 0.9 viewed at inclinations of $i = 65°$ (top) and 75° (bottom). As spin increases, the inner edge of the accretion disk moves closer to the event horizon and there is more emission in the highly curved regions around the black hole. This, in turn, causes the minimum of polarization degree and the swing from horizontal to vertical in polarization angle to shift to lower energies.

2.6 Discussion

This chapter has explored the effect of geometric thickness on the polarization spectra of accreting stellar mass black holes over a range of spins and luminosities. In general, increases in geometric thickness correspond to increases in polarization degree at energies above ~ 4 keV while yielding lower polarization degrees for energies below ~ 3 keV. This trend is due to the geometry itself, owing partly to increases in the amount of scattering in the inner regions of the disk where higher energy emission originates, and decreases in the amount of scattering in the outer regions of the disk which correspond to lower energy emission.

Across all observer inclinations, for all spins, the increasing disk thickness shifts the polarization degree minimum and the swing in polarization angle from horizontal to vertical to lower energies. The trend is, in general, due to the competing effects of direct and reflected emission in concert with lensing from the far side of the disk. The effect is exacerbated in the geometrically thick disks. Thick disks self-shadow their innermost regions, where doppler boosting depolarizes the high energy emission, which - in concert with the increased scattering in these regions - raises the polarization degree at higher energies. Additionally, there is more lensed emission from large radii from the far side of the disk, which shifts the swing in polarization angle down to lower energies.

Increases in black hole spin on the spectra have a similar effect between thin and thick disks, bringing the inner edge of the accretion disk to smaller and smaller radii and in so doing lowering the polarization degree minimum and swing in polarization angle to lower and lower energies. There are degeneracies that exist between spin and scale height, as noted in in Figure 2.6, particularly for higher inclination angles. As an example, a thin disk with a spin of $a = 0.9$ and a slim disk of scale height $H = 0.2$ and spin of $a = 0.5$ show approximately identical polarization degree and angle below $\sim 8keV$. A larger parameter

space study would likely yield other degeneracies; this is left to future work as the goal here was simply to establish whether any such degeneracies exist at all.

Chapter 3

General Relativistic Magneto-Hydrodynamical Simulations with H-AMR

3.1 Introduction

This chapter details the data set which is the focus the rest of this thesis. The data set was produced with the GRMHD code *H-AMR* [78], which was conceived and produced by Matthew Liska et al. and is based on the publicly available *HARMPI* [111] code. The data concerns a highly inclined, very thin accretion disk around a highly spinning stellar mass black hole, and its dynamical evolution through multiple tearing events and periods of precession. This chapter has two sections. The first will review *H-AMR*, its basic operational alogrithm and the clever computational adaptions that allow it to resolve thin disks. The following section will review the dataset itself. This section will specifically focus on the physical mechanisms driving the tearing events and the dynamism of these events, which make this dataset so unique. The final section will review the oscillatory signals found in the

dataset, relating these signals back to the characteristic frequencies of the orbiting plasma that produces them. All of the figures in this chapter were made from the *H-AMR* data files produced for integration into xTrack. Due to the limited resolution of the datasets (in comparison with the original GRMHD data), there are artifacts - blank spaces or lines - which appear. These have been left in the plots, as efforts to smooth them reduce the overall quality of the output.

3.2 The Current State of the Art - *H-AMR*

H-AMR is branched from [111], a version of the publicly available*HARM2D* code. The code can utilize multiple metrics and coordinate systems, but this work shall be concerned with the Kerr-Schild formulation of the Kerr metric, with the additional adaption of a logarithmic radial coordinate (i.e., $r \rightarrow log(r)$). Kerr-Schild coordinates are non-singular at the event horizon, allowing particle trajectories to be tracked through r_{EH} to the singularity at $r = 0$.

The numerical scheme has a cell maximum resolution of $N_r \times N_\theta \times N_phi = 13440 \times 4608 \times 8096$. The code integrates the conservative GRMHD equations,

$$\frac{\partial \mathbf{U}(\mathbf{p})}{\partial t} = \frac{\partial \mathbf{F}_r(\mathbf{p})}{\partial x^r} - \frac{\partial \mathbf{F}_\theta(\mathbf{p})}{\partial x^\theta} - \frac{\partial \mathbf{F}_\phi(\mathbf{p})}{\partial x^\phi} + \mathbf{S}(\mathbf{p}), \tag{3.1}$$

where $\mathbf{U}(\mathbf{p})$ is the vector of conserved quantities (particle number density, energy density,...), $\mathbf{F}_i(\mathbf{p})$ is the vector of fluxes corresponding to $\mathbf{U}(\mathbf{p})$, and $\mathbf{p}$ is the vector of primitive variables (velocity, internal energy, density,...). $\mathbf{S}(\mathbf{p})$ is the source term, accounting for the effects of the strong gravity on the spacetime, radiative interactions in the gas, and other physical processes. At each time step t_i the fluxes at each cell face are computed and the source terms are added at the cell centers, allowing the conserved quantities to be computed at

t_{i+1}. The magnetic field is evolved on the cell faces and the electric field calculated along cell edges in a staggered grid to ensure a divergence free evolution of $\mathbf{B}^{\mu}$.

The 'AMR' in *H-AMR* stands for Adaptive Mesh Refinement [112, 113], a feature which allows the code to adjust its spatial resolution as needed, increasing the resolution in regions of interest and reducing it in regions with low dynamical variability. This enables *H-AMR* to resolve features which would otherwise occupy only a fraction of a computational volume. In addition to refining the spatial grid, *H-AMR* also has the ability to adjust the time-stepping of the integration cell-by-cell, known as Local Adaptive Timestepping (LAT). The code is fully parallelized and GPU accelerated, which in conjunction with the AMR and LAT result in 5 orders of magnitude performance increase compared to traditional, non-AMR, CPU based GRMHD.

3.3 Characteristics of Thin, Misaligned Disks

The dataset that is the subject of the rest of this thesis was produced with *H-AMR* on the Summit supercomputer at Oak Ridge National Lab. The simulation ran for 5 million NVIDIA V100 GPU-hours (equivalently 800 Milion Sky Lake CPU core-hours). The disk was initialized for a black hole of $10M_{\odot}$ with a spin of $a = 0.9375$ surrounded by a torus in hydrostatic equilibrium [114] at a tilt of $\theta_{tilt} = 65°$. The disk is initially given a Keplerian velocity distribution and is seeded with a poloidal magnetic field. The plasma in the disk is artificially cooled to a target scale height of $H = 0.03$ by allowing the internal energy to exponentially decay, with the time constant of the decay determined by the orbital time scale [65].

3.3.1 Tearing Events

Immediately upon initialization the disk begins to precess, though it takes $t \simeq 10,000\frac{r_g}{c}$ to cool to from the toroid it is initialized as to a thin disk with a scale height of $H = 0.03$. Lense-Thirring torques begin to warp the disk soon after initialization and, as these warps build, the viscous stresses in the disk become unable to transport angular momentum outward rapidly enough to counteract these differential torques. Eventually the Lense-Thirring torques exceed the viscous torques holding the disk together, causing the disk to tear apart.

The disk is held together by its own viscosity, and following the derivations of Nixon et al. [77] (and Frank et al. [115]), the radius of the tearing event can be estimated. The azimuthal viscous force per unit area is given by

$$\mathbf{f}_v = \mu r \frac{d\Omega}{dr}, \tag{3.2}$$

where μ is the dynamical viscosity, and $r\frac{d\Omega}{dr}$ is the rate of shear [77]. Letting the area of the interface between two disk segments be $2\pi rH$ (where H is the scale height of the disk) and the kinetic viscosity be $v = \frac{\mu}{\rho}$, the total force in the azimuthal direction can be written as

$$\mathbf{F}_v = 2\pi\Sigma v r^2 \frac{d\Omega}{dr}, \tag{3.3}$$

where $\Sigma = \rho H$ is the integrated surface density. The torque due to viscosity is then

$$G_v = |\mathbf{r} \times \mathbf{F}_v| = -2\pi\Sigma v r^3 \frac{d\Omega}{dr}. \tag{3.4}$$

The Lense-Thirring precession frequency is $\mathbf{\Omega}_{LT} = (2G\mathbf{L}_{BH}/(c^2 r^3))$ (numerous derivations can be found in [116, 25, 6]), where $\mathbf{L}_{BH} = aGM^2/c$ is the angular momentum of

the black hole. For an approximately Keplerian orbit (i.e., $\Omega^2 \approx GM/r^3$), and a disk with angular momentum $L_{disk} = \rho H r^2 \Omega$, this precession induces a torque on the disk of

$$G_{LT} = \ 2\pi r H |\mathbf{\Omega}_{LT} \times \mathbf{L}_{disk}| = \ 2\pi H |\Omega_{LT}| \Sigma r^3 |\Omega \sin\theta|. \tag{3.5}$$

Here, θ is the angle between the angular momentum of the disk and the black hole. Tearing occurs when $G_{LT} > G_v$. For a thin, quasi-keplerian α disk [50], the radius of the expected break is then

$$R_{break} < \left(\frac{4ar}{3\alpha H} |sin(\theta)| \right)^{2/3} r_g, \tag{3.6}$$

where $r_g = GM/c^2$ is the gravitational radius. As the Lense-Thirring torques interact with the disk and induce warps, $\mathbf{L}_{disk}$ develops a strong radial dependence. At high enough spins and inclinations, this leads to multiple tearing radii, resulting in concentric precessing rings of matter as shown in [77]. From Equation 3.6, the high spin of the black hole and highly misaligned, very thin disk considered here is expected to undergo tearing as the disk warps and precesses from its high misalignment towards an equatorial alignment.

Indeed, there are 10 distinct episodes of tearing which occur over the $150,000\ r_g/c$ run time of the simulation. Of these ten events, 8 have very short durations (less than $\sim 5500\ r_g/c$), wherein the disk tears and very quickly reforms as a single misaligned disk. The two remaining tearing events, which shall be referred to as T1 and T2 moving forward, have durations of $42,282\ r_g/c$ (T1) and $26,865\ r_g/c$ (T2). The analysis that follows in Chapter 5 will focus on these two tearing events, with the majority of the focus given to T1 as the simulation ends during the T2 tearing event.

3.3.2 Precession and Bardeen-Petterson Alignment

The tearing events are preceded by rings of high density that form across the disk. As the plasma flows inwards and accretes, so too do these rings of density as is evidenced in Figures 3.1-3.3. In both T1 and T2, the tearing event starts when the ring reaches $\sim 20r_g$.

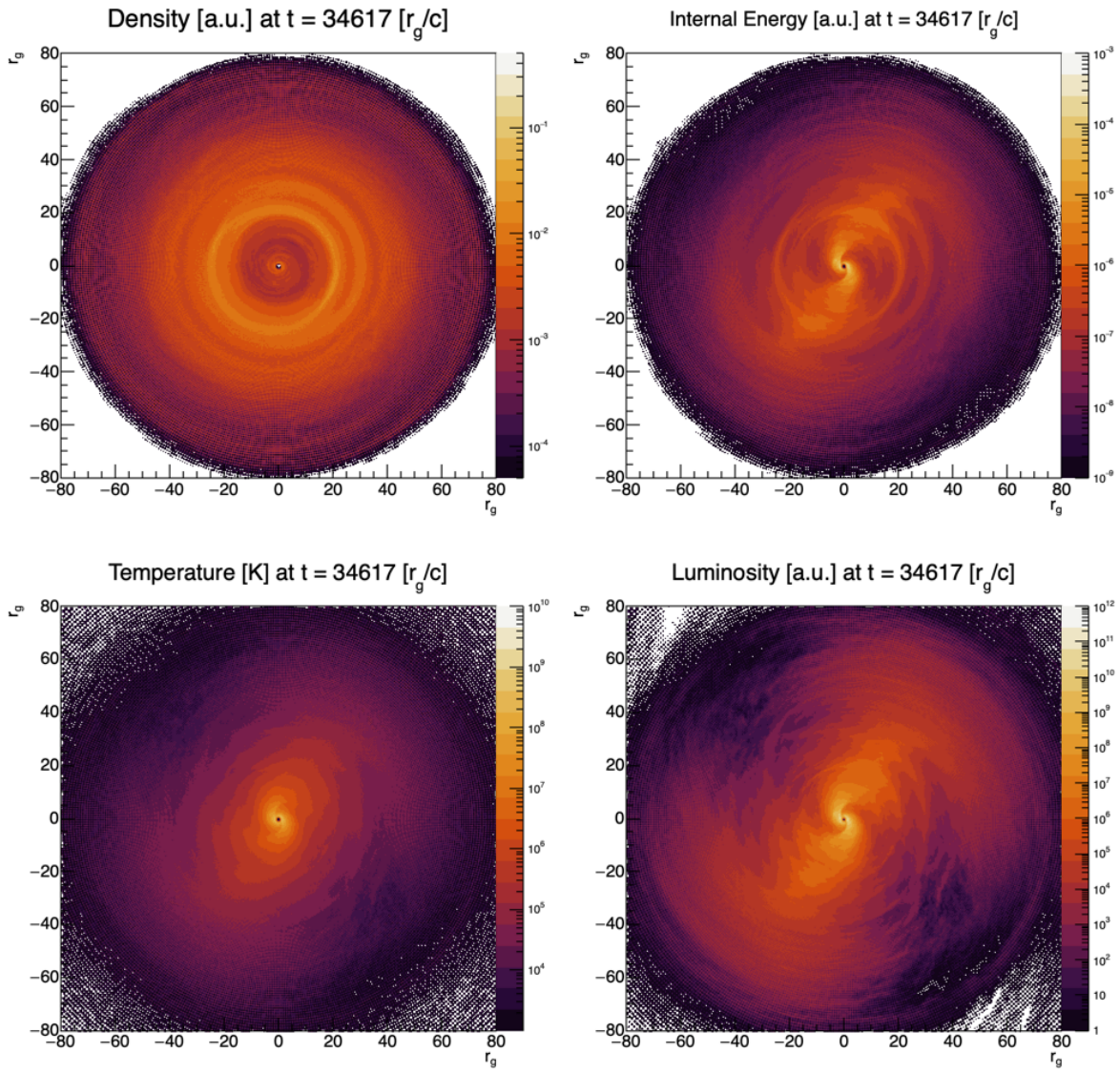

Fig. 3.1: Density (top left), Internal Energy (top right), Temperature (bottom left), and Luminosity (bottom right) immediately preceding the tearing event. Note the ring structures in density and internal energy, the most prominent of which is at $20 - 30\ r_g$.

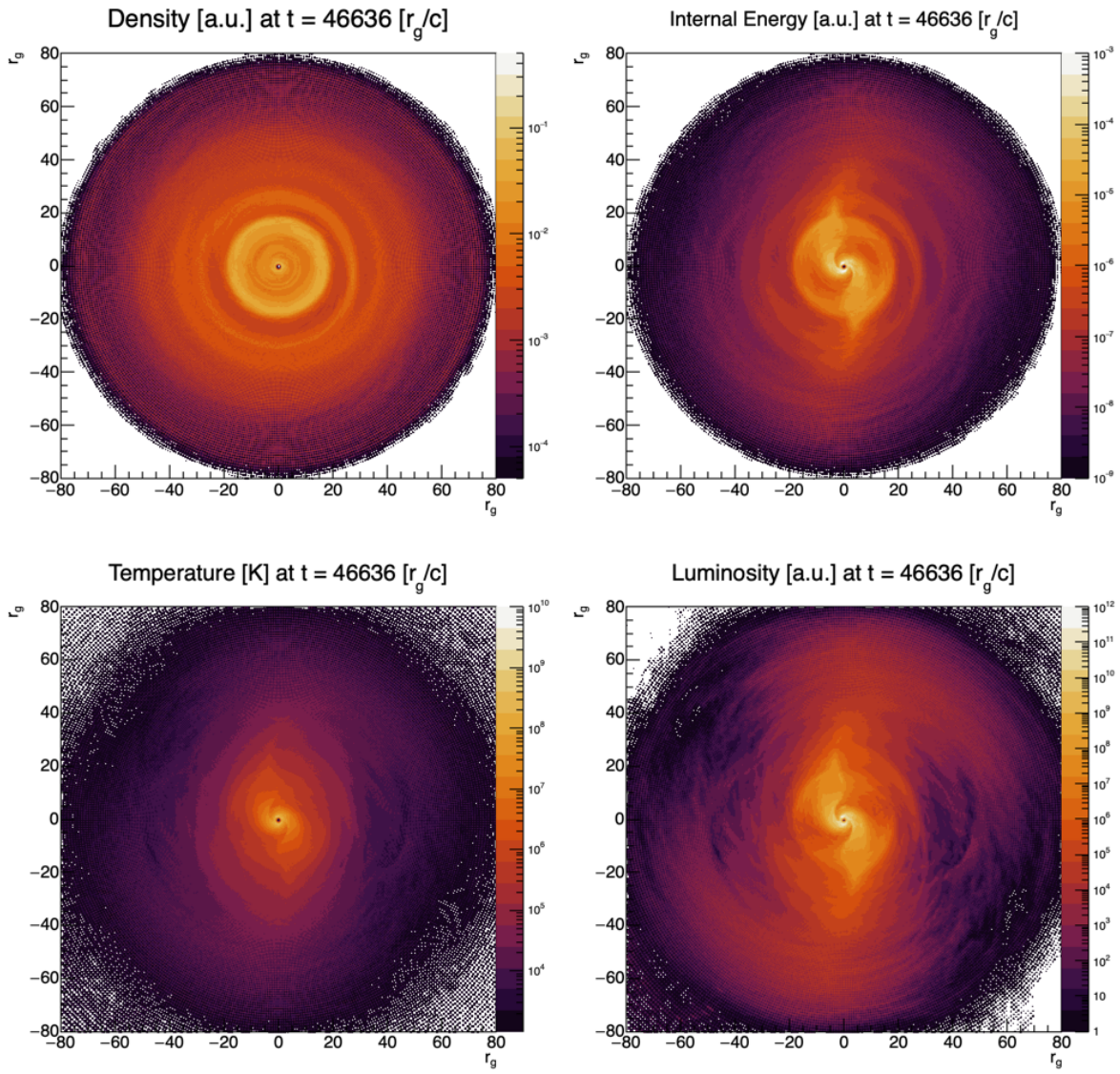

Fig. 3.2: The most prominent ring of density from Figure 3.1 has moved inward and is now at $r < 20r_g$, while density and internal energy across the entire inner disk have increased.

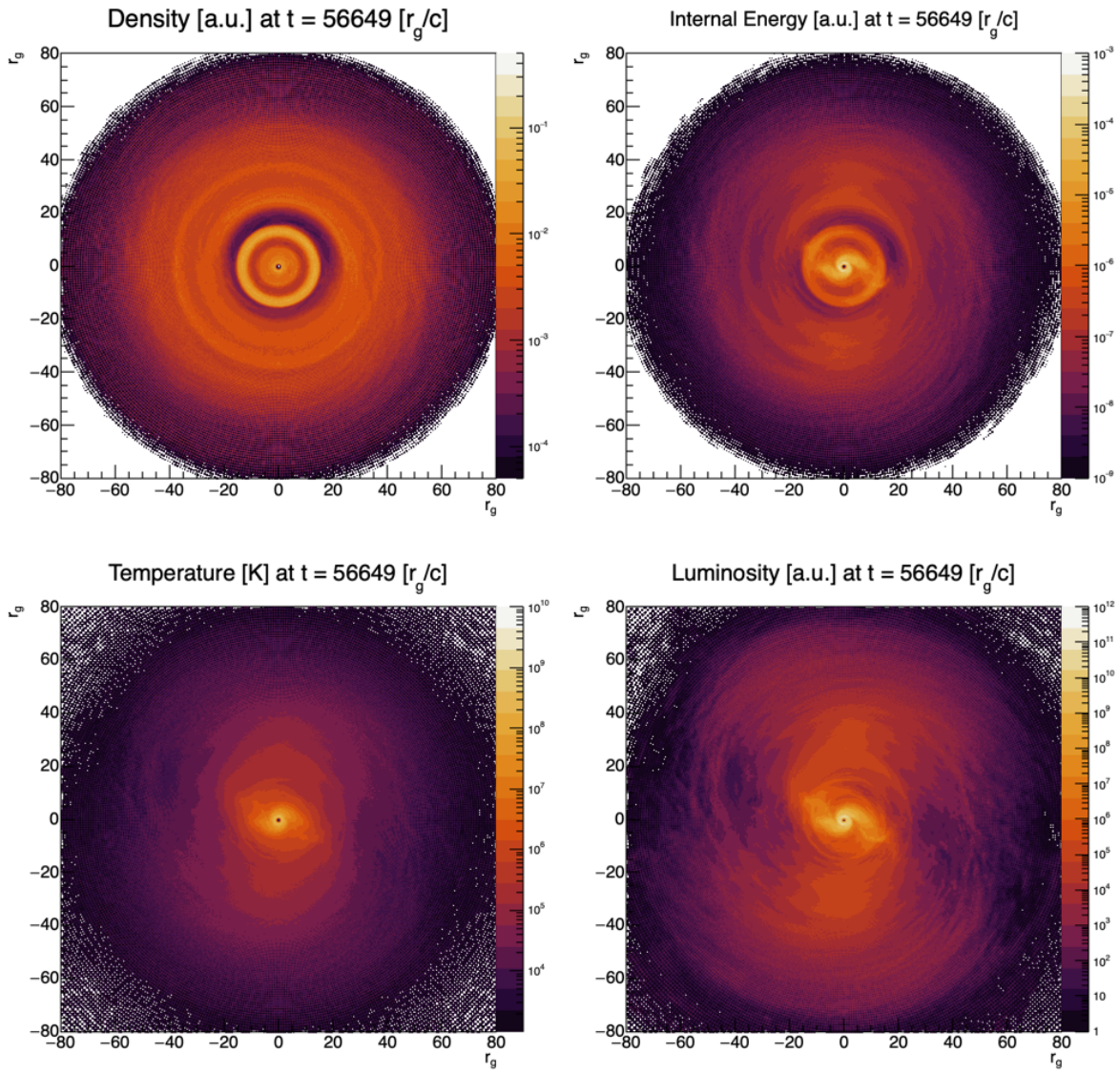

Fig. 3.3: There is now a more apparent separation between the inner and outer disks, with there being a dense ring on the outside of the inner disk. Note the presence of an additional density ring at $\sim 40 r_g$.

When the disk tears, the inner disk begins a rapid, differential Lense-Thirring precession, while the slow precession of the outer disk remains more-or-less unchanged. The tearing events are most easily identified by the sharp discontinuity that occurs in the tilt and precession angles [81] as is evidenced in Figure 3.4. This figure shows the tilt angle as measured from the black hole spin axis (left) and precession angle as measured from an arbitrary $\phi = 0°$ (right) which is constant for all times. The tilt and precession are plotted here as functions of radius (vertical axis) and time (horizontal axis). In particular in the plot of precession, sharp discontinuities between $\sim 40,000$ and $\sim 80,000 r_g/c$ are the periods of differential precession of the inner disk during the tearing event.

Following the procedure of Fragile and Anninos [73] and Nelson and Papaloizou [117], the tilt and precession angle can be calculated as

$$\theta_{tilt} = cos^{-1}\left(\frac{\mathbf{L}_{BH} \cdot \mathbf{L}_{disk}}{|\mathbf{L}_{BH}||\mathbf{L}_{disk}|}\right) \tag{3.7}$$

$$\phi_{prec} = cos^{-1}\left(\frac{\mathbf{L}_{BH} \times \mathbf{L}_{disk}}{|\mathbf{L}_{BH} \times \mathbf{L}_{disk}|}\right), \tag{3.8}$$

where, as in the preceding section, $\mathbf{L}_{BH}$ and $\mathbf{L}_{disk}$ are the angular momenta of the black hole and the disk, respectively.

In T1, the inner disk precesses for 5 cycles before accreting into the black hole. During these cycles, the disk enters a Bardeen-Petterson alignment [92] as shown in Figure 3.5, and in so doing undergoes another tearing event which is again preceded by a differentially precessing ring of density. During this period there are two inner disks (sub-disks). To avoid confusion, the innermost sub-disk will be called inner disk 1, and the outermost inner sub-disk will be called inner disk 2. The alignment begins in the innermost regions of the inner disk 1 and propagates outward to $\sim 5r_g$. This alignment is accompanied by an increase in

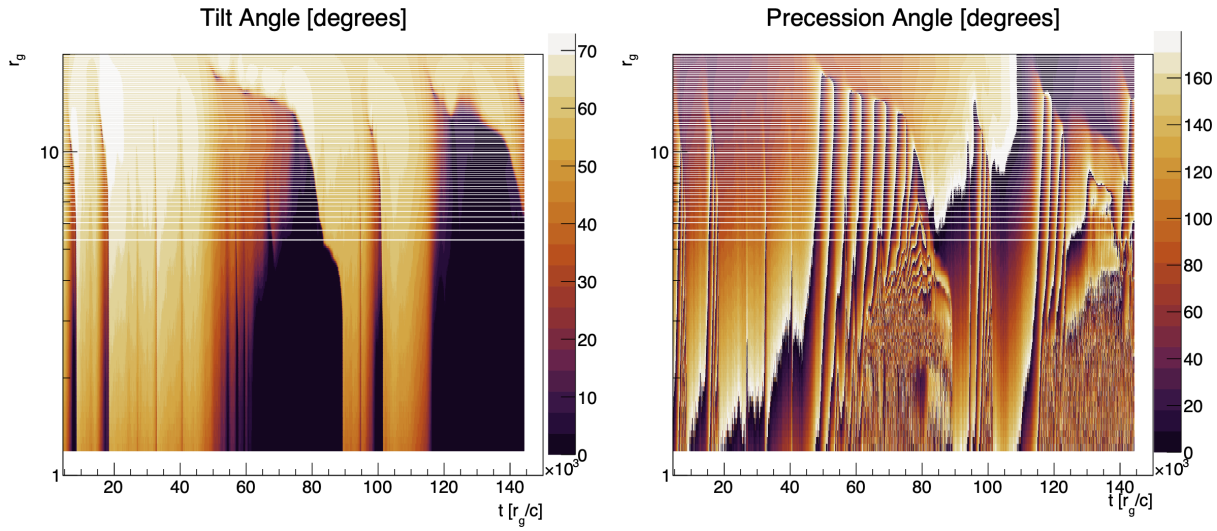

Fig. 3.4: Plots of the tilt angle (left) and precession angle (right) over the entire runtime of the simulation for $1 \leq r \leq 20$. There is a coincidence of discontinuities that occur in each plot corresponding to tearing events. In particular, on the plot of precession angle for $\sim 40,000 r_g/c \leq t \leq \sim 80,000 r_g/c$, the multiple consecutive discontinuities correspond to the 5 precessions of the tearing cycle T1. White horizontal lines on both plots are artefacts from the log(r) binning of the data sets.

density in this region, which is speculated to be sourced from a reduction of the infall speed of the plasma in the absence of warp. An additional alignment occurs from the outside of inner disk 2 and moves inward on a timescale comparable to the accretion time of the inner disk system. This is thought to be due to angular momentum cancellation as matter is fed from the outer disks to the inner disks via 'streamers' [81, 80], cancelling θ components of the disk's momentum in the process (though the exact cause is still being explored[1]).

While these 'streamers' feed gas from one adjacent sub-disk to the next, the inner disk system is eventually disconnected from the outer disk (see Figures 3.5-3.7). From here inner disk 2 transfers more mass to the aligned inner disk 1, increasing the density and catalyzing

[1] The effective viscosity in this simulation exceeded the sum of the Maxwellian and Reynolds viscosities by more than an order of magnitude, indicating that stresses due to local α-viscosity cannot be responsible for angular momentum transport [80].

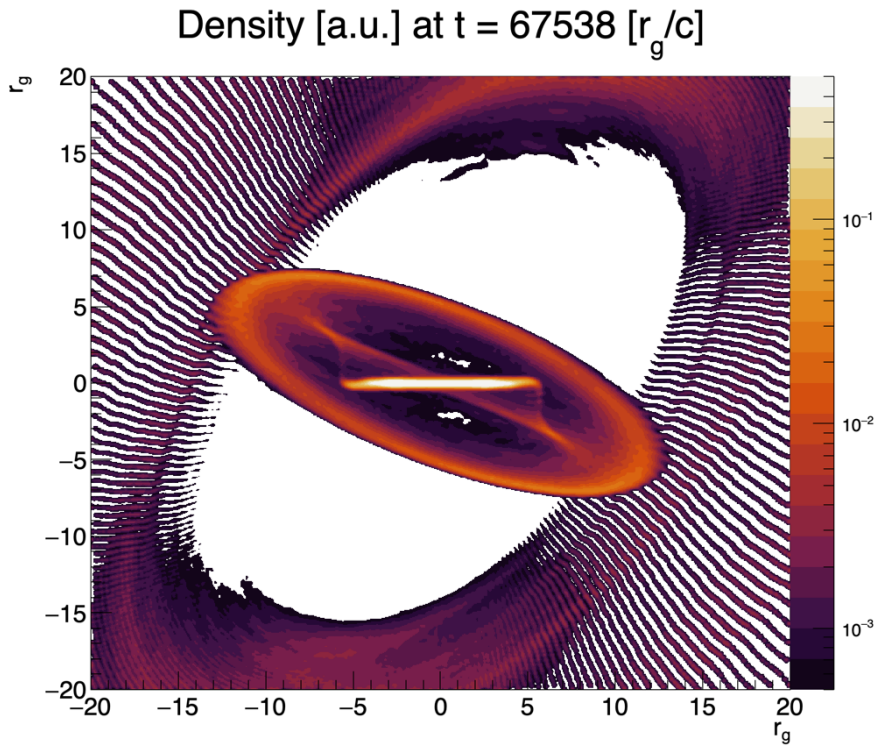

Fig. 3.5: The two inner sub-disks during Bardeen-Petterson alignment. Note the ring of high density at the outer edge of the larger inner sub-disk (inner disk 2), and that the density of the innermost, aligned sub-disk (inner disk 1) is approximately an order of magnitude higher than the precessing inner sub-disk.

an increase in the accretion rate (as will be explored in the next section). More mass accretes from the inner disks with each precession, and the difference in the Lense-Thirring precession rate of the inner sub-disks gets continually smaller. As the mutual alignment of the two inner disks increases in concert with a rise in the accretion rate, the radial extent of the inner disk system diminishes. Simultaneously, the extent of the outer disk moves to smaller and smaller r, with streamers reconnecting with the inner disk system and their density gradually increasing. These processes continue until the entire disk reforms as a single, inclined body, only to tear again at a different radius some time later[80].

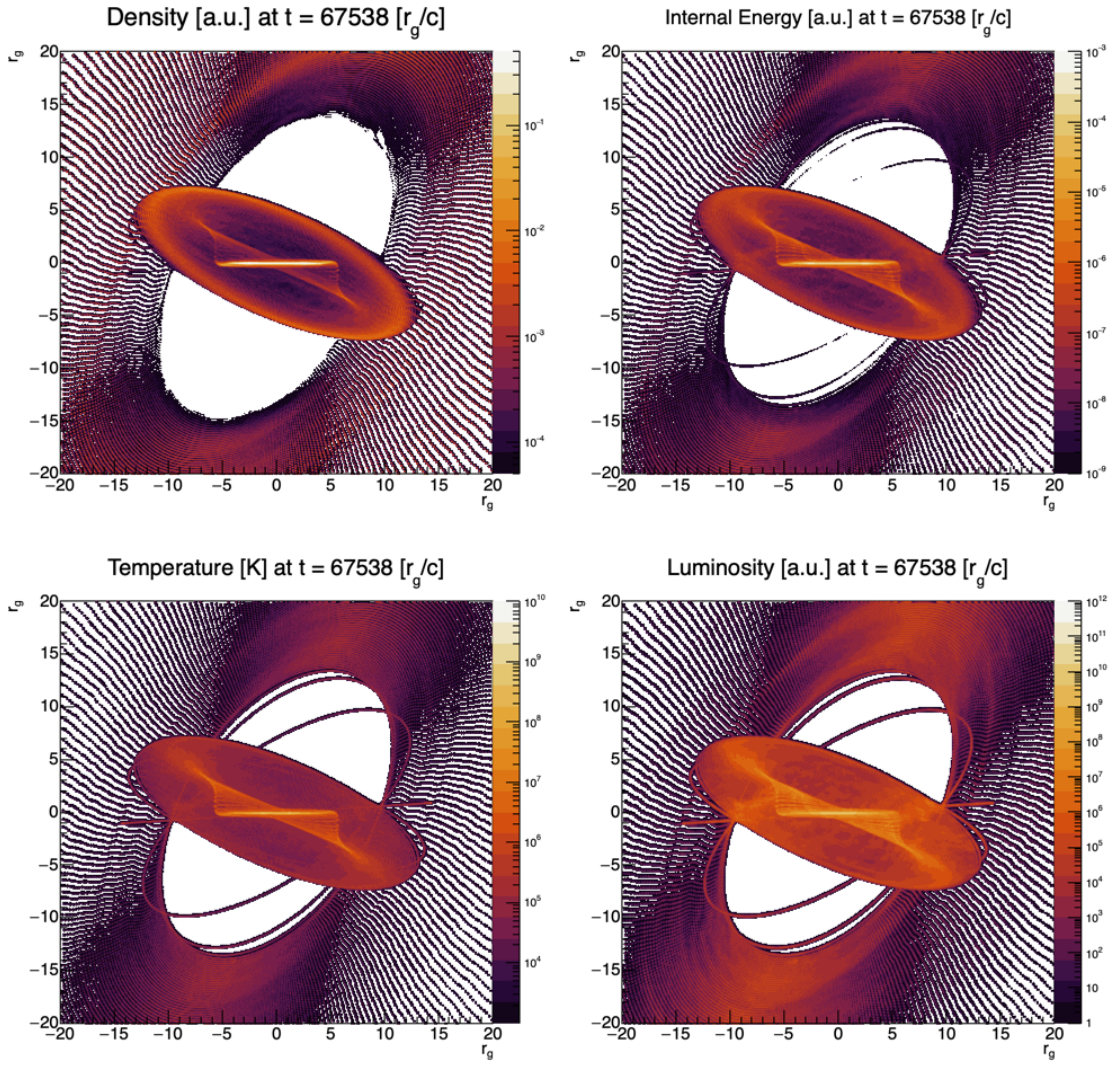

Fig. 3.6: The two inner sub-disks during Bardeen-Petterson alignment.

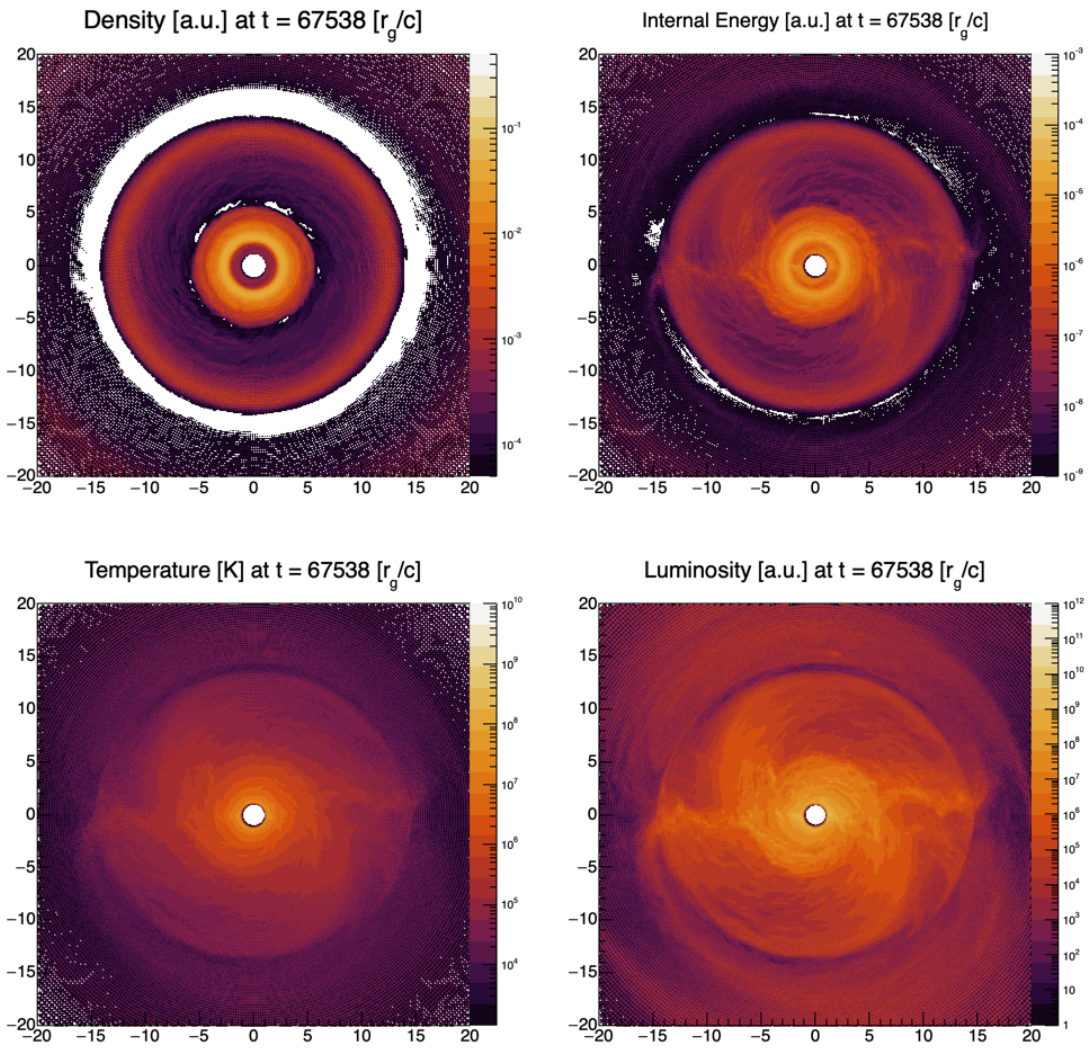

Fig. 3.7: There is now a more apparent separation between the inner and outer disks. Note the second tear that has opened up between the aligned innermost sub-disk, and the precessing inner sub-disk.

3.3.3 Oscillatory Behavior During Tearing Events

As mentioned above, tearing events are all accompanied by a spike in the accretion rate (see Figure 3.8) over the duration of the tearing event. This increase in $\dot{M}$ is spurred by a decrease in the infall speed of the gas as the inner disk aligns, leading to an increase in the density.

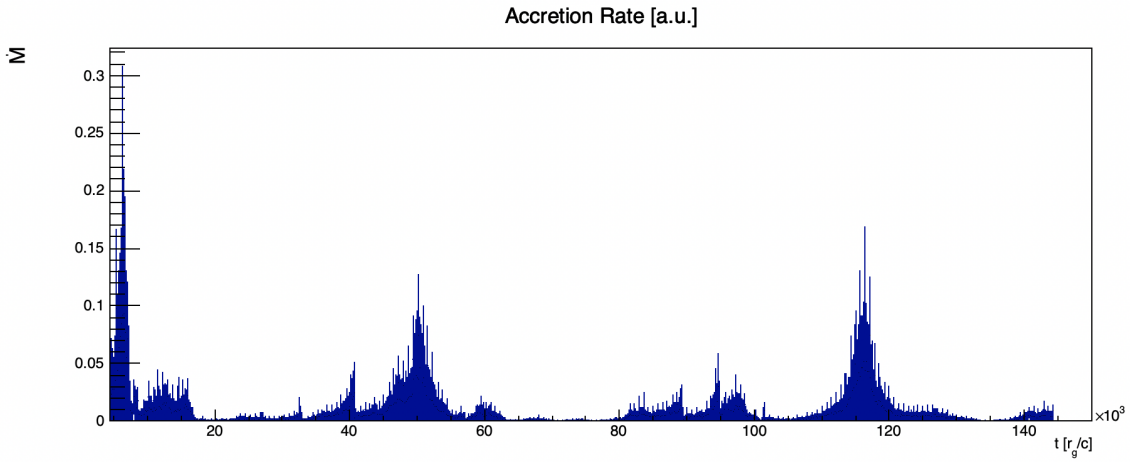

Fig. 3.8: The accretion rate $\dot{M}$ in arbitrary code units as calculated over the null surface of the event horizon over the full run time of the simulation. There are large, long duration increases in $\dot{M}$ that occur with each tearing event (i.e., three large increases between $\sim 40,000-60,000\ r_g/c$. Additionally, these are accompanied by short duration spikes, the magnitude of which tend to be larger when the baseline accretion rate is higher (e.g., compare the short spikes at $50,000\ r_g/c$ to those at $50,000\ r_g/c$).

More interestingly, there are high frequency oscillations in the radial accretion rate, $\dot{M}_r$, at distances corresponding to the tearing radius as outlined in detail in Musoke et al, 2023 [81]. Binning the accretion rate over T1 into radial bins (whereby the rate is calculated as the integrated density flux through a given radial shell), $\dot{M}_r$, reveals power dissipated at frequencies corresponding to an epicyclic mode of the density rings just inside the tearing radii of the two inner sub-disks. Specifically, there is a 55Hz oscillation located

at $13r_g \leq r \leq 14.5r_g$ corresponding to a radial epicyclic oscillation at $\sim 13r_g$ (see Figure 3.9). There is an another, weaker oscillation observed at 110Hz located at the same radii.

In addition to the Keplerian and Lense-Thirring frequencies, the radial and vertical epicyclic frequencies represent two additional characteristic frequencies of an orbital system. These epicyclic frequencies represent modes of oscillation given a perturbation in θ or r at a given orbital radius and are functions of the mass M (here in natural units of $M = 1$) and spin a of the black hole. From Nowak and Leher (1999)[118] with $\Omega_K^2 = \frac{GM}{r^3}(r^{3/2} + a)^{-2}$ and $\Omega_{LT} = \frac{GMa}{\pi c^2 r^3}$ the radial and epicyclic frequencies are

$$\omega_r^2 = (1 - \frac{6}{r} + \frac{8a}{r^{3/2}} - \frac{3a^2}{r^2})\Omega_K^2 \tag{3.9}$$

$$\omega_\theta^2 = (1 - \frac{4a}{r^{3/2}} + \frac{3a^2}{r^2})\Omega_K^2 \tag{3.10}$$

Musoke et al. also found indications of a possible low-frequency oscillation associated with the Lense-Thirring precession of the inner disk, which had a frequency of $\sim 2 - 4$Hz at $10r_g$. Lense-Thirring precession has been thought to give rise to low-frequency QPOs, [36, 72].

3.3.4 Discussion

Observational evidence supports the idea that many black holes accretion disks are misaligned with the black hole spin axis. Jets in stellar mass black holes have displayed periodic brightening during outbursts [55], a seeming indication of precession. A statistical study of a set of Seyfert galaxies showed an approximately random distribution of jet inclinations with respect to the plane of the host galaxy [57] which is a likely indication of a misaligned and/or warped accretion flow. TDEs have also displayed indications of initial misalignment followed

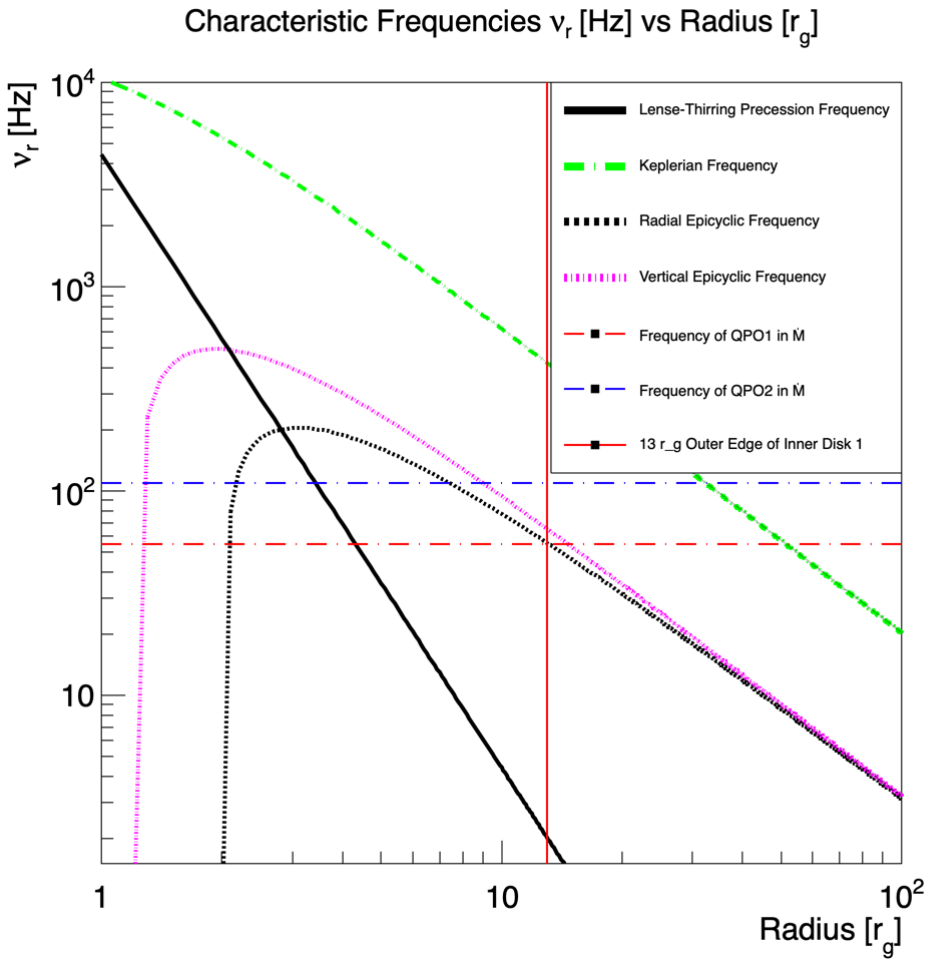

Fig. 3.9: Lense-Thirring precession (thick-black), Keplerian (dash-dot green), radial epicyclic (dashed black), and vertical epicyclic (dash-dot pink) frequencies as functions of radius. The vertical red line is the tearing radius for tearing event T1. The horizontal dash-dot blue and red lines correspond to the oscillations found in the power-spectrum of $\dot{M}$.

by precession and magnetic arrest [56]. This misalignment naturally induces warps in the disk due to Lense-Thirring torques, which cause the disk to precess and can, under the right conditions, induce tearing events which lead to a precessing quasi-Bardeen-Petterson alignment. This precession is a popular explanation for lfQPOs as the frequencies of these signals are commensurate with the Lense-Thirring frequencies in the inner regions of the disk where

precession is expected. Additionally, these warped and misaligned disks are expected to exhibit significant increases in luminosity [119]. The observation of both hfQPO-like behavior in the accretion rate and the precession of the innerdisk over many cycles in this simulation motivate the following study of the spectral, polarimetric, and time domain characteristics of this dataset that follows. Additionally, as warped and precessing disks are often associated with powerful jets in nature and because variations in the centroid of the Fe-Kα line have been observed concurrently with lfQPOs [37], the effect of this evolving geometry on Fe-Kα line profiles is explored.

Chapter 4

Raytracing GRMHD Data in Kerr-Schild Coordinates

4.1 Introduction

Chapter 4 details the changes required in xTrack in order to accommodate Kerr-Schild formulation of the Kerr metric and integrate the data from *H-AMR*. In the following sections, the transformation of the metric into Kerr-Schild coordinates is explored in detail and some fundamental conserved quantities and characteristic radii are derived. The specifics of the data read in from *H-AMR* is also detailed, along with the calculations required to convert the arbitrary 'code units' into real, physical quantities. The raytracing code - specifically the changes required to raytracing this asymmetric and evolving disk structure - is reviewed, and the scattering algorithm and tetrad construction are covered in detail. The chapter ends with sections on the validation of the code completed by comparing an artificial thin disk - created by projecting a frame of the *H-AMR* data into the equatorial plane - with a classic thin disk constructed with the treatment of Page and Thorne (1974)[52].

4.2 Kerr-Schild Spacetime

Boyer-Lindquist coordinates are the most common formulation of the Kerr metric and are particularly useful in astrophysical problems. Their popularity is due to the convenient properties they render in the metric, for example they minimize the number of off-diagonal elements (leaving only mixed terms in $g_{t\phi}$), greatly simplifying calculations as was shown in Section 2.2.1, and reduce the spacetime to the metric of Schwarzchild in the limit $a \to 0$. There are, however, some applications where these coordinates are ill-suited, not least of which involves probing the event horizon. The Kerr metric in the form given in Equation 2.3 is contains a coordinate singularity at $r = M + \sqrt{M^2 - a^2}$. This is not a true singularity, as evidenced by the Kretschmann scalar, $R_{\mu\nu\rho\delta}R^{\mu\nu\rho\delta}$, being finite at the horizon [6, 25], and as such is removable given an appropriate parameterization of the spacetime.

The singularity of Boyer-Lindquist coordinates is problematic for GRMHD simulations, as the trajectories of infalling matter through the event horizon are of particular interest for simulating accretion, thus many codes choose to adopt Kerr-Schild coordinates which are non-singular at r_{EH}. [120, 121, 122] The Kerr-Schild formulation of the Kerr metric requires a coordinate transformation of the Boyer-Lindquist coordinates t and ϕ of the form

$$d\tilde{t} = \left(dt + \frac{2Mr}{\Delta}dr\right) \text{ and } d\tilde{\phi} = \left(d\phi + \frac{a}{\Delta}dr\right), \tag{4.1}$$

rendering the metric as

$$\begin{aligned} dS^2 = &-\left(1 - \frac{2Mr}{\rho^2}\right)d\tilde{t}^2 - \left(\frac{4Marsin^2\theta}{\rho^2}\right)d\tilde{t}d\tilde{\phi} + \left(\frac{4Mr}{\rho^2}\right)d\tilde{t}dr \\ &-2asin^2\theta\left(1 + \frac{2Mr}{\rho^2}\right)drd\tilde{\phi} + \left(\frac{\Sigma}{\rho^2}sin^2\theta\right)d\tilde{\phi}^2 + \left(1 + \frac{2Mr}{\rho^2}\right)dr^2 + \rho^2 d\theta^2 \end{aligned} \tag{4.2}$$

where

$$\rho^2 = r^2 + a^2 cos^2\theta \ , \tag{4.3a}$$

$$\Delta = r^2 - 2Mr + a^2 \ ,\text{and} \tag{4.3b}$$

$$\Sigma = (r^2 + a^2)^2 - a^2 \Delta sin^2\theta. \tag{4.3c}$$

While these pseudo-spherical Kerr-Schild coordinates $x^\mu = \{\tilde{t}, r, \theta, \tilde{\phi}\}$ remove the coordinate singularity that existed in Equation 2.3, they also lack much of the convenience of the Boyer-Lindquist formulation. The metric no longer reduces to the Schwarzchild metric at $a = 0$, and now has mixed terms in g_{tr}, $g_{t\phi}$, and $g_{r\phi}$. These additional components in the metric will prevent the parameterization of the geodesic equation utilized in integration in the Boyer-Lindquist case, as will now be shown.

4.2.1 Conserved Quantities and the Innermost Stable Circular Orbit

As described in Section 2.2.1, the existence of Killing vectors on a Reimannian manifold represent an isometry of the manifold itself. Their existence in the Kerr metric, and the conserved quantities associated with them, are a property of the spacetime and are independent of any chosen coordinates [6]. For the Kerr spacetime, the Killing vectors are $\xi_1 = (1, 0, 0, 0)$ and $\xi_2 = (0, 0, 0, 1)$. Just as in the Boyer-Lindquist case, the conserved quantities associated with these vectors can be found as

$$g_{\mu\nu}\xi_1^\mu k^\nu = -E = g_{tt}k^t + g_{tr}k^r + g_{t\phi}k^\phi \tag{4.4}$$

$$g_{\mu\nu}\xi_2^\mu k^\nu = L = g_{t\phi}k^t + g_{r\phi}k^r + g_{\phi\phi}k^\phi \tag{4.5}$$

There is no parameterization of the geodesic equation in terms of these conserved quantities in Kerr-Schild coordinates as there is in Boyer-Lindquist, as the two equations are over-determined. But, the quantities that they represent are still conserved, and are used to check the error on the calculation as the system is integrated.

It is also possible to derive these same conserved quantities via the Euler-Lagrange equation, which the reader knows well from mechanics, finding conserved quantities as they apply to any orbiting body in the Kerr spacetime. Taking the Lagrangian as $L = \frac{1}{2} g_{\mu\nu} u^\mu u^\nu$, where $u^\mu = \dot{x}^\mu$, the Euler-Lagrange equation is

$$\frac{d}{d\tau}\frac{\partial L}{\partial \dot{x}^\mu} - \frac{\partial L}{\partial x^\mu} = 0 \rightarrow \frac{d}{d\tau}\frac{\partial L}{\partial \dot{x}^\mu} = \frac{\partial L}{\partial x^\mu}. \tag{4.6}$$

Here, τ is the proper time. Conjugate momenta occur when $\frac{\partial L}{\partial x^\mu} = 0$, which for this stationary, axially symmetric metric is satisfied for both x^t and x^ϕ. Then,

$$\frac{\partial L}{\partial t} = 0 \rightarrow \frac{\partial L}{\partial \dot{x}^t} = constant = \frac{1}{2} g_{t\nu}\dot{x}^\nu = \frac{1}{2}(g_{tt}\dot{x}^t + g_{tr}\dot{x}^r + g_{t\phi}\dot{x}^\phi) \tag{4.7}$$

$$\frac{\partial L}{\partial \phi} = 0 \rightarrow \frac{\partial L}{\partial \dot{x}^\phi} = constant = \frac{1}{2} g_{\phi\nu}\dot{x}^\nu = \frac{1}{2}(g_{t\phi}\dot{x}^t + g_{\phi r}\dot{x}^r + g_{\phi\phi}\dot{x}^\phi) \tag{4.8}$$

For a photon, where $\dot{x}^\mu = k^\mu$, the conjugate momenta recovered are exactly the conserved quantities found via the Killing vectors (as they should be). The Langrangian formulation is shown here as careful consideration of Equation 4.6 allows the definition of an important quantity in the physics of black hole accretion: the innermost stable circular orbit, r_{ISCO}.

Following Bardeen (1974)[123] and Johannsen and Psaltis (2011)[124], the innermost stable circular orbit is that which satisfies $\frac{dE}{dr} = 0$. A stable circular orbit trivially satisfies

$dr/d\tau = \dot{x}^r = 0$, which renders the factor $\frac{\partial L}{\partial \dot{x}^r} = 0$. Then,

$$\frac{\partial L}{\partial x^r} = \frac{1}{2}(\partial_r g_{tt}(u^t)^2 + \partial_r g_{\phi\phi}(u^\phi)^2 + \partial_r g_{\theta\theta}(u^\theta)^2 + \partial_r g_{t\phi} u^t u^\phi) = constant = E. \tag{4.9}$$

Adding the constraint that the particle's orbit is confined to the equatorial plane, $u^\theta = 0$. Solving for u^ϕ/u^t gives,

$$\frac{u^\phi}{u^t} = \frac{\partial_r g_{t\phi} - \sqrt{(\partial_r g_{t\phi})^2 - \partial_r g_{tt}\partial_r g_{\phi\phi}}}{\partial_r g_{\phi\phi}} = \Omega, \tag{4.10}$$

where Ω is the orbital frequency of the particle. Next, as u^μ is a timelike vector, u^t can be written as

$$u^t = \frac{1}{\sqrt{-g_{tt} - 2\Omega g_{t\phi} - \Omega^2 g_{\phi\phi}}}. \tag{4.11}$$

u^ϕ is then

$$u^\phi = \Omega u^t, \tag{4.12}$$

leaving Equation 4.9 as

$$E = -\frac{(g_{tt} + \Omega g_{t\phi})}{\sqrt{-g_{tt} - 2\Omega g_{t\phi} - \Omega^2 g_{\phi\phi}}}. \tag{4.13}$$

Equation 4.13 has terms determined solely by the metric and its derivatives. From here, finding r_{ISCO} is a matter of solving $dE/dr = 0$ for the appropriate spin and mass as is shown in Figure 4.1. Completing this process in Boyer-Lindquist coordinates yields the same result.

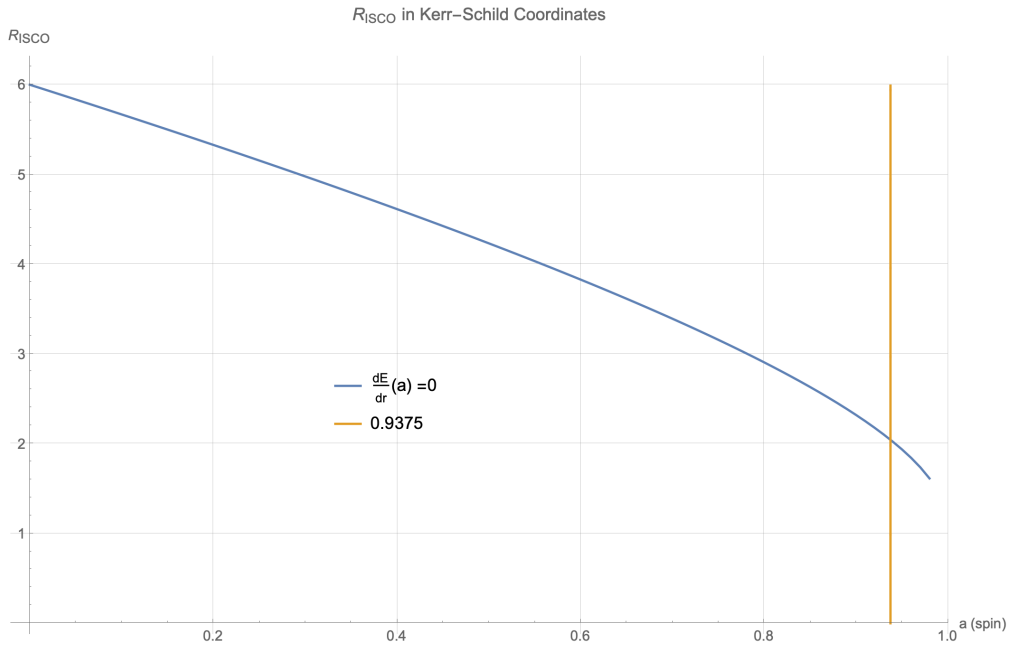

Fig. 4.1: Numerical solution of solving the $\frac{dE}{dr} = 0$ (E given in Equation 4.13) to solve for the innermost stable circular orbit. The vertical line is the spin of the black hole simulated by the H-AMR data.

4.3 The GRMHD Data from H-AMR

The data from the *H-AMR* GRMHD simulation is binned in 3000 $\sim 50\frac{r_g}{c}$ wide frames. In each frame, the disk is parameterized into 512 azimuthal bins and 356 logarithmic radial bins on the interval $r_{EH} \leq r \leq 140\ r_g$. The θ value corresponding to each (r, ϕ) grid point is given as a midplane approximation, wherein a value (θ_{mp}) is calculated as the being the midpoint of the volume element of the disk based on the density in a 1 r_g^2 bin around the grid point. For each frame, the input data contains the accretion rate in code units, $\dot{M}_{au}$, calculated by integrating the net flux of matter density into the event horizon over all solid angle. The surface flux, $F = \frac{dU}{dtdA}$, the energy dissipation per unit surface area in the plasma frame, is determined by an artificial cooling function designed to keep the disk thin over the runtime of the simulation. Table 4.1 gives a summary of the H-AMR data that is read into xTrack.

Physical Quantity	*Variable*	*Units*	*Binning*
time stamp of frame	t_{frame}	$\frac{r_g}{c}$	for frame
accretion rate	$\dot{M}_{au}$	arbitrary units	for frame
integrated density	ρ_{au}	arbitrary units	(r, ϕ)
internal energy	U_{au}	arbitrary units	(r, ϕ)
Flux	$F_{au} = \frac{dU}{dtdA}$	arbitrary units	(r, ϕ)
4-velocity	u^{μ}_{KS}	$\gamma, \dot{r}, \dot{\theta}, \dot{\phi}$	(r, ϕ)
normal 3-vector	$\vec{n}$	$\hat{r}, \hat{\theta}, \hat{\phi}$	(r, ϕ)
tilt angle	θ_{tilt}	degrees	ϕ
precession angle	ϕ_{prec}	degrees	r
radial accretion rate	$\dot{M}(r, \phi)_{au}$	arbitrary units	(r, ϕ)

Tab. 4.1: Parameterization of the H-AMR Data

The conversion of variables like $\dot{M}$ from arbitrary code units into physical units is necessary for the analysis. In order to simplify these calculations, some useful scale quantities are

defined here. Letting the mass of the black hole, $M_{BH} = 10M_{\odot} = 2 \times 10^{34} g$, the fundamental length scale can be defined as

$$\ell = \frac{GM_{BH}}{c^2} \; [cm] \tag{4.14}$$

where $G = 6.67 \times 10^{-8} cm^3 g^{-1} s^{-1}$ is the gravitational constant and $c = 3 \times 10^{10} cm/s$ is the speed of light. This can be thought of as the mass of the black hole in *geometrized* units. A fundamental time scale can then be defined as

$$t = \frac{\ell}{c} \; [s]. \tag{4.15}$$

In order to calculate the accretion rate, emissivity, and temperature in physical units, the efficiency of the flow η must be calculated. Following Novikov & Thorne's [51] prescription,

$$\eta = 1 - E_{ISCO} = 0.179 \tag{4.16}$$

where E_{ISCO} is given by Equation 4.13. Taking this efficiency and the formal definition of luminosity, $L = \eta \dot{M} c^2$ [115], and choosing the desired accretion rate, which here is $\dot{M} = 0.1 \dot{M}_{Edd}$ corresponding with a scale height of $H = 0.03$, with $\dot{M}_{Edd}$ being the Eddington rate, a scale density can also be defined as

$$\rho_{sc} = \frac{\dot{M} t}{\dot{M}_{au} \ell^3} \; [\mathrm{g/cm^3}]. \tag{4.17}$$

With these definitions, the arbitrary units utilized in the code can be converted into real, physical units. The flux emitted per unit surface area per unit time in the plasma frame, for example, is calculated as

$$\mathcal{F} = \frac{|F_{au} \gamma| \rho_{sc} c^2 \ell}{t} \; [\mathrm{ergs/cm^2/s}]. \tag{4.18}$$

The optical depth, which is assumed to be due to electron scattering, is found with

$$\tau = \kappa_R \Sigma = \kappa_R \rho_{au} \ell \text{ [unitless]}, \tag{4.19}$$

where $\kappa_R \simeq \frac{\sigma_T}{m_p} \simeq 0.4 cm^2 g^{-1}$ for electron scattering (see Chapter 5.6 in [115]).

4.4 Thermal Emission

Unlike the thick torus disk discussed above in 2.4, there is no azimuthal symmetry (or indeed, any symmetry) in this disk - photons cannot be emitted solely into the upper hemisphere without loss of accuracy, and photons arriving at $\theta_{obs} \geq \frac{\pi}{2}$ cannot be folded to the upper hemisphere of the observer plane. Instead, thermal photons are emitted isotropically across all solid angle from each (r, ϕ) grid point for $r_{EH} \leq r \leq 100\ r_g$ and for all ϕ, such that the initial position of each photon is some $x^\mu_\gamma = (t_{frame}, r_i, \theta_{mp}, \phi_i)$.

Photon wave-vectors $\mathbf{k}^\mu$ are initialized as null 4-vectors with their components being drawn with a random probability per solid angle in the plasma frame such that $|\mathbf{k}^\mu| = 0$. Each photon energy k^t is given a value of unity, allowing a simple calculation of the Doppler boost by evaluating k^t_{obs} (this boost, commonly called a g-factor, is necessary for applying proper energies in the analysis, as will be described below). The polarization vector $\mathbf{f}^\mu$ is similarly drawn from a random distribution and initialized such that $f^t = 0$ and $|\mathbf{f}^\mu| = constant$. A final constraint on the initialization of a photon wave packet is the orthogonality of the wave and polarization vectors, with each initialized four vector satisfying $\mathbf{k}_\mu \mathbf{f}^\nu = 0$. The initial polarization is calculated from Table XXIV of Chandrasekhar [24] and the photons are statistically weighted with the product of his limb brightening function and F_{au}.

After initialization in the plasma frame, photons are transformed into the global Kerr-

Schild frame and propogated forward by integrating the geodesic equation

$$\frac{d^2x^\mu}{d\lambda'^2} = -\Gamma^\mu_{\sigma\nu}\frac{dx^\sigma}{d\lambda'}\frac{dx^\nu}{d\lambda'} \tag{4.20}$$

and parallel transporting the polarization vector $\mathbf{f}^\mu$ according to

$$\frac{df^\mu}{d\lambda'} = -\Gamma^\mu_{\sigma\nu}f^\sigma\frac{dx^\nu}{d\lambda'}. \tag{4.21}$$

Here, $\Gamma^\mu_{\sigma\nu} = \frac{1}{2}g^{\rho\lambda}(\partial_\mu g_{\nu\lambda} + \partial_\nu g_{\mu\lambda} - \partial_\lambda g_{\mu\nu})$ are the Christoffel symbols and are determined entirely by the metric as defined in its coordinate basis. The integration algorithm follows the Cash-Karp methodology [109], a fifth order Runge-Kutta algorithm that utilizes adaptive step sizes. The adaptive step sizing is necessary for raytracing in the high gravity regime, as the curved space near the compact object requires very small step sizes for accuracy. The maximum step size of the integration is smaller than in the Boyer-Lindquist case, as the Kerr-Schild spacetime does not allow the parameterization of the geodesic equation described in Section 2.2.1. Thus, all four components of the wave vector must be integrated, which consequently increases the error on the calculation. In an effort to reduce this error further, and to prevent possible photon-disk interactions from being erroneously missed, an additional step size adaptation is added to the integration which truncates the the step size as the photon travels from x^μ_i to $x^\mu_i + \Delta x^\mu_i$ to the grid in $(r_i, \phi_i), (r_j, \phi_j)$ which bounds x^μ_i such that $r_i \leq x^r_i \leq r_j$ and $\phi_i \leq x^\phi_i \leq \phi_j$. This adaptation limits the maximal step size of a single integration to the edge of the grid that the photon is in currently, forcing smaller step sizes than would ordinarily be tolerable with Cash-Karp and ensuring that no photon-disk interactions can be missed due to multiple grid cells being traversed in a single step.

Photons are allowed to scatter off of the disk an indefinite number of times where $\tau >$

1 as calculated in 4.19, while passing through the gaps that open up during the tearing events. This includes scattering in the plunging region where $r_{EH} \leq r \leq r_{ISCO}$, provided the aforementioned requirement on the optical depth is met. The disk evolves on timescales much faster than the light travel time from the inner-edge of the disk to its outer-edge, an effect known as 'slow light.' To account for this, multiple frames of the disk are read in at a time. As each photon is initialized with its $x^{t_0} = t_{frame}$, the disk geometry used to determine scattering is simply updated to a time configuration that is closest to the photon's age when the scattering check occurs. The intersection of the geodesic with the disk is determined geometrically, and when a valid intersection is detected the geodesic is truncated such that it ends exactly on the midplane of the disk (this algorithm is described in detail in Section 4.4.1). When this occurs, the same prescription is followed as in the Boyer-Lindquist case of the torus disk. The photon's wave and polarization vectors are transformed into the plasma frame using the tetrad described in 4.4.2, where the incoming polarization angle and degree are calcualted with the Stokes parameters encoded in $\mathbf{f}^{\nu}$. The outgoing Stokes parameters are then calculated using Equation 164 and Table XXV of Chandrasekhar [24]. The stokes parameters are then used to calculate the outgoing polarization degree and angle and the statistical weight of the interaction based on the direction of scattering. The trajectory of the outgoing photon is drawn from a random probability per solid half-angle, with the sign k^{θ}_{PF} determined algorithmically to ensure that photons impinging from above are reflected above, and vise versa. Finally, $\mathbf{k}^{\mu}$ and $\mathbf{f}^{\nu}$ are transformed back into the global Kerr-Schild frame, and the integration of the geodesic equation and parallel transport of the polarization vector resume.

Photon geodesics are integrated until they either cross into the event horizon or reach an observer in asymptotically flat space. Contrary to the torus disk in Boyer-Lindquist coordinates, where geodesics are determined to cross into the horizon when $x^{r}_{\gamma} \leq 1.02\ r_{EH}$,

in the Kerr-Schild case photon geodesics are only terminated when $x^r_\gamma < r_{EH}$. The observer is located at a distance of $10,000 r_g$, and photons reaching this distance are transformed into a coordinate stationary frame such that $\mathbf{e}_\mu \cdot \mathbf{e}_\nu = \eta_{\mu\nu}$, where $\eta_{\mu\nu}$ is the metric of Minkowski.

At emission, Equation 4.18 is utilizied to calculate the temperature for the grid point of emission with

$$T_{eff} = f_h \left(\frac{\mathcal{F}}{\sigma_{SB}} \right)^{\frac{1}{4}}. \tag{4.22}$$

where σ_{SB} is the Stef-Boltzmann constant and $f_h = 1.8$ is the spectral hardening factor [110]. To determine the statistical weight of each photon that reaches the observer, $\mathcal{F}$ must be calculated in the global frame. The number of photons emitted in the plasma frame per unit proper time and area is equal to the number of photons emitted in the global frame per unit global time and area. Kulkarni [125] and Krawczynski [93] note that as the proper four volume is an invariant and the proper distance along θ is an invariant for boosts along the $\mathbf{e}_\phi$ direction, $\sqrt{-g_{tr\phi}}$ is also an invariant. This fact holds true even in the presence of θ components of momentum, as can be verified numerically by transforming the vector $Y^\mu = (0, 0, d\theta, 0)$ into the plasma frame. Thus, the number of photons emitted in the global frame per unit global time and area is given by

$$\frac{dN}{dt\ dr\ d\phi} = \sqrt{-g_{tr\phi}} \frac{\mathcal{F}}{\langle \hat{E} \rangle} \omega_i. \tag{4.23}$$

The factor $\sqrt{-g_{tr\phi}} = \sin\theta \sqrt{r^2 - a^2 \cos\theta^2}$ is the determinant of the $t - r - \phi$ components of the metric. The statistical weight at the observer of each photon is then given by

$$\omega_{st} = \sqrt{-g_{tr\phi}} \frac{\mathcal{F}}{\langle \hat{E} \rangle} \omega_i \tag{4.24}$$

where ω_i contains the weights of emission and all scattering processes and $\langle \hat{E} \rangle = 2.7 f_h k_b T_{eff}$

is the average energy of the photon in the plasma frame. For a spectral bin bounded below by $E1$ and above by $E2$, the photon then contributes a statistical weight of

$$\omega = \omega_{st} \frac{\int_{E1}^{E2} \frac{E^2}{e^{E/\epsilon_0}-1} dE}{\int_0^{\infty} \frac{E^2}{e^{E/\epsilon_0}-1} dE} \tag{4.25}$$

The factor $\epsilon_0 = T_{eff} * g$ encodes the effect of boosting on the distribution.

4.4.1 Scattering Algorithm

Disk crossings are determined geometrically by utilizing the the photons current position, x_i^μ, next position after integration, $x_j^\mu = x_i^\mu + \Delta x^\mu$, and the grid (r_i, ϕ_i) and (r_{i+1}, ϕ_{i+1}). The integration steps are limited such that the grid bounds both the current position of the photon and the next integration step of the photon, with $r_i \leq x_i^r, x_j^r \leq r_{i+1}$ and $\phi_i \leq x_i^\phi, x_j^\phi \leq \phi_{i+1}$. The indexing of this grid defines two sides of a quadrilateral surface with three vertices given (for example) by $P_1 = (r_i, \phi_i)$, $P_2 = (r_{i+1}, \phi_i)$ and $P_3 = (r_{i+1}, \phi_{i+1})$. With these three vertices, it is straightforward to define an equation of surface, $\mathcal{S}$. First, after converting to cartesian coordinates, let the normal $\vec{n} = (P_2 - P_1) \times (P_3 - P_2)$ and let $P_0 \in \mathcal{S}$. The equation of the surface is then

$$(P - P_0) \cdot \vec{n} = 0 \tag{4.26}$$

Any point P that satisfies this equation must be on the plane defined by the surface (but is not necessarily on the surface bounded by the grid). Next, letting l_i and l_j be the cartesian coordinates of the spatial components of x_i^μ and x_j^μ, respectively, the equation of the ray is then

$$P = l_i + \vec{l}d \tag{4.27}$$

where $\vec{l} = l_j - l_i$ and d is some constant. If $\vec{l} \cdot \vec{n} \neq 0$ then there is the possibility of a crossing. Combining Equations 4.26 and 4.27,

$$d = \frac{(P_0 - l_i) \cdot \vec{n}}{\vec{l} \cdot \vec{n}} \tag{4.28}$$

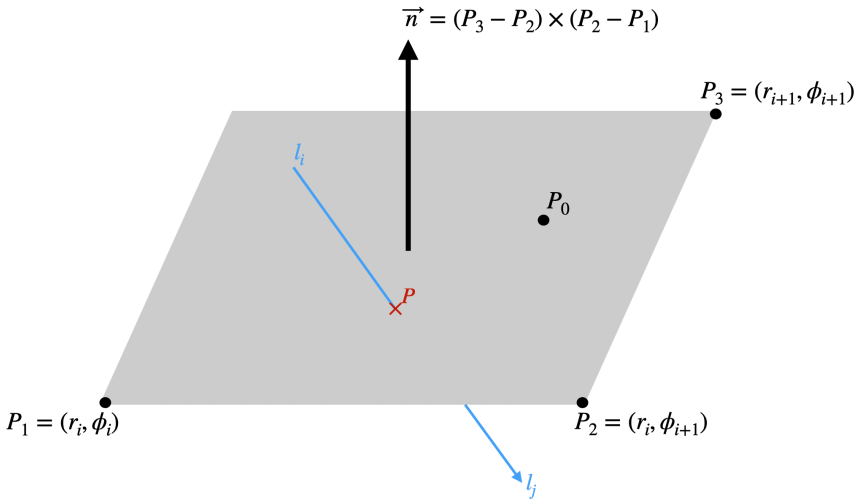

Fig. 4.2: Schematic drawing of the points and vectors required for detecting a photon-disk interaction.

Plugging d back into Equation 4.27 allows a solution for P. If P lies between the end points of $\vec{l}$ then it is within the grid bounded by (r_i, ϕ_i) and (r_{i+1}, ϕ_{i+1}), thus $P \in \mathcal{S}$ and a disk crossing has occurred. The integration step is then truncated such that the geodesic ends on point P.

4.4.2 Tetrad of the Misaligned Disk

In order to transform into the plasma frame and out of the plasma frame into the global Kerr-Schild frame, a tetrad must be constructed for the point of emission (or interaction, in the case of scattering). This tetrad, composed of one time-like and three space-like vectors, must span the local frame rest frame of the disk element, rendering its effective metric to be Minkowskian, while conserving the Lorentzian properties of the space. As described in Appendix A, the Graham-Schmidt orthogonalization algorithm is used to construct the tetrad. Unlike the result discussed in Section 2.3 or in [93, 99], the tetrad describing this misaligned and warped disk does not have an elegant, closed form solution. This is in part due to the complexity of the Kerr metric in Kerr-Schild coordinates, and in part due to the the complexity of the disk itself.

Unlike Boyer-Lindquist coordinates, which render the spacetime into 6 metric elements (the diagonals g_{tt}, g_{rr}, $g_{\theta\theta}$ and $g_{\phi\phi}$ the mixed terms $g_{t\phi}$ and $g_{\phi t}$), the Kerr-Schild prescription renders the spacetime into 10 metric elements, with only the mixed terms in θ being zero. And unlike the classical thin disk and toroidal disk described in Chapter 2, which have only a ϕ component to their orbital velocity, this misaligned, warped disk has velocity components in all three spatial dimensions. Finally, the normal vector, which is the θ tangent vector, may also contain three spatial components. To overcome these complexities, the tetrad is computed numerically by computing the orthogonalization algorithm at every necessary

point.

The time-like input vector is chosen to be the four-velocity of the plasma, $\mathbf{u}^{\mu}_{KS} = (\gamma, u^r, u^\theta, u^\phi)$. The radial and azimuthal tangent vectors ($\frac{dS}{dx^\mu}$) are taken from the surface itself. For emission, these are found by indexing, such that a photon emitted from $x^\mu = (x^t, x^r_i, x^\theta, x^\phi_j)$, where (i, j) are the indexes of the radial and azimuth grid for the point of emission, will have radial and azimuthal tangent components of $\frac{dS}{dr} = x^\mu_{i+1} - x^\mu_i$ and $\frac{dS}{d\phi} = x^\mu_{j+1} - x^\mu_j$, respectively. Taking the Kerr-Schild tangent vectors as $\mathbf{e}_\mu = \partial_\mu$, and the tangents of the surface as $\frac{dS}{dx^\mu}$, the values of the (unnormalized) seed vectors for the orthogonalization are taken as $\mathbf{v}^\mu \propto \frac{dS}{dx^\mu}\mathbf{e}_\mu$, with $\mathbf{v}^\phi$ having an extra factor $\mathbf{e}_t$ to ensure the orthogonality with u^μ and allow the tetrad of a Keplerian thin disk to be recovered.

The θ tangent is then taken as the the normal to the surface as defined by *H-AMR* and read in at runtime. From here, denoting the plasma frame with the tilde, the basis is computed as follows:

$$\mathbf{e}_{\tilde{t}} = u^\mu_{KS} \tag{4.29}$$

$$\mathbf{e}_{\tilde{r}} = \mathbf{v}^r + (\mathbf{e}_{\tilde{t}} \cdot \mathbf{v}^r)\mathbf{e}_{\tilde{t}} \tag{4.30}$$

$$\mathbf{e}_{\tilde{\phi}} = \mathbf{v}^\phi + (\mathbf{e}_{\tilde{t}} \cdot \mathbf{v}^\phi)\mathbf{e}_{\tilde{t}} - (\mathbf{e}_{\tilde{r}} \cdot \mathbf{v}^\phi)\mathbf{e}_{\tilde{r}} \tag{4.31}$$

$$\mathbf{e}_{\tilde{\theta}} = \mathbf{v}^\theta + (\mathbf{e}_{\tilde{t}} \cdot \mathbf{v}^\theta)\mathbf{e}_{\tilde{t}} - (\mathbf{e}_{\tilde{r}} \cdot \mathbf{v}^\theta)\mathbf{e}_{\tilde{r}} - (\mathbf{e}_{\tilde{\phi}} \cdot \mathbf{v}^\theta)\mathbf{e}_{\tilde{\phi}} \tag{4.32}$$

Note that, as described in Appendix A, each $\mathbf{e}_{\tilde{\mu}}$ is normalized after it is computed and before the calculation proceeds to the next step. These vectors are by construction mutually

orthogonal, and the three spatial vectors of the tetrad are properly space-like four-vectors. The vector $\mathbf{e}_{\tilde{t}}$ is time-like by definition, and this is accounted for in the change of sign accompanying the subtraction of these projections across the spatial components of the tetrad. These vectors are the column vectors of the transformation matrix $\mathbf{e}^{\nu}_{\widetilde{\mu}}$, satisfying $\mathbf{e}_{\widetilde{\mu}} = e^{\nu}_{\widetilde{\mu}} \cdot \mathbf{e}_{\nu}$. Letting a bar denote the inverse, transformations into and out of the plasma frame occur with

$$\mathbf{k}^{\widetilde{\mu}} = \bar{e}^{\widetilde{\mu}}_{\nu} \cdot \mathbf{k}^{\nu} \tag{4.33}$$

and

$$\mathbf{k}^{\nu} = e^{\nu}_{\widetilde{\mu}} \cdot \mathbf{k}^{\widetilde{\mu}}. \tag{4.34}$$

The tetrad required for scattering events follows the same basic algorithm, but the input vectors change. The vector $\mathbf{e}_{\tilde{t}}$ is set equal to the four velocity of the plasma as linearly interpolated between the two nearest neighboring grid points and the point of scattering. The normal at the point of scattering (to be used as $\mathbf{v}^{\theta}$) taken as the norm defined for the grid surface in the scattering alogrithm. The radial and azimuthal tangents are computed by finding $\frac{dS}{dr}$ or $\frac{dS}{d\phi}$ between the point of scattering and the nearest grid point in increasing r or ϕ, respectively. Transformations into the frame of a coordinate stationary observer also utilize this algorithm, taking the input for $\mathbf{e}_{\tilde{t}}$ as the momentum of a stationary observer and letting $\mathbf{e}_{\mu}$ be the tangents of Minkowski space, we have:

$$\mathbf{e}_{\tilde{t}} = \mathbf{p}_{t} \tag{4.35}$$

$$\mathbf{e}_{\tilde{\phi}} = \mathbf{e}_{\phi} + (\mathbf{e}_{\tilde{t}} \cdot \mathbf{e}_{\phi})\mathbf{e}_{\tilde{t}} \tag{4.36}$$

$$\mathbf{e}_{\tilde{\theta}} = \mathbf{e}_{\theta} + (\mathbf{e}_{\tilde{t}} \cdot \mathbf{e}_{\theta})\mathbf{e}_{\tilde{t}} - (\mathbf{e}_{\tilde{\phi}} \cdot \mathbf{e}_{\theta})\mathbf{e}_{\tilde{\phi}} \tag{4.37}$$

$$\mathbf{e}_{\tilde{r}} = \mathbf{e}_r + (\mathbf{e}_{\tilde{t}} \cdot \mathbf{e}_r)\mathbf{e}_{\tilde{t}} - (\mathbf{e}_{\tilde{\phi}} \cdot \mathbf{e}_r)\mathbf{e}_{\tilde{\phi}} - (\mathbf{e}_{\tilde{\theta}} \cdot \mathbf{e}_r)\mathbf{e}_{\tilde{\theta}} \tag{4.38}$$

Note that $\mathbf{e}_{\tilde{r}}$ is orthogonalized last in the alogrithm. This is due to the to the $g_{r\phi}$ and $g_{\phi r}$ components of the metric, which have a form $drd\phi = -2a\sin^2\theta(1 - \frac{2r}{\rho})$. These components do not go to zero at large r. Orthogonalizing in the order t, ϕ, θ, r yields basis vectors which produce a Minkowskian metric, transform $\mathbf{p}_t$ into its own rest frame with the proper sign, and minimize the error on $|\mathbf{k}^\mu|$ and $|\mathbf{f}^\nu|$ after the transformation.

4.5 Lamppost Emission

The distribution of momentum across the disk as it warps, tears, and precesses, is highly dynamic and deviates significantly from a Keplerian prescription. In particular, there are large variations in the θ component of the momentum, the influence of which on emission lines, like the Fe-Kα line, are up to this point not well understood. In an effort to quantify this, a 'lamppost' corona geometry is initialized in the code to emit power-law photons that will reflect off of the evolving disk structure.

In other *H-AMR* simulations of misaligned and precessing disks, jets were produced that precessed with the disk. The alignment of these jets correlated to the alignment of the disk on comparable scales. On scales smaller than the tearing radius, the jet aligns with the angular momentum of inner disk, and at scales larger than the tearing radius, the jet aligns with angular momentum of the outer disk.

In order to fully explore the effects of this precessing disk and its accompanying jets on the Fe-kα line, two lamppost models have been built into the code. The first is a classic lamppost aligned with the black hole spin axis, though slightly offset to avoid the coordinate singularity that occurs at $\theta = 0, \pi$. The second has been designed to mimic the precessing

jet observed in simulations and is aligned with the inner disk angular momentum vector. Letting the lamppost $LP1$ be aligned with the inner disk and r_1 be the outer edge of the inner disk, the lamppost is located at

$$x^{\mu}_{LP1} = (t_{frame}, r_1, \theta_{tilt}, \phi_{prec}). \tag{4.39}$$

where θ_{tilt} and ϕ_{prec} are the tilt and precession angles of the disk at radius r_1.

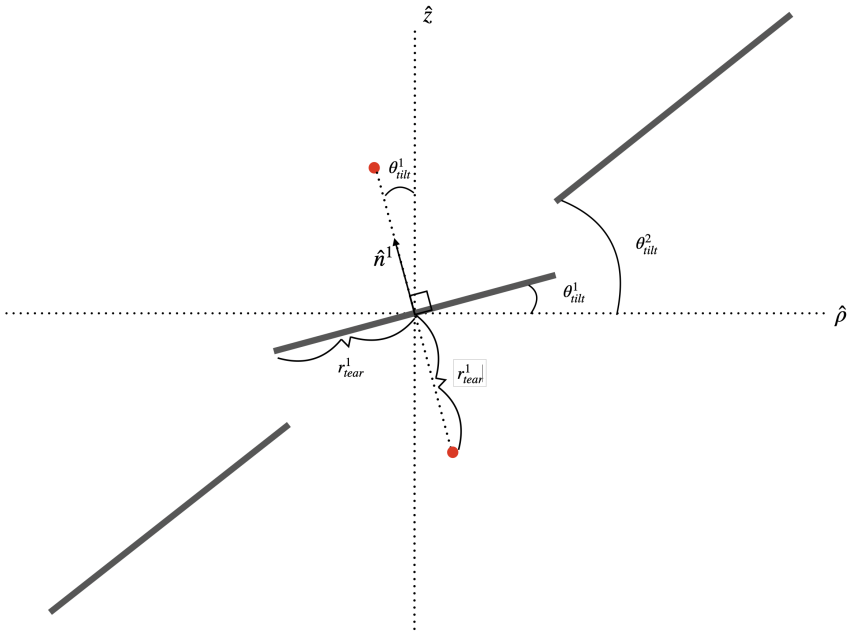

Fig. 4.3: Schematic of lamppost model LP1. The lamppost is offset from the black hole spin axis by the tilt angle at the tearing radius and its height above the disk is equal to that radius.

Due to the lack of symmetry in the disk there are two lampposts for each configuration, one above and one below the disk. For the axially aligned configuration, the second lamppost is located at $\theta = \pi - \delta$, and in the offset configuration the second lamppost is located at $\theta_{tilt} + \frac{\pi}{2}$ and $\phi_{prec} + \pi$. For simplicity, the lampposts are initialized in the frame of a zero angular momentum observers (ZAMO), with their positions advancing at rest frame by frame

as the disk precesses. ZAMO frames, or locally non-rotating inertial frames as they were originally coined by Bardeen et al in 1974 [126], are frames which are stationary with respect to an observer located at infinity (i.e., Equation 2.5 equals zero). Locally, however, these frames co-rotate with the ergotic precession of the spacetime induced by the black hole's spin [6]. The frequency of this frame dragging in Boyer-Lindquist coordinates is given by

$$\Omega \equiv \frac{d\phi}{dt} = \frac{d\phi/d\tau}{dt/d\tau} = \frac{u^{\phi}}{u^{t}} = \frac{-g_{t\phi}}{g_{\phi\phi}} \tag{4.40}$$

Substituting Equations 4.1 into 4.40 to convert to Kerr-Schild coordinates,

$$\frac{d\phi}{d\tau} = \frac{d\tilde{\phi}}{d\tau} - \frac{2Mr}{\Delta}\frac{dr}{d\tau} \tag{4.41}$$

$$\frac{dt}{d\tau} = \frac{d\tilde{t}}{d\tau} - \frac{a}{\Delta}\frac{dr}{d\tau} \tag{4.42}$$

The factors $\frac{dr}{d\tau}$ are trivially zero by the requirement of stationarity in the frame. Thus, $\Omega_{BL} = \Omega_{KS} = \frac{-g_{t\phi}}{g_{\phi\phi}}$. The tetrad of our ZAMO frame is then constructed following the prescription in Appendix A, with $\mathbf{e}_{\tilde{t}} = (1, 0, 0, \Omega_{KS})$.

The lamppost emits power law photons corresponding to a photon index of $\Gamma = 1.7$ proportional to $dN/dE \propto E^{-(\Gamma+1)}$, producing emission in the range $1 - 100keV$. These photons are emitted isotropically over solid angle, irradiating the disk from above and below. The fluorescence of Fe-Kα photons follows the prescription of George and Fabian [127], where a minimum ionizing energy of 7.1keV is required to liberate the electron from the k-shell of the Fe atom. When a photon interacts with the disk, it is transformed into the plasma frame and if $u^{t}_{PF} > 7.1$keV an iron photon is emitted following the same procedure used for thermal emission, with the caveat that its plasma frame energy is 6.4keV. If u^{t}_{PF} does not meet this threshold, the photon is reflected according to the procedure outlined in Section 4.4. Iron

photons are tagged on emission so that they can be separated in analysis.

4.6 Thin Disk in Kerr-Schild Coordinates

4.6.1 Thermal Emission

In order to test the validity of a code, a psuedo thin disk is constructed by projecting a frame of the *H-AMR* data into the equatorial plane and adding small deviations in θ_{disk} such that $\theta_{disk} = \frac{\pi}{2} + 0.1 * \delta\theta$ where $\delta\theta$ is a random number in the range $(-1, 1)$ corresponding to a maximum deviation of 5° from the equatorial plane. The velocities are constructed to be Keplerian, with $\Omega_K = (a + r^{3/2})^{-1}$ and the tetrad is constructed following the procedure in Appendix A with $\mathbf{e}_{\tilde{t}} = (1, 0, 0, \Omega_K)$. Photons are emitted isotropically across solid angle from each (r, ϕ) grid point in the disk. Photons impinging on the disk from above are reflected upwards and photons impinging from below are reflected downwards. Finally, a radial brightness profile corresponding to an accretion rate of $0.1\ \dot{M}_{Edd}$ and a spin of $a = 0.9$ is applied following the Page and Thorne prescription (appropriately derived in the Kerr-Schild formulation of the Kerr Metric). The same brightness profile (again, derived in appropriate coordinates) is then applied to the classic thin disk in Boyer-Lindquist coordinates. Emission from the Boyer-Lindquist disk occurs in radial bins at a single azimuth, while emission from the Kerr-Schild disk occurs in radial and azimuth bins. Observations are integrated over all azimuths for the Boyer-Lindquist case photons arriving below $\theta = \pi/2$ are folded up as described in Chapter 2. In the Kerr-Child case, no photons are folded from the lower hemisphere to the upper hemisphere, as in the GRMHD data set there is no symmetry in the disk. Kerr-Schild photons are collected in single azimuthal bins with $\Phi \pm 4^\circ$. For both, the inclination observation window is $i \pm 4^\circ$.

The comparison begins with images of the direct and reflected emission for each case, where the bars overlaid are proportional to the polarization degree and angle. Figure 4.4 shows the direct emission for the Boyer-Lindquist disk on the left, and the Kerr-Schild disk on the right. The maps show three inclinations, $i = 25°$ (top row), $45°$ (middle row), and $65°$ (bottom row). The color in these maps is logarithmic intensity and is scaled to arbitrary units. The differences in apparent intensity between the two cases are due mainly to the difference in binning between the two cases. The Boyer-Lindquist (on the left) disk is segmented into 10,000 logarithmic spaced radial bins, whereas the Kerr-Schild case (on the right) is segmented into only a few hundred. Overplotted on the intensity is the polarization due to direct emission, with the length and direction of the bars encoding the polarization degree and angle. The maps are approximately the same.

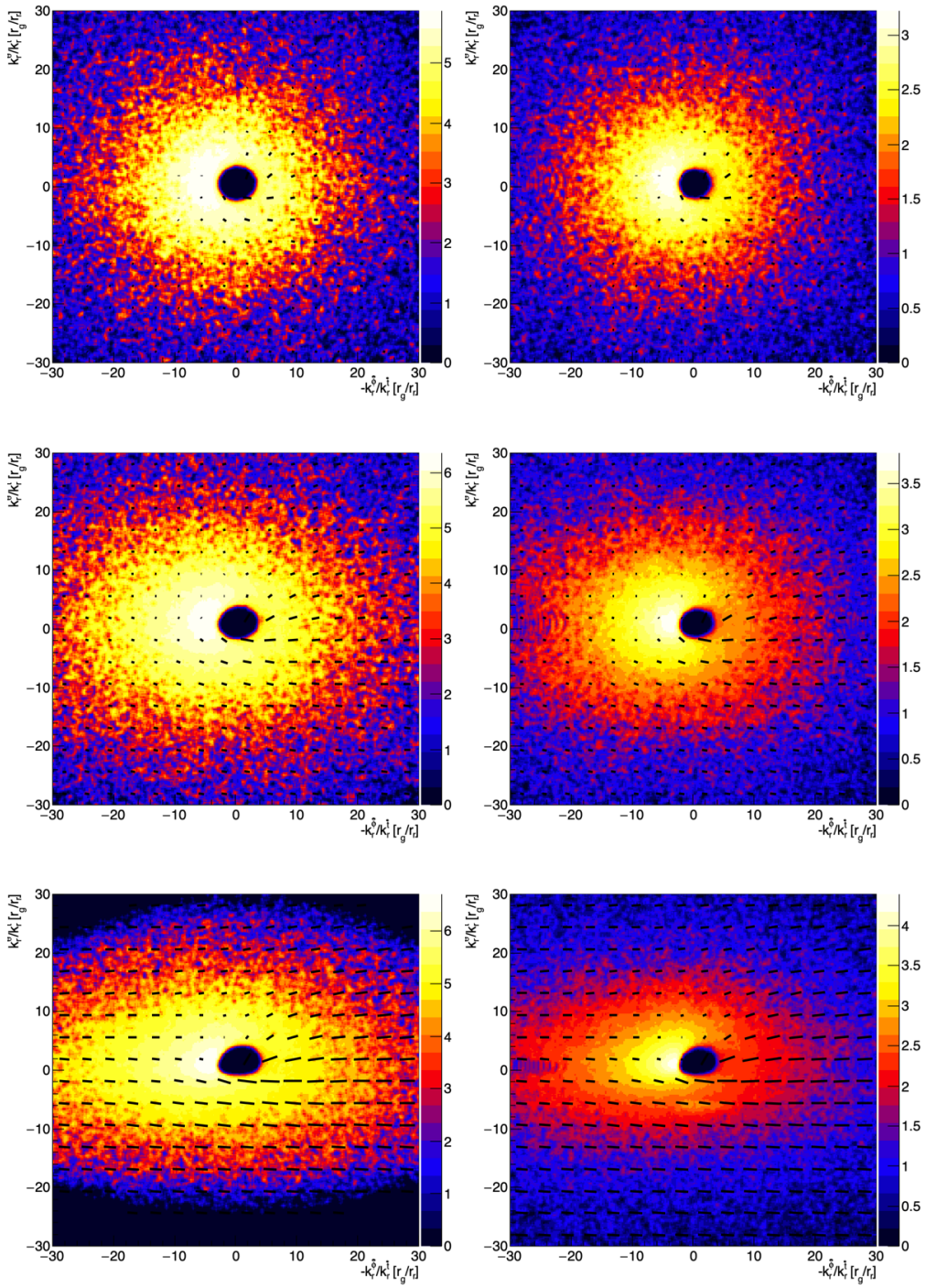

Fig. 4.4: Direct emission of Boyer-Lindquist thin disk (left) and Kerr-Schild pseudo-thin disk (right). Color here is logarithmic intensity and in arbitrary units. These images are for inclinations of $i = 25°$, $45°$, and $65°$ moving from the top row to the bottom row.

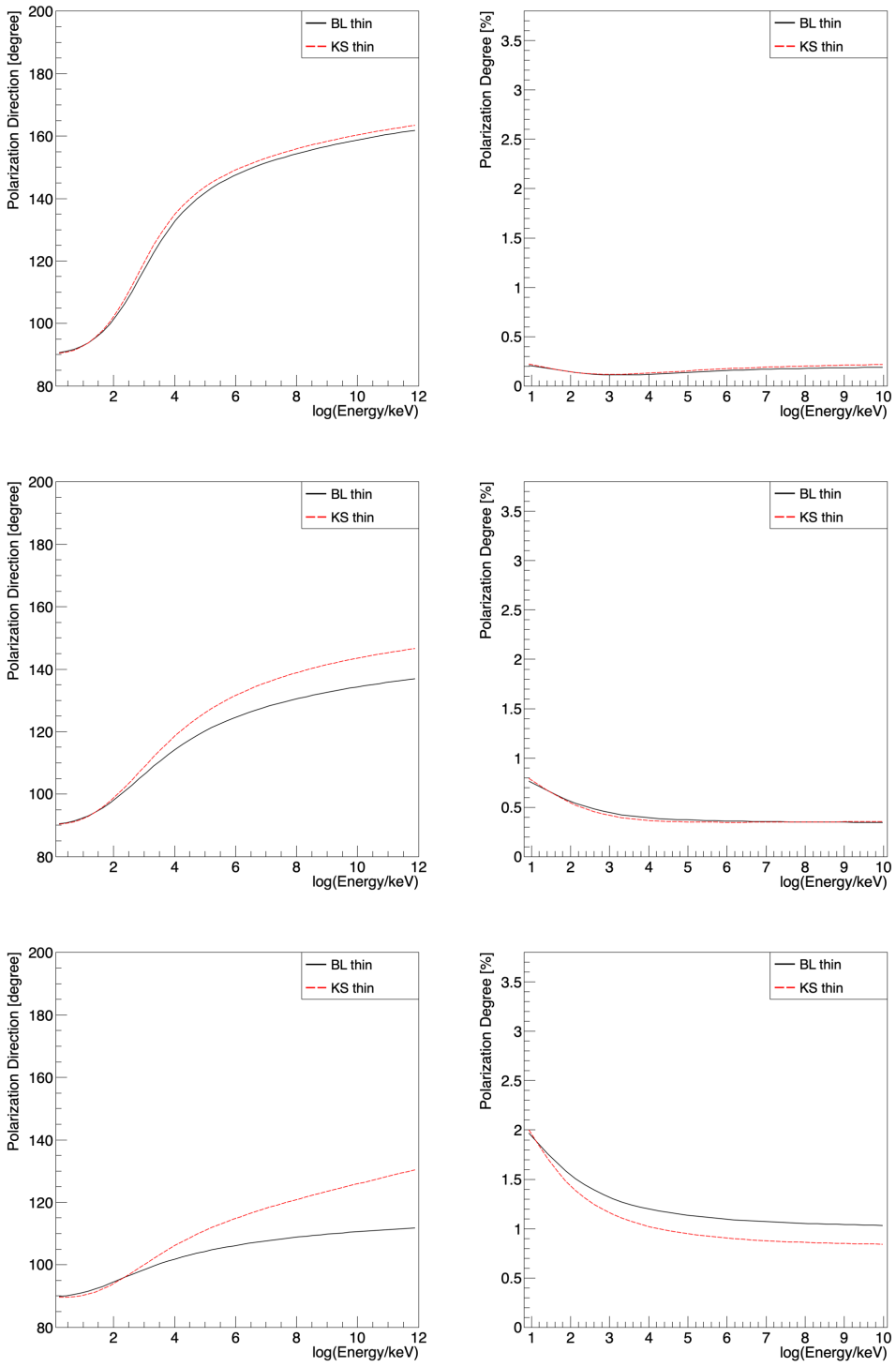

Fig. 4.5: Polarization angle (left) and degree (right) of the direct emission for inclinations of $i = 25°$, $45°$, and $64°$. At $i = 25°$ there is good agreement between the Boyer-Lindquist result and the Kerr-Schild result. at $i = 45°$ the angle agrees at low energies and the polarization degrees align closely. At a moderately high inclination of $i = 65°$ both the polarization angle and degree begin to diverge for energies above ~ 2 keV.

Comparison of the polarization spectra is evaluated more rigorously in Figure 4.5, with the polarization angle on the left and the polarization degree on the right. These plots are for the same inclinations as Figure 4.4. At low inclinations, the spectra are nearly identical. As the inclination increases to $i = 45°$, the polarization angle begins to deviate from the Boyer-Lindquist case. At $i = 65°$, both the polarization angle and degree deviate. Note that the deviations are maximal at high energies. In comparing the images and spectra for the total emission in Figures 4.6 and 4.7, these discrepancies become larger. For the Kerr-Schild case the polarization angle is higher across all inclinations, though its swing to vertical happens at approximately the same energies as the Boyer-Lindquist thin disk. The polarization degree shows deviations at high energies at low inclinations. As the inclination increases, these deviations shift to lower energies and grow larger in magnitude. These discrepancies are attributed to higher statistical error on the integration of the geodesic equation and parallel transport of the polarization vector at small radii. As mentioned in Section 4.2.1, the integration of the geodesic equation in Kerr-Schild coordinates cannot be parameterized into an integration of only r and θ as it can in the Boyer-Lindquist case. The lack of symmetry in the disk and high spin of the black hole also play a role. Errors are kept as low as possible by minimizing step sizes below the Boyer-Lindquist thresholds throughout the integration, but remain non-negligible in the Kerr-Schild case nonetheless.

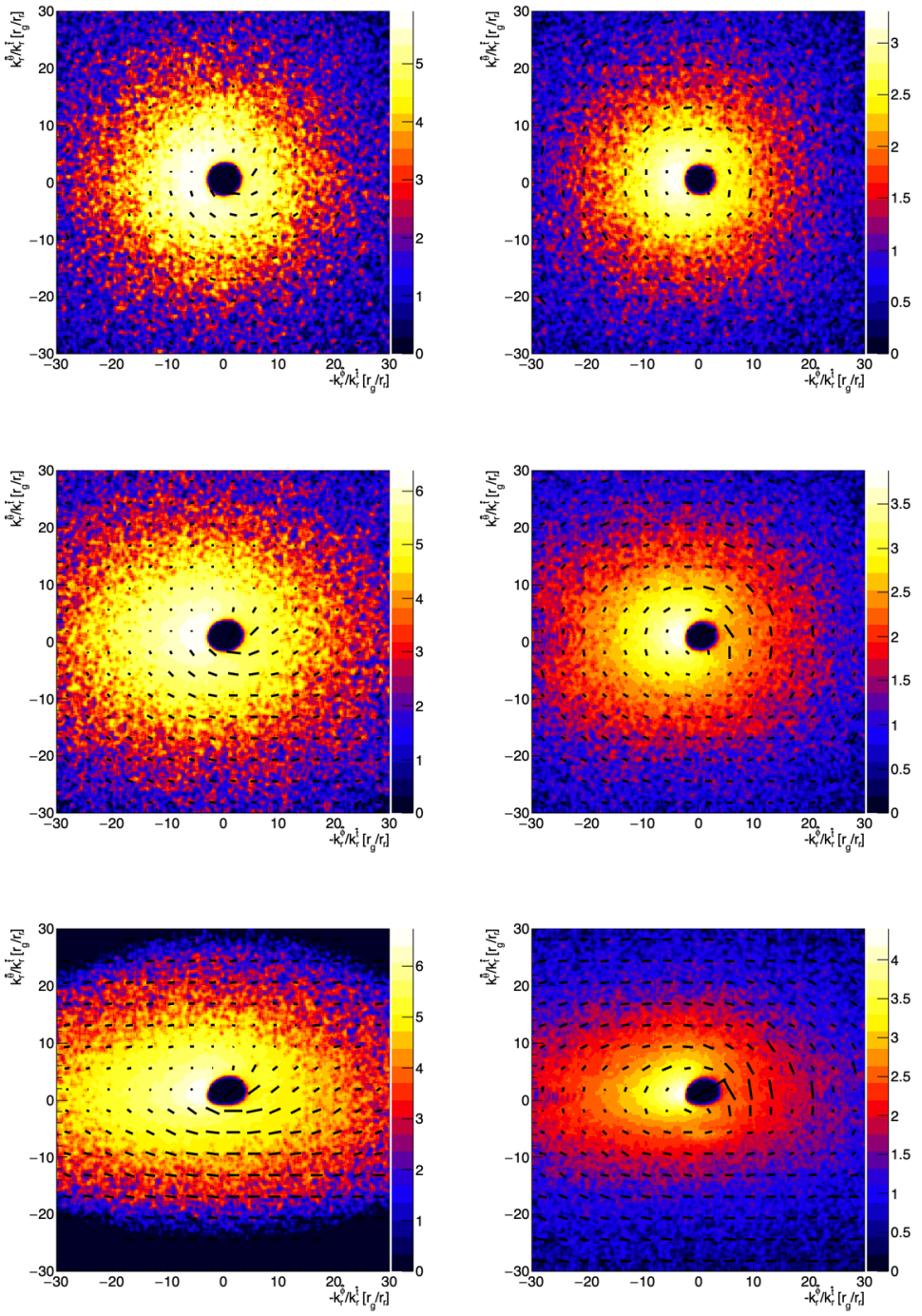

Fig. 4.6: Total emission of Boyer-Lindquist thin disk (left) and Kerr-Schild pseudo-thin disk (right). Color here is logarithmic intensity and in arbitrary units. These images are for inclinations of $i = 25°$, $45°$, and $65°$ moving from the top row to the bottom row.

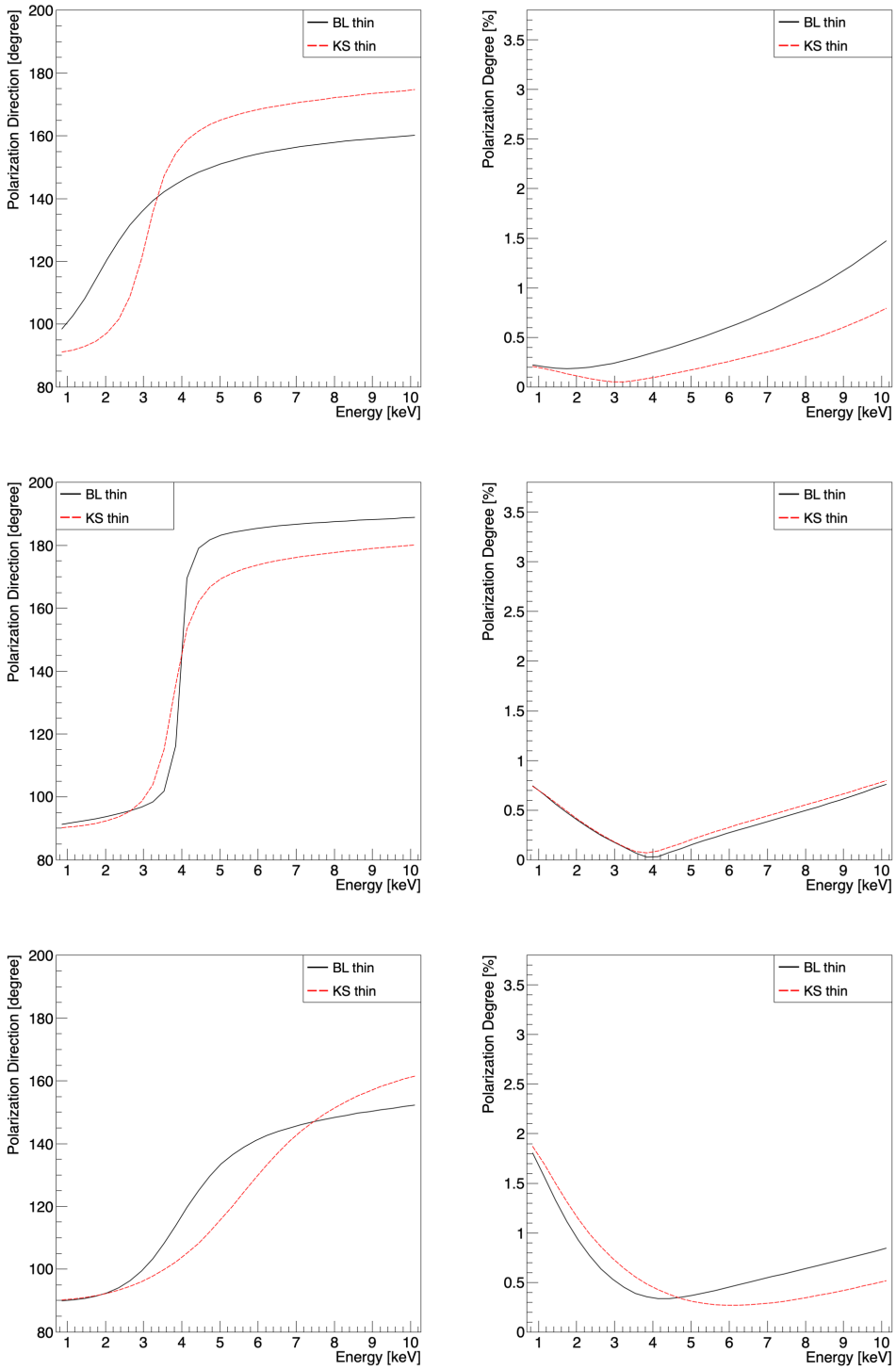

Fig. 4.7: Total emission over inclinations of $i = 25°$, $45°$, and $65°$.

4.6.2 Fe-Kα Line Profile

To compare Fe-Kα line profiles, the axially aligned lamppost model described in Section 4.5. The disk is taken as a frame of the of the *H-AMR* data when it is in a Bardeen-Petterson alignment and projected into the equatorial plane. Small deviations in θ_{disk} are added such that $\theta_{disk} = \frac{\pi}{2} + 0.1 * \delta\theta$ where $\delta\theta$ is a random number in the range $(-1, 1)$. The disk is then given a Keplerian velocity profile. The tilt angles from the *H-AMR* data are left at their original values and the conditional check for gaps in the disk is left in the scattering algorithm as a test. The lampposts emit isotropically over all solid angle. Photons impinging on the disk from above are reflected upwards, those impinging from below are reflected downwards, and photons whose trajectory passes through the gap in the disk are allowed to continue without interruption. The accuracy of this scattering algorithm is evidenced in Figure 4.8. This figure shows a random selection of photon geodesics (black lines) from each lamppost projected into cylindrical coordinates, with the trajectories being truncated at a radial distance of $20r_g$. A schematic of the disk is overplotted in blue.

The Fe-Kα profiles are not given any weighting. These raw Fe lines are compared against the raw Fe lines for a lamppost over the Boyer-Lindquist thin disk. Each line is normalized to its own flux before comparison. Doppler maps of reflected emission for the Kerr-Schild disk and the Fe-Kα lines for the Boyer-Lindquist and Kerr-Schild disks are compared in Figure 4.9 for inclinations of $i = 45°$ (top), $75°$ (middle), and $85°$ (bottom). The Doppler maps show the gap between the inner and outer disks - a remnant of the frame data before it is projected into the equatorial plane. The line profiles between the Kerr-Schild and Boyer-Lindquist disks match closely, with red and blue shifts for each being equal. Interesting to note is that in all three inclinations, the peak of the line is higher in the Boyer-Lindquist case than in the Kerr-Schild case, though the difference is small.

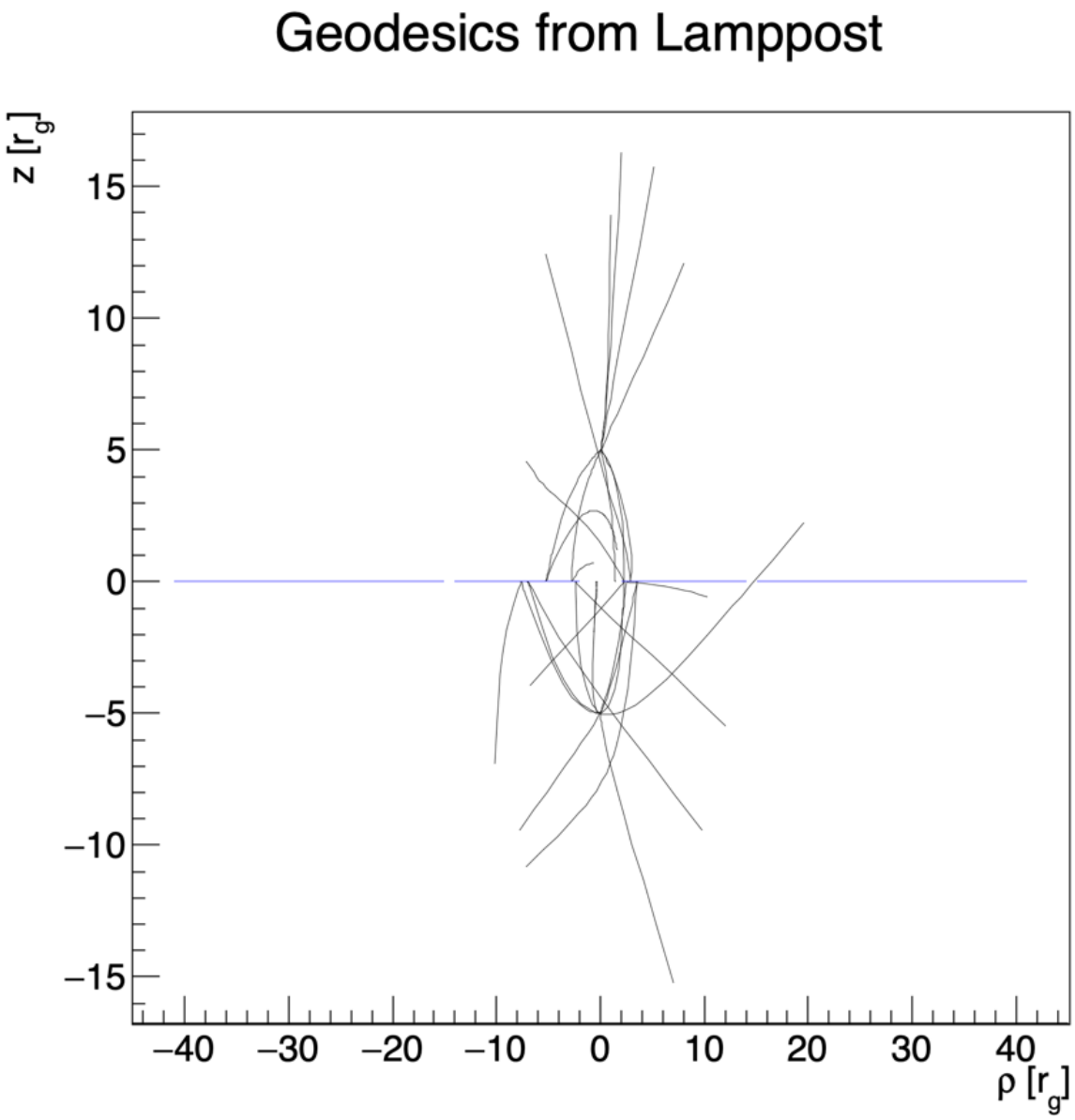

Fig. 4.8: Geodesics from two lampposts are shown in black. The blue line is a schematic of the projection of the disk into the equatorial plane with the gaps visible at $\sim 13r_g$.

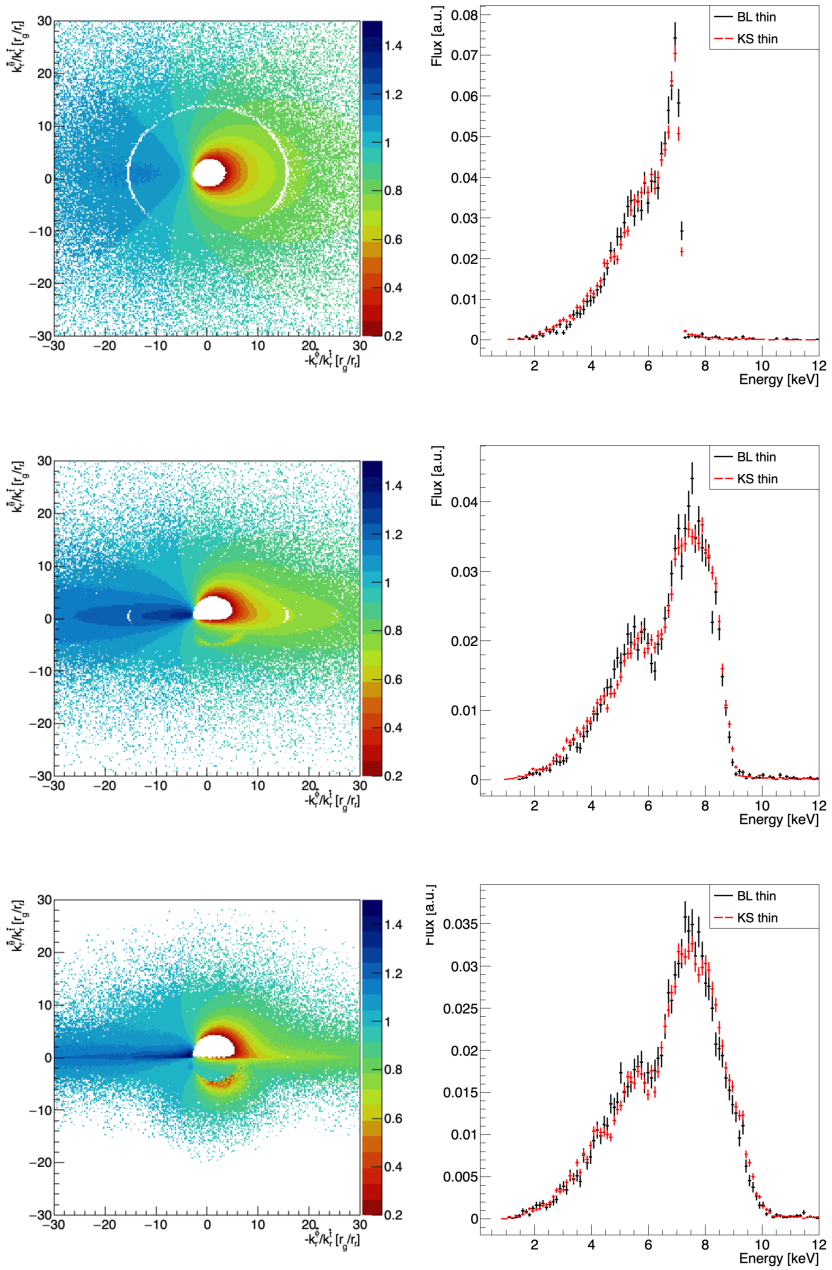

Fig. 4.9: Doppler maps of the blue/red shift of reflected emission for the Kerr-Schild thin disk are on the left. Raw Fe-Kα lines are shown on the right for both the Boyer-Lindquist (black) and Kerr-Schild disks (red) for inclinations of $i = 45°$ (top), $75°$ (middle), and $85°$ (bottom).

Chapter 5

Observational Characteristics of Dynamically Evolving Accretion Flows

5.1 Introduction

Chapter 5 details the results of postprocessing the *H-AMR* for the data set described in Chapter 3 with the raytracing code described in Chapter 4. In all, the raw raytracing data used to produce these results totalled in excess of 5 Pb. These results are being prepared for publication. In particular, Section 5.2 represents a unique and important result, the first of its kind. A selection of images has been included in this chapter, and those interested will find many movies of the raytraced accretion flow which can be viewed here[2].

The *H-AMR* data set is large, with the full runtime of the simulation being $\sim$ 3000 frames. Each of these frames is $\sim 50\frac{r_g}{c}$ in temporal width. The main tearing event occurred over the range $40,000\frac{r_g}{c} \leq t \leq 80,000\frac{r_g}{c}$. This temporal range is the primary focus of the analysis that follows. For all of the analysis in the following sections, only two inclinations

[2] https://www.youtube.com/channel/UCs4DWHchu3DHuFZ-cPhyDxA

will be considered, $i = 27°$ and $65°$. This is due simply to the computational and storage demands of the calculations. These inclinations were chosen as they correspond Cyg X-1 ($27°$ [128]) and GRS1915+105 ($65°$, [129]), the latter of which is a known source of hfQPOS [43]. A variety of azimuths are explored for each of these inclinations, and will be denoted as Φ. $\Phi = 0$ is defined as the azimuthal direction of the net angular momentum vector of the disk at $t = 0$. It has no deeper physical meaning and may be considered an arbitrary value by which the azimuthal orientation of the observer with respect to the black hole is measured, with some $\Phi = 0$ being constant for all inclinations and times.

The chapter begins with a time domain analysis of the X-ray emission of the disk over the course of the tearing event. These results are related back to the geometry and dynamics in the accretion flow itself. Section 2 contains an analysis of the Fe-Kα emission from a co-rotating lamppost. The effect of the differentially precessing disk geometry on the shape of the Fe-Kα line is evaluated, as well as the time domain behavior of its centroid. Section 3 details the behavior of the polarization degree and angle over the course of the tearing event. The chapter closes with a discussion of the results and their impact on the field. The results of the time domain analysis of Section 1 are well vetted and being prepared for publication. The sections on the Fe-Kα line profiles and polarization represent first results. Additional simulations are in progress that will reduce the statistical errors on these results and will be described in a forthcoming publication.

5.2 Quasi-Periodic Oscillations

5.2.1 Analysis Methods

As discussed in Section 3.3.3, oscillatory signals were discovered in the radial accretion rate $\dot{M}_r$ at the outer edge of the inner disk, located at $\sim 13\ r_g$. The strongest of these signals was at 55Hz, while the second signal was weaker - too weak to be definitive - at 110Hz. The 55Hz oscillation corresponds to the radial epicyclic frequency of that radius $\sim 13rg$. Here, the thermal emission from the frames in the range $40,000\frac{r_g}{c} \leq t \leq 80,000\frac{r_g}{c}$ is evaluated. For each frame, $\sim 1.5 \times 10^9$ photons are generated. Multiple frames are loaded at a time and the disk geometry is updated for scattering to that configuration which is closest to the photon's age.

Counts are added to the lightcurve based on the received flux in arbitrary units. As described in Section 4.4, each photon contributes a statistical weight of

$$\omega_{st} = 2\pi\Delta r\sqrt{-g_{tr\phi}}\frac{\mathcal{F}}{\langle\hat{E}\rangle}\omega_i \tag{5.1}$$

where Δr is the width of the emission bin, $\sqrt{-g_{tr\phi}}$ is the invariant area measured in the global frame, and $\mathcal{F}$ is the flux of emission in the plasma frame and $\langle\hat{E}\rangle$ is the average emission energy in the plasma frame. The weights of emission and all scattering processes are encoded in ω_i. For an energy bin bounded below by $E1$ and above by $E2$ each photon then contributes with a weight of

$$\omega = \omega_{st}\frac{\int_{E1}^{E2}\frac{E^2}{e^{E/\epsilon_0}-1}dE}{\int_0^\infty\frac{E^2}{e^{E/\epsilon_0}-1}dE} \tag{5.2}$$

As the photons are statistical packets, each photon contributes to the lightcurve a weight

equal to the sum of all ω over all energies to the lighcurve bin corresponding to the photon's receipt time at the observer. In practice, the raw data from each frame is filled into a lightcurve of 4096 bins covering the range $0\frac{r_g}{c} \leq t_{lc} \leq 160,000\frac{r_g}{c}$ giving $\sim 40\frac{r_g}{c}$ wide bins. This is a slightly smaller cadence than the binning of the frames themselves, ensuring that no frame to frame variation can be lost. For a black hole of $10M_\odot$ and a spin of $a = 0.9375$ these $\sim 40\frac{r_g}{c}$ wide bins correspond to a wall clock time width of 3.8 ms. After all the lightcurves are generated they are combined into a single lightcurve of identical dimension.

The lightcurve is then taken to Fourier space and the power spectral density computed using the Stingray timing package [130, 131]. Stingray leverages the Fast Fourier Transform (FFT) functionality of numpy to compute the Fourier transform of the lightcurve. The magnitude of oscillations at a given frequency is measured with the power spectral density,

$$P(\nu) = \lim_{t\to\infty} \frac{1}{\nu} |\hat{f}_t(\nu)|^2, \tag{5.3}$$

where T is the period of the signal, $\hat{f}_t(\nu)$ is the Fourier transform, and ν is the Fourier frequency. The power spectra that follow are all normalized with the fractional RMS.

5.2.2 Emission Characteristics of the Evolving Accretion Flow

The details of the *H-AMR* data set were discussed in detail in Chapter 3, but are reviewed briefly now. The disk is initialized at an inclination of 65° with respect to the black hole spin. As time passes, the Lense-Thirring torques from the dragging of spacetime due to the black hole's spin build. Eventually, these torques exceed the vicsous torques holding the disk together, inducing a tearing event. During a tearing event, the disk splits into two (or more) distinct sub-disks, which begin differentially precessing at the Lense-Thirring precession frequency. Figure 5.1 shows images of the disk at various times before and during

the tearing event. These disk images are constructed by back projecting the photon wave vector $\mathbf{k}^{\mu}$ into a plane intersecting the black hole spin axis and orthogonal to the line of sight. The color scale is log intensity in arbitrary units.

These tearing events are accompanied by an increase in the accretion rate as integrated over the null surface of the event horizon. This corresponds to an increase in the luminosity across the inner sub-disks. The lightcurves from the tearing event reflect this increase in luminosity clearly as shown in Figure 5.2. Here, the x axis has been converted from scale free units of $\frac{r_g}{c}$ to seconds. The tearing event begins at $\sim$ 4 seconds and ends at $\sim$ 8 seconds. The light curve is shown for two inclinations, $i = 27^{\circ}$ and 65°. Note that at the higher inclination the features are broadened, an effect induced by the relativistic motion of the accreting plasma. The 4 peaks in the count rate visible here between 4 and 8 seconds correspond to the four peaks in the accretion rate shown in Figure 3.8.

The lightcurve is taken to Fourier space and the power spectral density (PSD) is computed. To begin, the raw, unaveraged PSD is computed. In all PSD plots that follow, the frequency is on the X-axis and frequency$\times$power is plotted on the Y-axis. The raw PSDs for a variety of azimuths are given in Figure 5.3. There are a few important features to note in this figure, with the first and most obvious being the appearance of between 2 ($i = 27^{\circ}$, $\Phi = 274$) and 4 ($i = 65^{\circ}$, $\Phi = 154$) peaks. The largest peak, present at every azimuth for both inclinations, is spread over a frequency range of 55 Hz $\leq \nu \leq \sim$ 59 Hz, with its centroid at $\sim$ 57.5 Hz. (recall that the oscillation observed in $\dot{M}_r$ was at 55 Hz). This 57 Hz peak is the fundamental frequency of the oscillations. The second largest peak is spread over a frequency range of 113 Hz $\leq \nu \leq \sim$ 116 Hz with a centroid occurring at $\sim$ 115 Hz. This peak is the second harmonic, or octave, of the fundamental frequency, occurring almost exactly in a $2:1$ ratio depending on azimuth. Some observers ($i = 65^{\circ}$, $\Phi = 154^{\circ}$) also see a third peak spread over a frequency range of 87 Hz $\leq \nu \leq \sim$ 90Hz, frequency peak at $\sim$ 89 Hz, which is

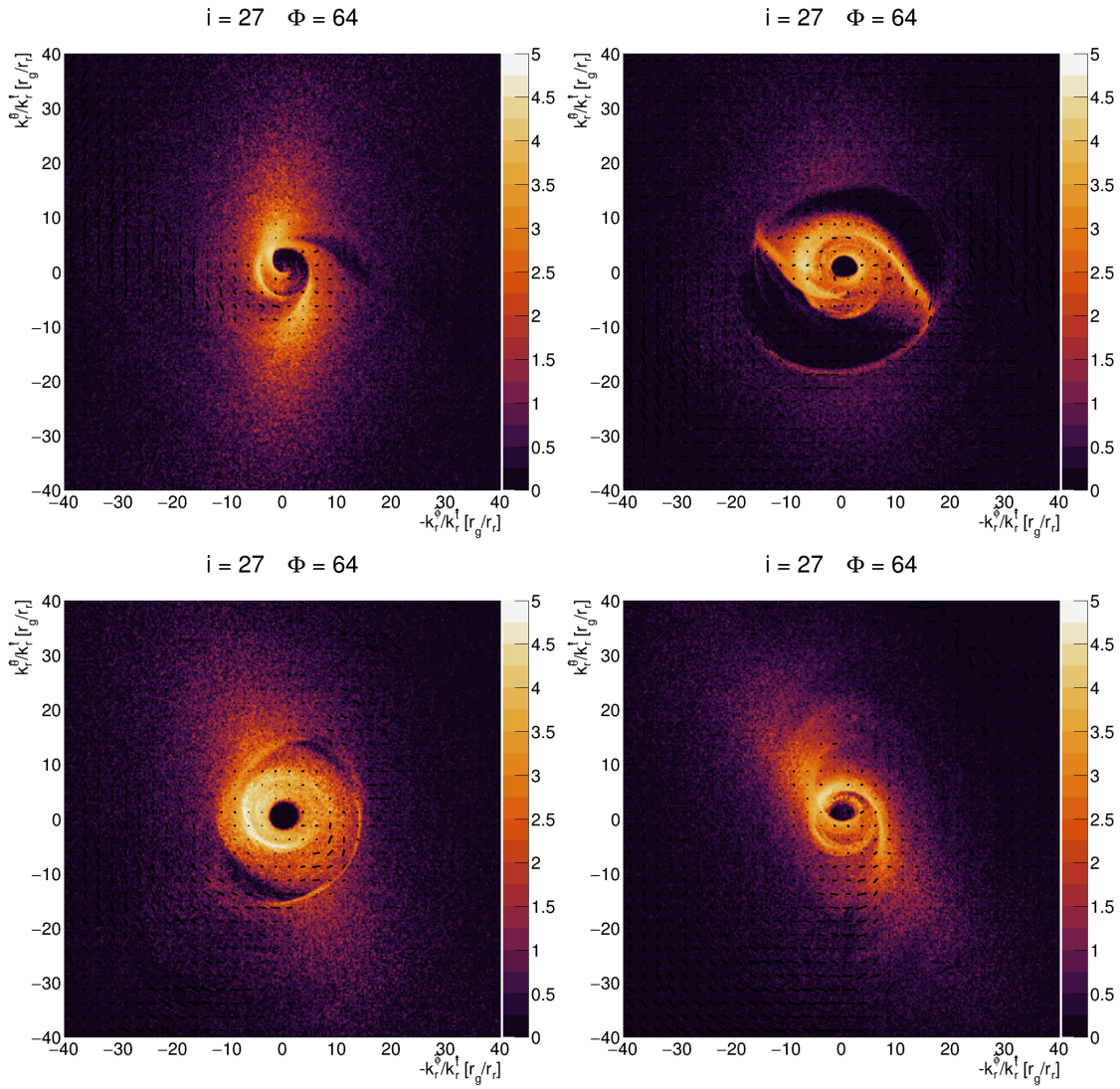

Fig. 5.1: Four images of the disk for an inclination of $i = 27°$ and an azimuth of $\Phi = 64°$. Overlaid on the images are bars denoting the polarization degree and angle. These images progress forward in time from left to right and top to bottom, with the upper left being just before the tearing event begins and the bottom right being just after it ends.

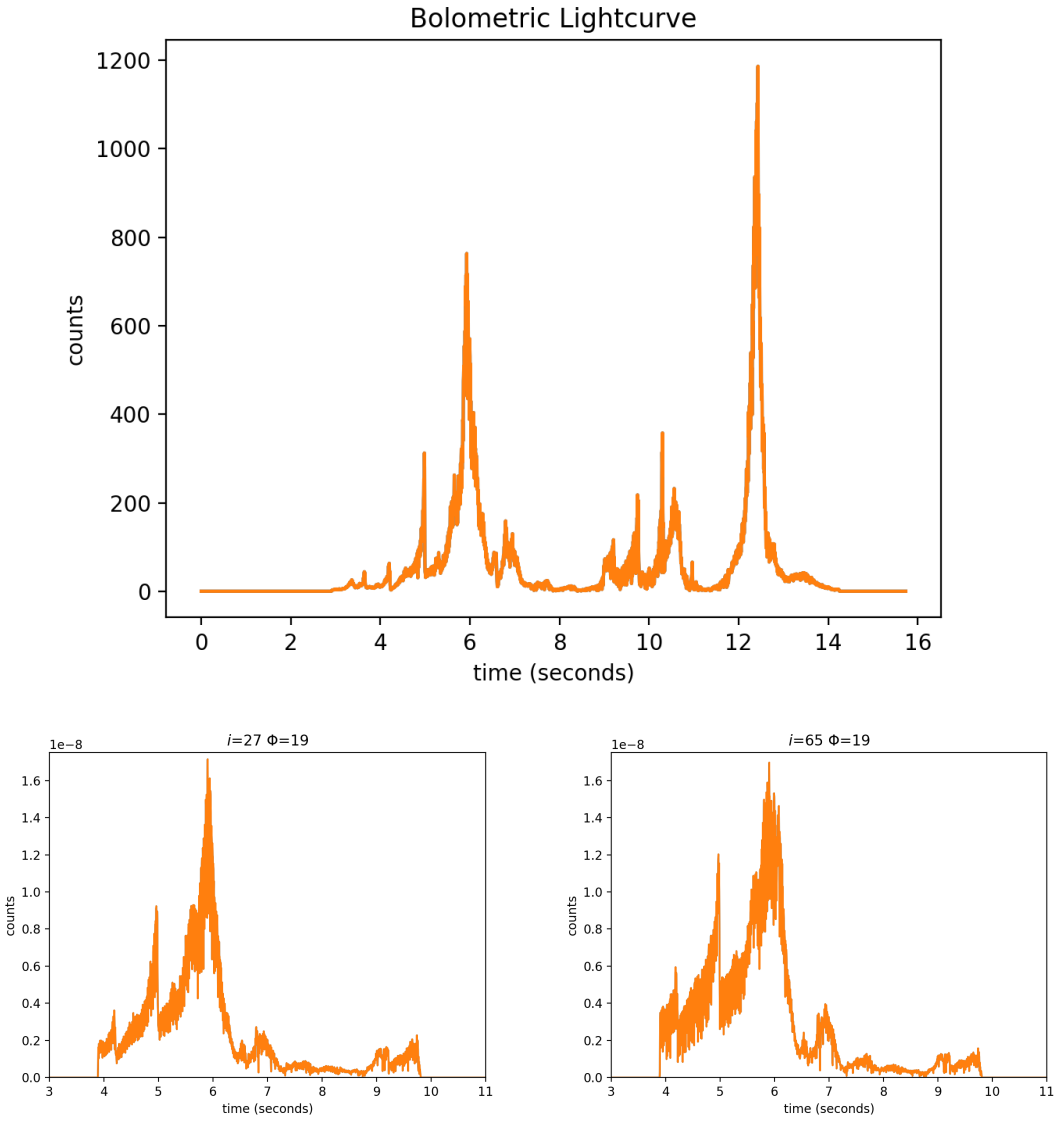

Fig. 5.2: Lightcurves generated by raytracing the H-AMR data from a simulation of a $10M_{\odot}$ black hole with spin $a = 0.9375$. The accretion disk is initially misaligned at 65°. **Top**: Bolometric lightcurve over the runtime of the simulation. The 'counts' for all lightcurves are in arbitrary units. **Bottom**: Lightcurves of total emission for the two inclinations at an azimuth of $\Phi = 19°$. Note the broader features at the higher inclination of $i = 65°$. This is a product of relativistic beaming due to the orbital motion of the plasma.

in a 3 : 2 ratio with the fundamental peak. There also exists a narrow low frequency peak centered at ~ 3 Hz.

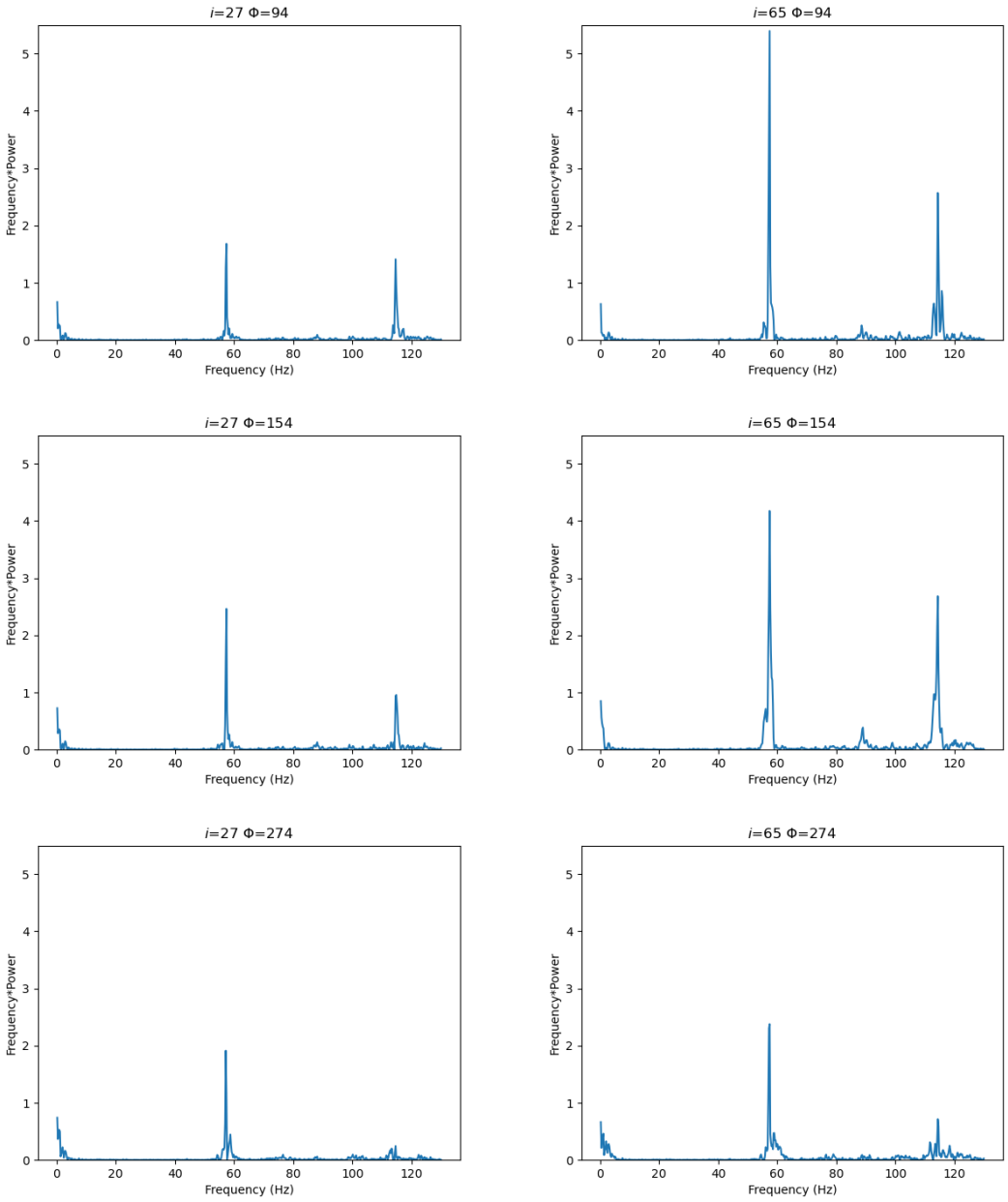

Fig. 5.3: Raw (unaveraged) power spectral density of total emission for the two inclinations at azimuths of $\Phi = 94°$, $154°$, and $274°$.

Unsurprisingly, these signals are present in the reflection spectrum for most inclinations and azimuths. Figure 5.4 shows one azimuth for each inclination. At some azimuths there is less power in the reflection spectrum at $i = 65°$ than $i = 27°$. This is likely due to the occulting of the inner disk and the outer disk, which is aligned at approximately 65° during the tearing event.

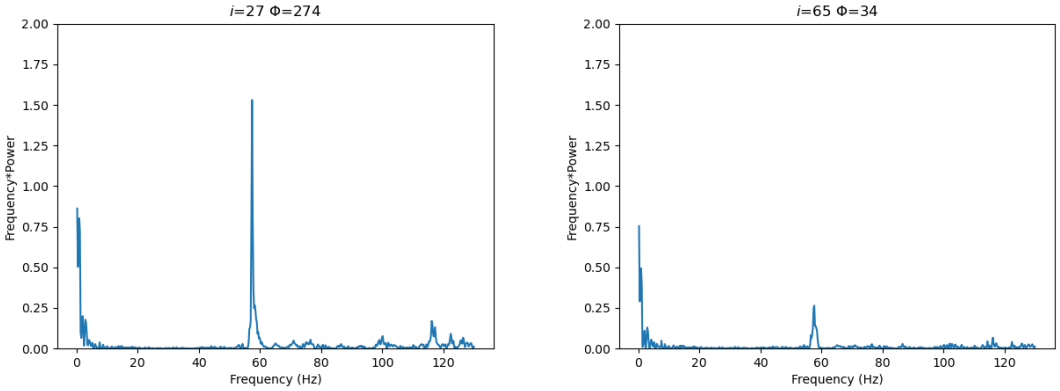

Fig. 5.4: Reflection PSD

Plotting these PSDs in log-log form and averaging the FFT before computing the PDS reduces the noise and makes the signals more apparent. For the following PSDs in Figure 5.5, the lightcurve was limited to the range 4-8 seconds. The lightcurve is cut into 4 intervals of length 1 second and the FFTs of each segment are averaged together before the PSD is computed. These PSDs were chosen in particular to illustrate that the lfQPO does not always increase in power as the inclination increases.

The quality of and power in these signals is quantified by fitting a Lorentzian of the form

$$f(\nu) = \frac{A\gamma^2}{\gamma^2 + (\nu - \nu_0)^2}. \tag{5.4}$$

Here, A is a constant of the fit, γ is half of the full width at half maximum (FWHM), and ν_0 is the centroid frequency. The quality factor is taken as $Q = \nu/FWHM$. Overplotting

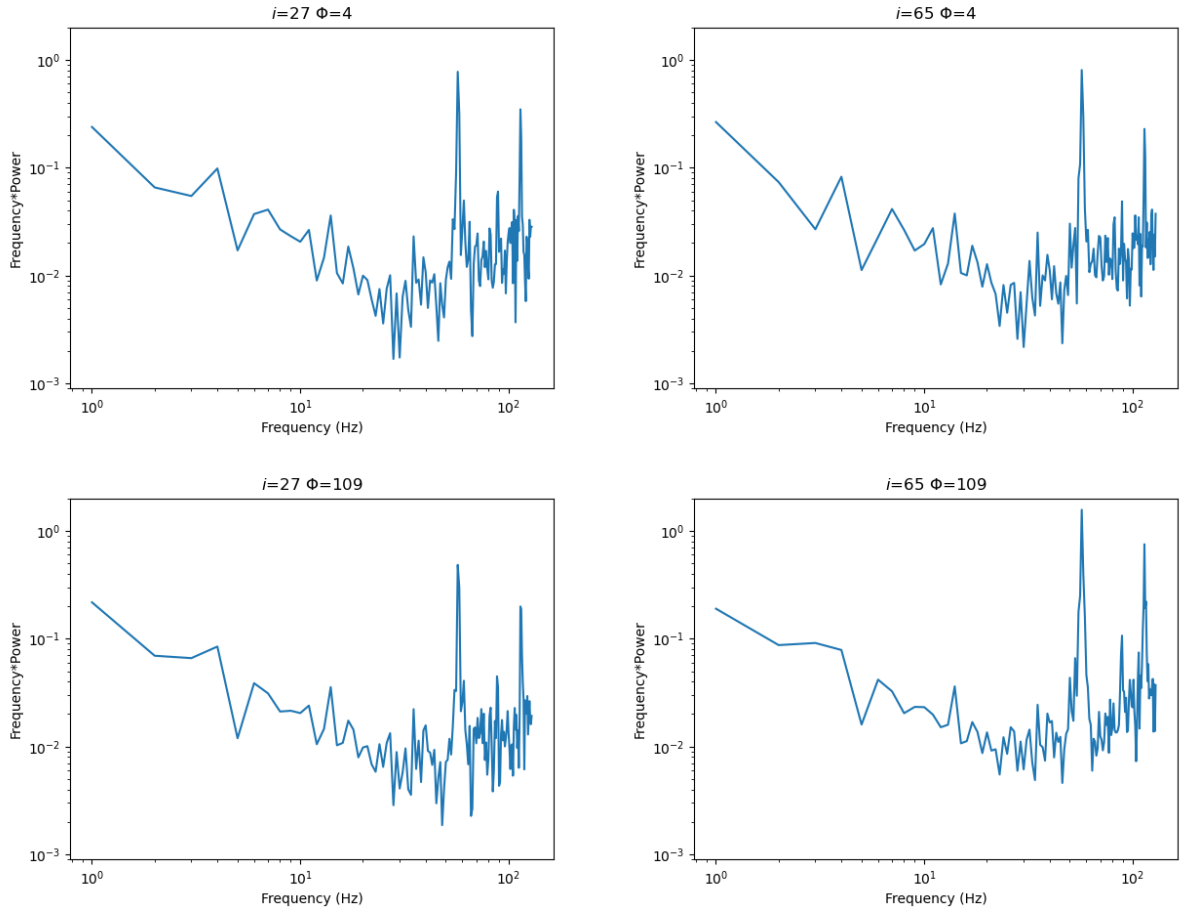

Fig. 5.5: Power spectral density for inclinations of $i = 27°$ (left) and $i = 65°$ (right) at azimuths of $\Phi = 4°$ (top) and $\Phi = 109°$ (bottom)/ The 57.5 Hz peak and its first octave at 115 Hz are visible at all four orientations, as is the low frequency ~ 3 Hz oscillation to a varying degree.

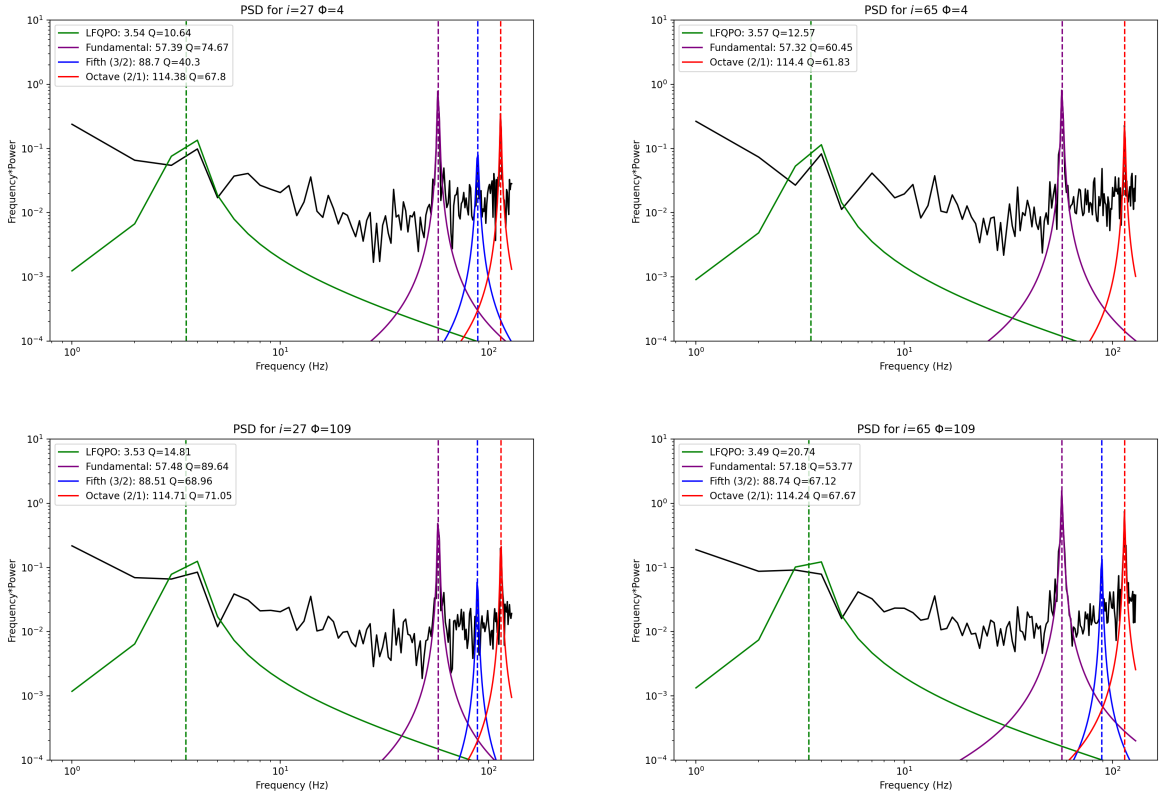

Fig. 5.6: Lorentzian fits for the spectra in Figure 5.5.

the fit on the PSD can obscure the peak itself, so for clarity the fits in Figure 5.6 are for the same spectra from Figure 5.5. The quality factor of the hfQPO fits are high, a reflection of the power in the signal and the narrow frequency band of the oscillations.

The most important question underlying these results concerns the origin of the oscillations. Recall that Musoke et al [81] found a 55 Hz oscillation in $\dot{M}_r$ isolated at the tearing radius ($\sim 13r_g$), corresponding to the radial epicyclic frequency at this radius. Intuitively then it seems likely that these signals are emanating from the outer edge of the inner disk. To ascertain this, the lightcurve is broken into $1r_g$ wide bins based on the last interaction radius (i.e., emission radius for direct emission or last scattering radius for reflected emission) extending from the event horizon to $50r_g$. For each radial bin three lightcurves are

computed, one for the total emission, the direct emission, and the reflected emission. These lightcurves are then taken to Fourier space where the PSD is computed identically to those shown above.

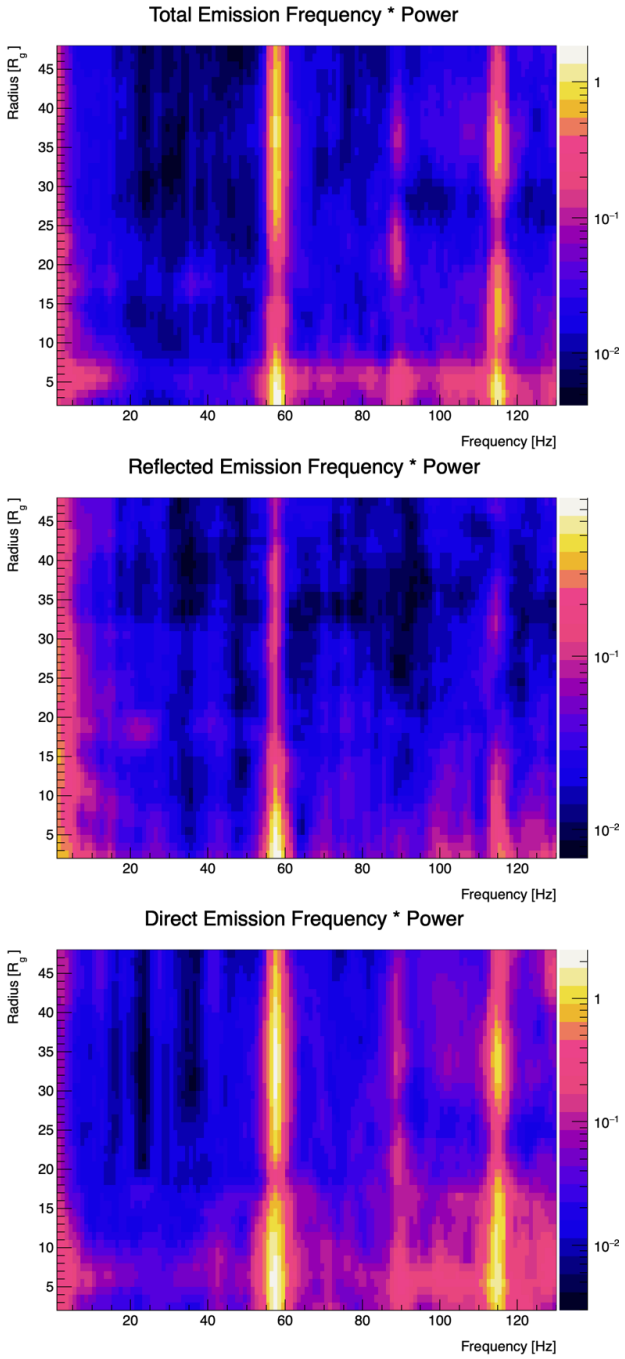

Fig. 5.7: PSD maps for $i = 27°$, $\Phi = 4°$. Note that for $10 \leq r \leq 20$ there is diminished power in the fundamental frequency and increased power in octave.

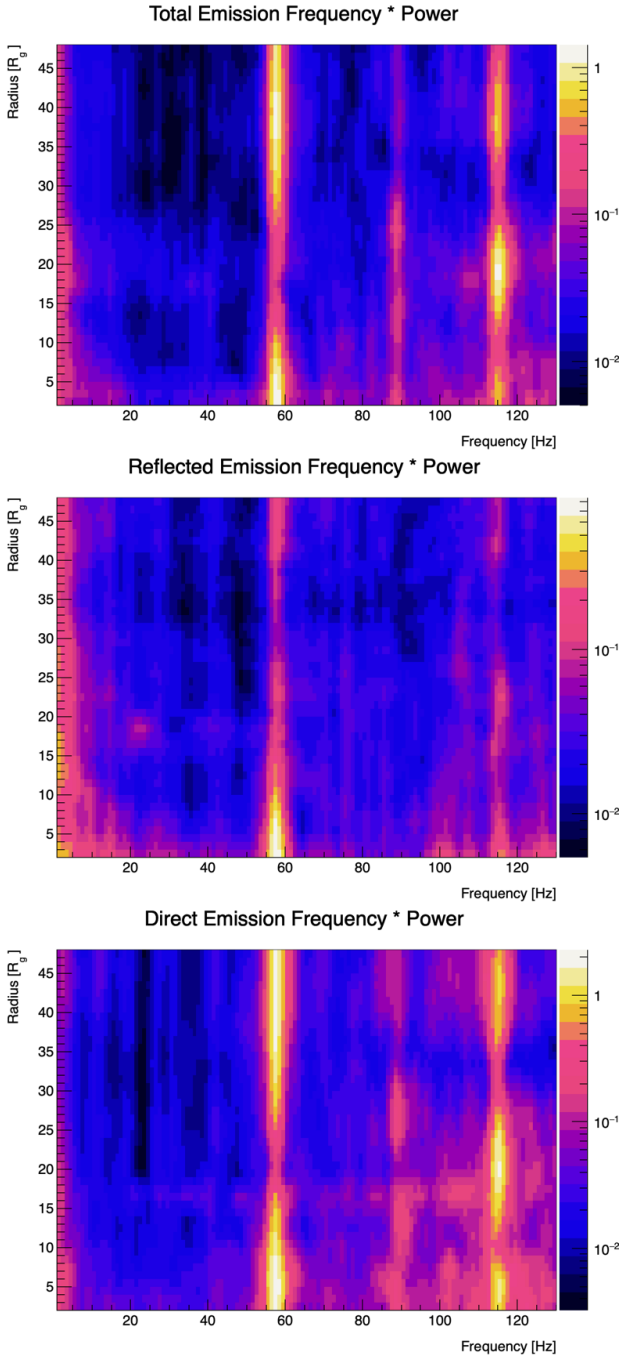

Fig. 5.8: PSD maps for $i = 27°$, $\Phi = 109°$. As in Figure 5.7, diminished power at $10 \leq r \leq 25$ in total emission and $\sim 18 \leq r \leq 20$ in direct emission at the fundamental frequency is accompanied by increased power in the octave.

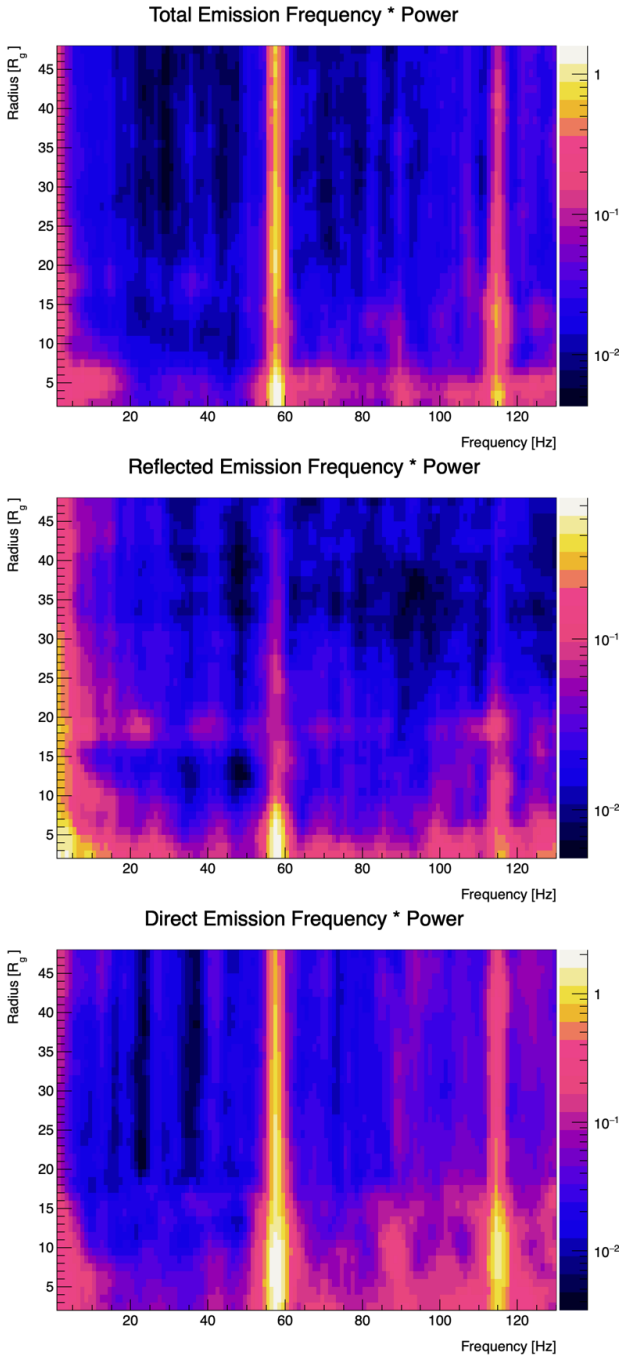

Fig. 5.9: PSD maps for $i = 65°$, $\Phi = 4°$.

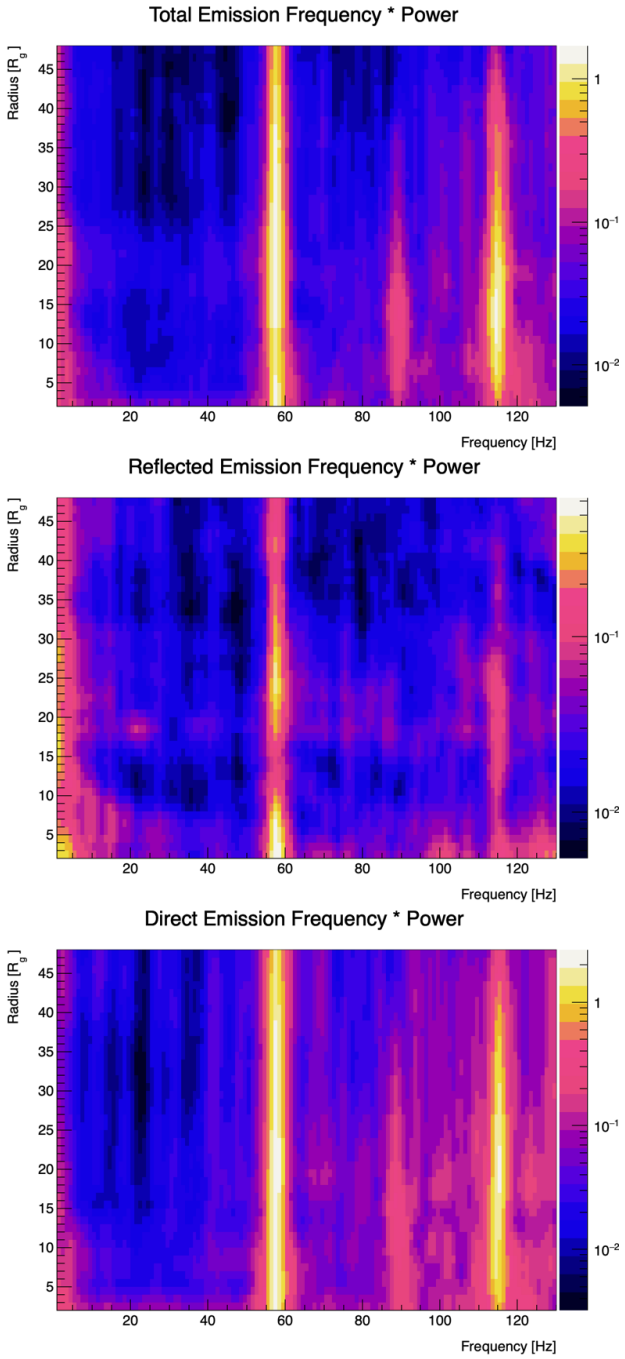

Fig. 5.10: PSD maps for $i = 65°$, $\Phi = 109°$.

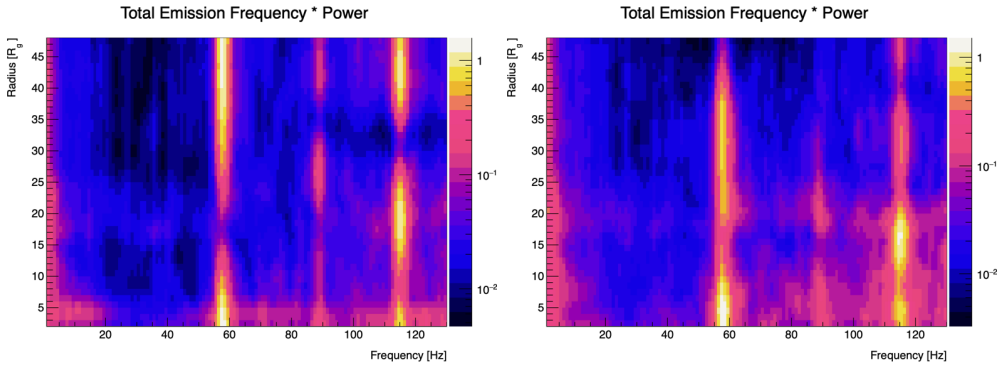

Fig. 5.11: PSD maps for $i = 27°$, $\Phi = 64°$ (left) and $i = 65°$, $\Phi = 304°$ right.

These PSD maps reveal an unexpected result - the fundamental frequency of the hfQPO and its harmonics (when present) are global modes, emanating from both within the inner disk and throughout the outer disk. An interesting pattern emerges in the case of $i = 27°$, $\Phi = 109°$, where diminished power in the oscillation at a given radius in the fundamental frequency corresponds to an increase of power in the harmonic at that same radius (see Figure 5.8). This trend is repeated across both inclinations at a variety of azimuths, implying that the harmonic is in fact due to a resonance in the fundamental frequency, see Figure 5.11.

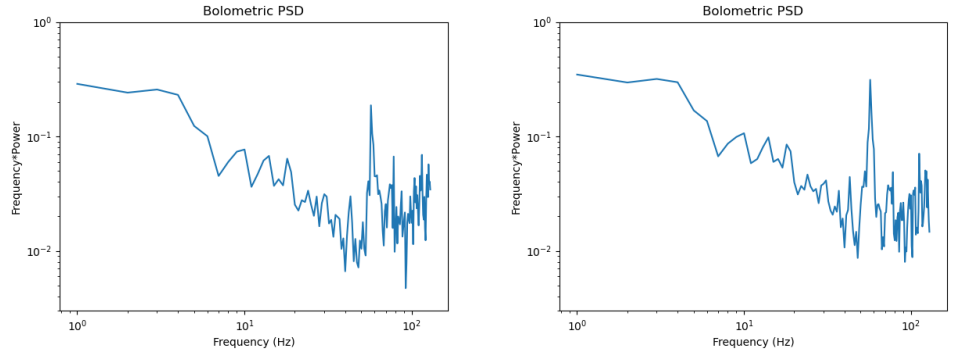

Fig. 5.12: Bolometric PSD for total emission (left) and reflected emission (right).

To quantify whether the visibility of these oscillations is dependent the viewing angle, a lightcurve is integrated over all observer orientations (i.e., all solid angle) and taken to

Fourier space where its power spectral density is examined. Figure 5.12 shows this result for the total and reflected emission. The fundamental frequency of the hfQPO and the lfQPO are visible for all observers in both the total emission and the reflected emission. A number of smaller peaks from the i,Φ PSDs carry over at low frequencies. These are due to the warped and differentially precessing inner disk tearing into sub-disks as it evolves toward Bardeen-Petterson alignment. One high frequency peak arises that was not apparent in the individual observer PSDs, either being washed out due to interference or present but of low amplitude. This peak is at ~ 44 Hz. It is possible that was thought to be a $3:2$ harmonic is in fact not related to the fundamental hfQPO frequency at all, but instead is the second harmonic (first octave) of a different oscillation altogether. This 44 Hz frequency corresponds to a radial epicyclic frequency near the inner edge of the outer disk during the tearing event, $\sim 15.5 r_g$. Figure 5.13 shows the frequencies of all of these oscillations against the orbital characteristic frequencies for a $10 M_\odot$ black hole with a spin of $a = 0.9375$.

5.2.3 Discussion

The 55 Hz oscillation in $\dot{M}_r$ observed at the tearing radius in the GRMHD data translates into a spectral hfQPO at ~ 57 Hz in the thermal emission of the disk which is visible at all inclinations and azimuths. This spectral hfQPO is accompanied by a harmonic at ~ 115 Hz that is visible at both inclinations examined, but not all azimuths. In some observer orientations, there is a second harmonic at ~ 88 Hz that arises. Additionally there is an lfQPO that arises from the differential Lense-Thirring precession of the inner disk, also visible to all observer inclinations and azimuths.

Binning the lightcurve into $1 r_g$ wide radial bins and computing the power spectral density reveals that, unlike the oscillation in $\dot{M}_r$, these signals are not isolated to the tearing radius

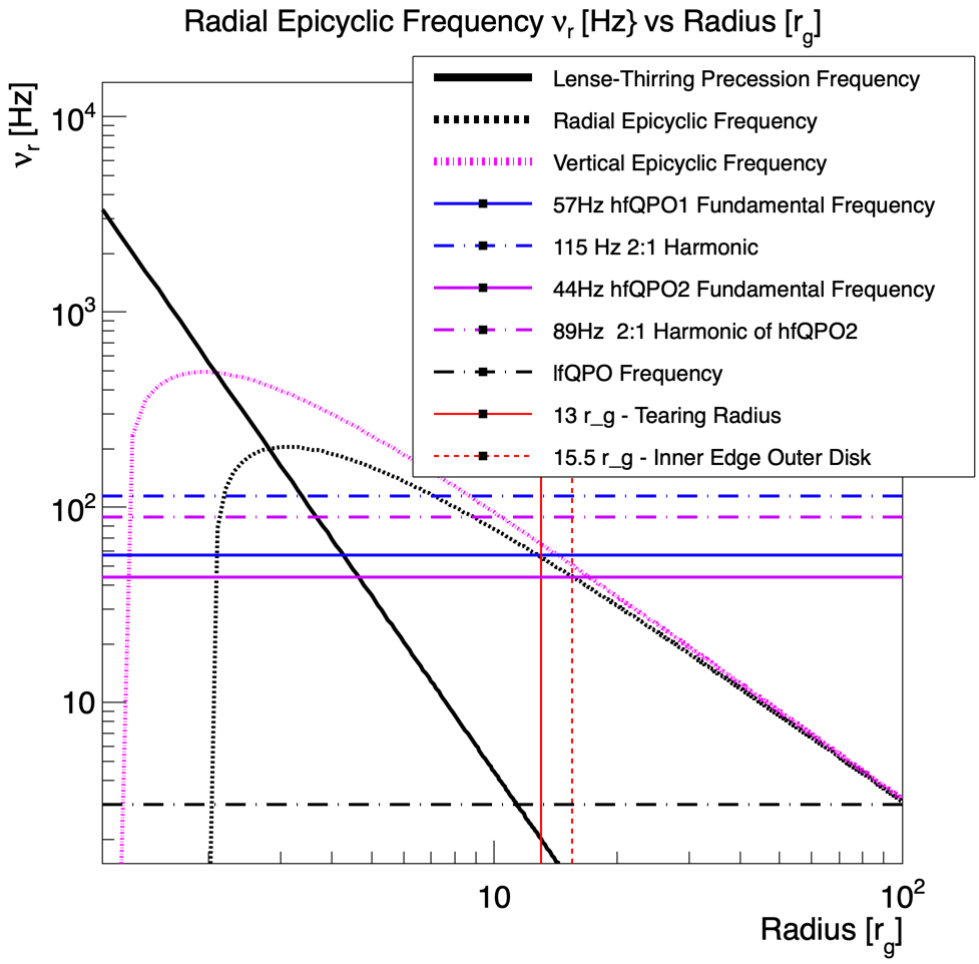

Fig. 5.13: Fundametal orbital frequencies are plotted with the lfQPO and hfQPO frequencies overlaid. The two red vertical lines are the radii where the radial epicyclic frequencies correspond to the two hfQPO frequencies.

but are in fact global modes (Figures 5.7 - 5.10). The fundamental frequency and its octave occur in the direct, reflected, and total emission from the entirety of the inner disk and throughout the outer disk to varying degrees. The third $3:2$ peak is present only in the direct and total emission. When present, this oscillation occurs across the entirety of the inner disk but its presence in the outer disk is less extended than the fundamental and $2:1$ harmonic, typically disappearing after $\sim 30r_g$. The lfQPO is also present as a global

mode from across the entirety of the inner disk and throughout the outer disk to varying extents. Its presence in the direct emission is typically isolated to the inner precessing disk (and sometimes to near the inner edge of the outer disk), but extends across all radii in the reflection spectrum for all observer orientations examined.

There is evidence of a resonance inducing the 2 : 1 harmonic as shown in Figure 5.11. Diminished power in the fundamental frequency at a given radius often (but not always) corresponds to an increase in power in the harmonic, implying self interference in the oscillation itself. This conclusion requires further investigation. The bolometric lightcurve integrated over all solid angle shows that the fundamental hfQPO and the lfQPO are visible to all observers across all inclinations. It also reveals a fourth high frequency oscillation not present (or not of significant amplitude) in the individual observer PSDs at $\sim$ 44 Hz. This oscillation corresponds to a radial epicyclic oscillation near the inner edge of the outer disk at $\sim 15.5 r_g$. It is possible the $\sim$ 89 Hz oscillation thought to be the 3 : 2 harmonic of the fundamental frequency is in fact the first octave of this 44 Hz oscillation, but more investigation is required to determine this definitively.

The source of these oscillations during the tearing event, and their propagation across the disk, is the dynamics of the evolving plasma itself. Preceding the tearing event there is a standing ring of density near the tearing radius. After the tearing event occurs and the disk begins to precess, this ring oscillates in the inner disk. While the inner disk is precessing and oscillating, material is fed from the outer disk to the inner disk(s) via streamers. This process provides a mechanism for the transfer of angular momentum from the inner to the outer disk, causing the inner disk to (eventually) align and the streamers to break off. During this oscillation, angular momentum is being transported outward via these streamers, propagating the 57 Hz and 115 Hz oscillations to the outer disk kinetically via viscosity. If the apparent 3 : 2 harmonic is infact the 2 : 1 octave of the 44 Hz oscillation at the inner

edge of the outer disk, the infalling material in these streamers would provide a mechanism for transporting this oscillation inward to the inner disk in a similar fashion.

5.3 Fe-kα Profiles

H-AMR has been used to simulate numerous thin disks of varying inclination which develop warps and undergo precession to varying degrees without the presence of tearing events. In some of these simulations, jets are formed which expel matter along the poloidal magnetic fields of the disk. During periods of misalignment, warp, and precession, these jets precess with the disk and are aligned with the disk on comparative distance scales (i.e., aligned and precessing with the inner disk on small scales, aligned and precessing with the outer disk on large scales) [79]. It has been shown that steady state geometries diverging from the standard thin disk can have strong effects on the reflection spectra of stellar mass black holes and AGN. Slim disks of moderate scale height self-shadow their inner regions, leading to a truncation of the blue wing of the Fe-Kα line [105, 104], and the boosting profile of Keplerian disks in Bardeen-Petterson alignment can shift the extent of the red wing and change the flux ratios in blue and red shifted emission leading to errors in estimating spin [100]. In nature, a correspondence between the Fe-Kα line's shape and the phase of lfQPOs has been observed. The stellar mass black hole H1743-322 has exhibited a shifting of its Fe-Kα centroid from red to blue-shifted energies over the the ($\sim$ 5 second) cycle of an observed $\sim$ 0.2 Hz Type C QPO [37].

These theoretical and observational results motivate the following anaylsis. As described in Section 4.5, two lampposts corona are initialized, one above the disk and one below. Each lamppost is aligned with the disk configuration at a radius of $10r_g$, such that their offset from the black hole spin axis and azimuthal location are equal to the tilt and precession angle of the annulus of the disk at this distance, and located at a radial coordinate equal to $10r_g$. The lamppost co-rotates with the inner disk in the frame of a ZAMO, and emits power law radiation proportional to $dN/dE \propto E^{-(\Gamma+1)}$ with a photon index of $\Gamma = 1.7$. For this

section of the analysis, there are no emission mechanisms considered other than the emission of the lamppost itself. The Fe-Kα profiles that follow are raw (unweighted). These emission profiles at various stages of the tearing process will be evaluated, as well as the integrated line profile over the duration of the tearing event. The shift in the centroid frequency will also be examined. Fitting and spin estimation analysis are not completed here and are instead left for future work.

5.3.1 Evolving Fe-Kα Profiles

The Fe-Kα profiles produced with this co-rotating lamppost across the duration of the tearing event vary widely in their breadth, the location of their centroid, and the relative amplitude of their blue and red shifted emission. Some profiles look familiar (e.g., Figure 5.14), having higher counts in the blue shifted than red shifted emission due to Doppler beaming. The Doppler maps can also can also seem reasonable, with blue shifted emission coming from the approaching (left) side of the disk and redshifted emission coming from the receding (right) side and lensed emission from the back (see the bottom left of Figure 5.16).

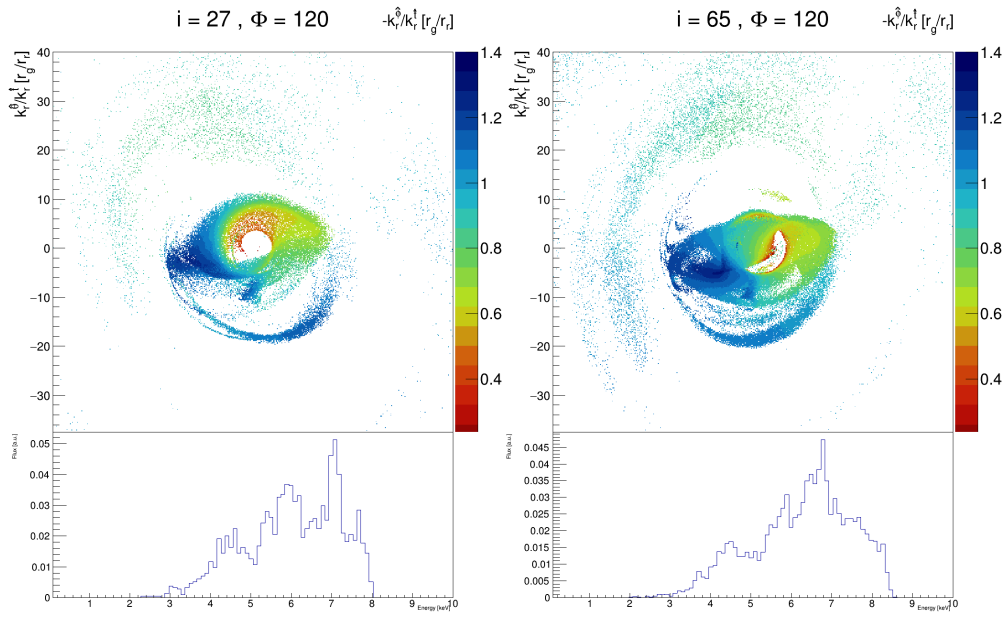

Fig. 5.14: Dopper maps and Fe-Kα line profiles for the two inclinations at the same azimuth of $\Phi = 120°$. Both are from the same time, during the precession of the inner disk. Note that the warp covering the black hole shadow is still illuminated by the lammpost, as it is aligned with the lower most blue tendril of the disk in the frame, oriented out of the page in this azimuth and moment in time.

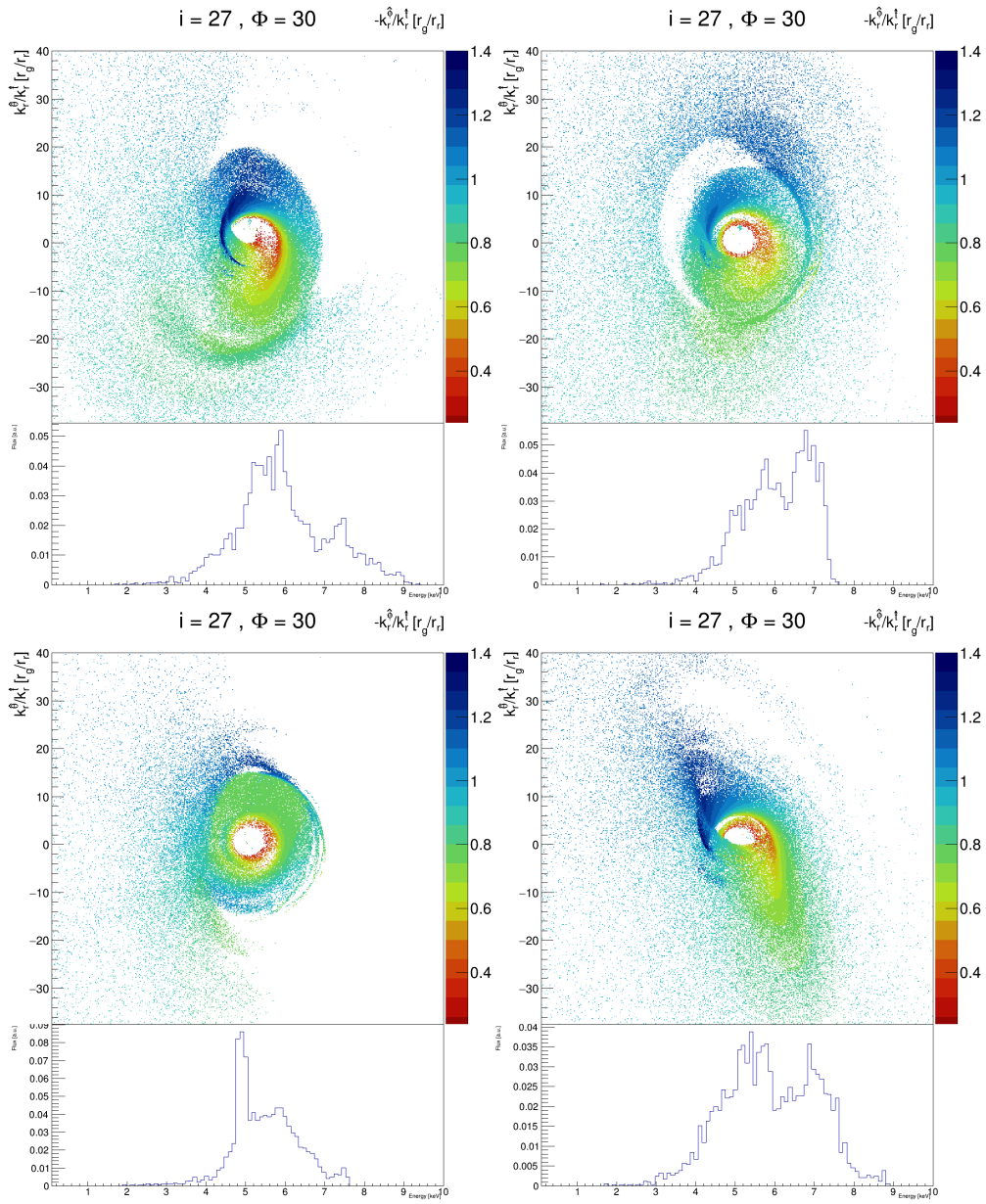

Fig. 5.15: Doppler maps and Fe-Kα line profiles for an inclination of $i = 27°$ at an azimuth of $\Phi = 30$. These figures run sequentially forward in time from left to right and top to bottom, with the top left image being just before the disk tears and the bottom right being near the end of the tearing cycle

The evolution of the system causes these emission line to vary significantly over the duration of the tearing event, with a single inclination and azimuth showing a diverse range of profiles (Figure 5.15). There are two physical mechanisms that are responsible for this variation, the first being the orbital motion of the plasma itself. The inner and outer disks precess as the system evolves, but there is additional motion in each disk due to the warps that develop. These warps lead to large θ components of momentum, skewing the Doppler profile of the disk and resulting in Fe-Kα line profiles which deviate significantly from those expected from a thin disk or even a Bardeen-Petterson aligned disk with a Keplerian profile. This effect is typical strongest at lower inclinations, where the observer's line of sight is more closely aligned with $\hat{\theta}$. The second mechanism at work here is the precession of the lamppost itself. By design it precesses with the inner disk, and thus there are configurations where parts of the outer disk may not be illuminated at all (top left and bottom left of Figure 5.15).

The detection of a chaotic Fe-Kα line like those shown above in a stellar mass black hole is not feasible with the current technology available. The full duration of this tearing event for a $10M_{\odot}$ black hole is on the order 4 wall clock seconds, and the Fe-Kα fluxes received even from the brightest sources are orders of magnitude too low to facilitate a meaningful measurement in such a short time. However, the duration of the event scales linearly with black hole mass, making the detection of an emission line during a tearing event possible for an AGN given a sensitive enough instrument. In stellar mass black holes, given long term observations of sources exhibiting hfQPOs, it may be possible to determine whether such tearing events are actually occurring via the behavior of the iron line and its integrated line profile. As will be shown in the last section of this chapter, the line profile's behavior over the course of the tearing event encodes the orbital evolution of the plasma. First, though, the integrated Fe-Kα line is examined. Raw Fe-Kα profiles are normalized in each frame

and added across all energy bins. The resulting line profiles, in some cases, look markedly different than the snapshots which compose them as shown in Figures 5.16-5.19.

Abarr and Krawczynski [100] examined the Fe-Kα lines of Keplerian disks in a Bardeen-Petterson configuration extensively. They showed that for a fixed viewing angle the location of the breaking radius and the tilt of the outer disk can have dramatic effect on the line profile, manifesting double peaks or flattening the line depending on the orientation. This is seen at various stages of the tearing event as shown above. They also observed that the centroid of the Fe-Kα line (as well as its width and shape) shift as the observer's azimuth changes for a given inclination (see Figure 5.20). For both snapshots and integrated profiles, shifting the observer orientation shifts the centroid and changes the line shape. As in the Keplerian Bardeen-Petterson case, this is attributed to the change in the boosting profile seen by different observers.

5.3.2 Shift in the Centroid frequency

For a quantitative examination of the evolution of the Fe-Kα profile, the centroid of the line is examined over the duration of the tearing event. This examination will end up bolstering the results of Section 5.2, as will be detailed at the end of this section. As mentioned previously, Ingram et al. [37] have observed a modulation of the Fe-Kα centroid over the cycle of an lfQPO in H1743-322. This further reinforces the idea that lfQPOs are due to the orbital motion of a precessing inner disk. In the data evaluated so far in this chapter, the presence of the lfQPO in the direct and reflected emission does not definitively rule out a low frequency harmonic related to $\dot{M}$ modulating the luminosity as the source of the lfQPO signal. But, if the signal is present in the reflection spectrum generated by an emitter of constant output, then the orbital motion must be (at least in part) a source of the low frequency oscillation

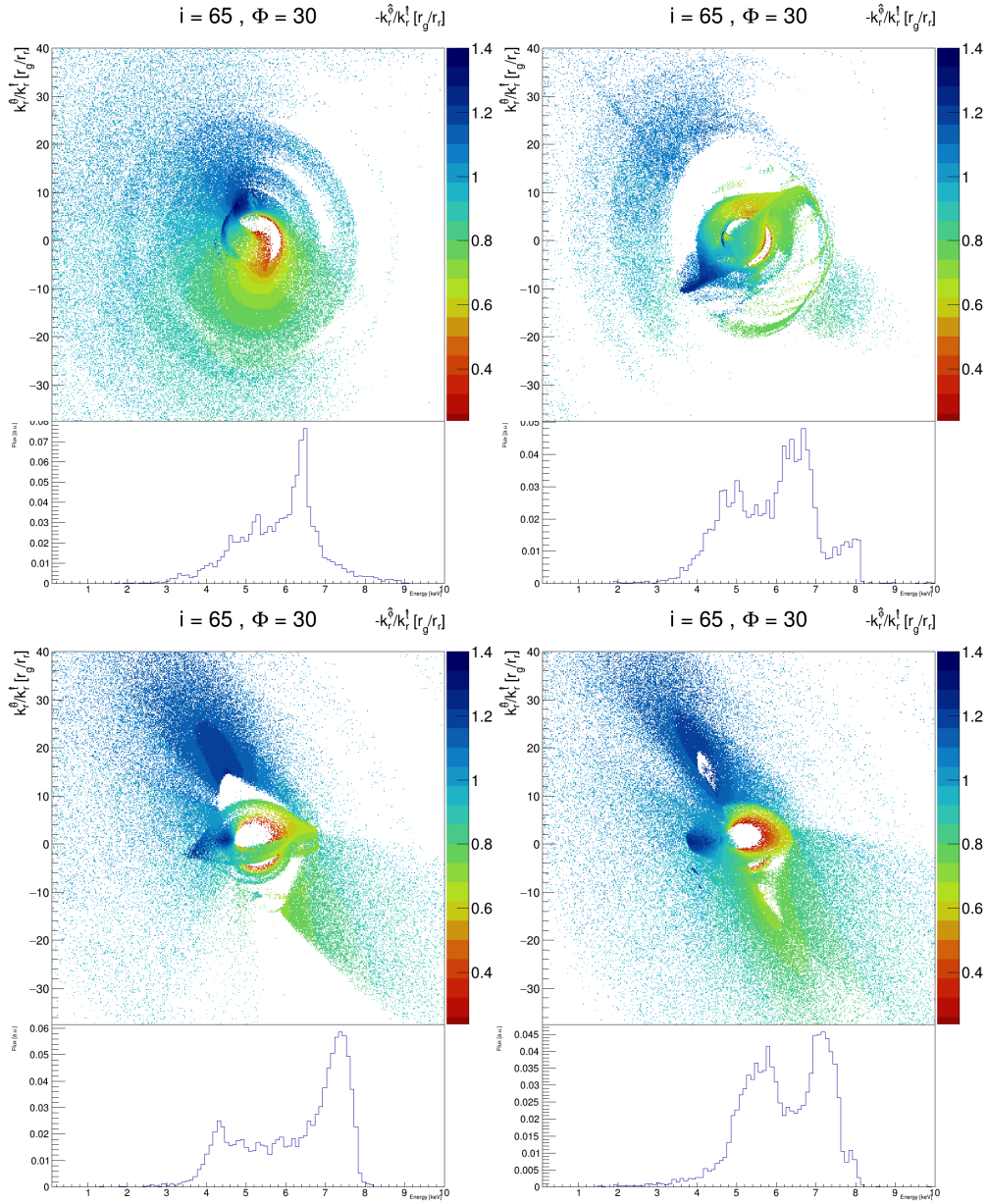

Fig. 5.16: Doppler maps and Fe-Kα line profiles for an inclination of $i = 65°$ at an azimuth of $\Phi = 30$. The frames go in sequential order from left to right and top to bottom.

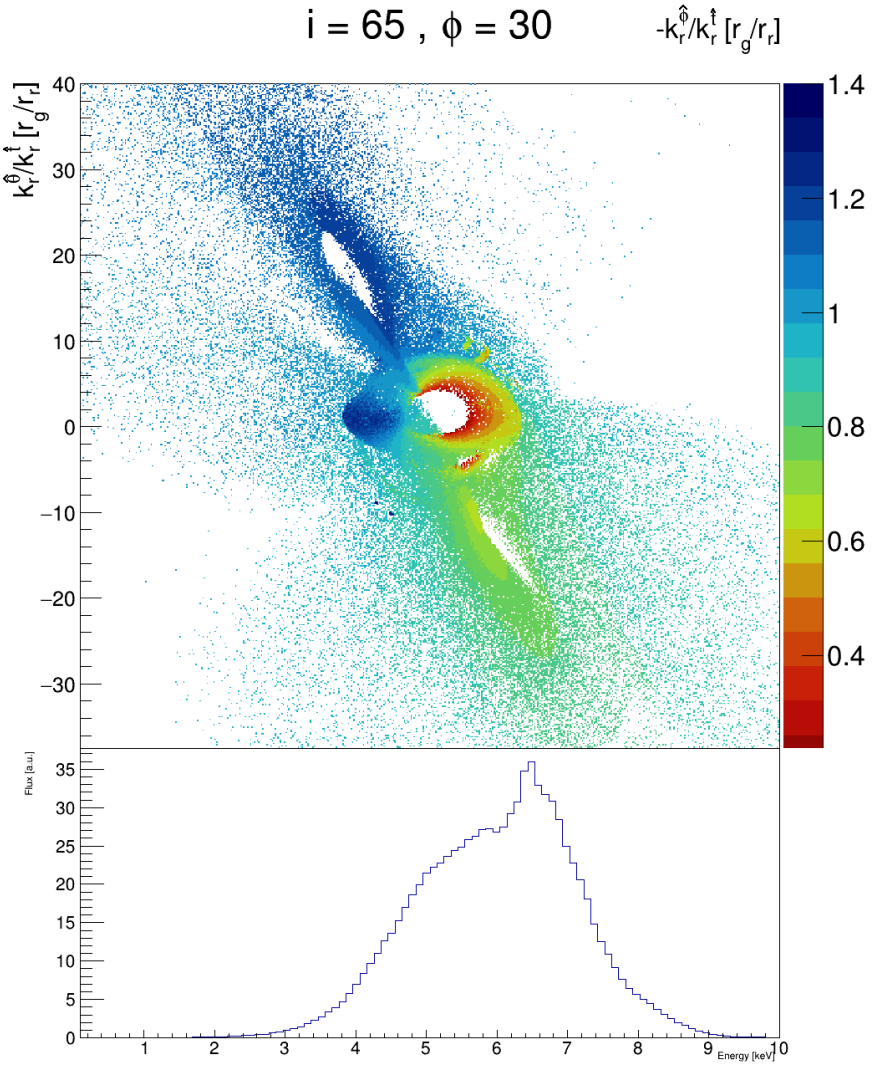

Fig. 5.17: The integrated Fe-Kα over 80% of the duration of the tearing event for an inclination of $i = 65°$ and $\Phi = 30°$. This is the integrated profile of Figure 5.16. The corresponding Doppler map shows the disk in Bardeen-Petterson configuration, and is taken $\sim 1000 r_g/c$ after the final frame of Figure 5.16.

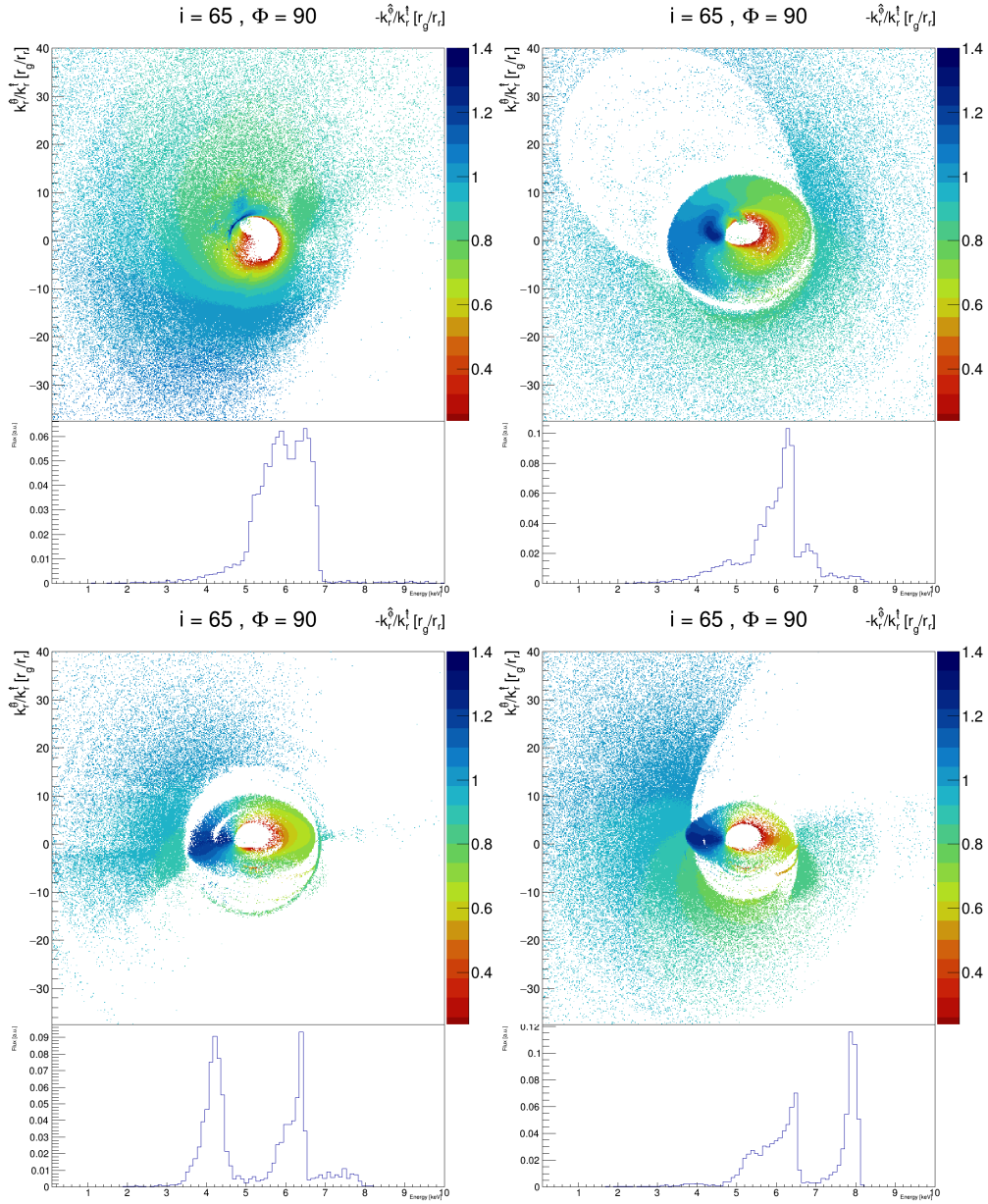

Fig. 5.18: Doppler maps and Fe-Kα line profiles for an inclination of $i = 65°$ at an azimuth of $\Phi = 90$. The frames go in sequential order from left to right and top to bottom.

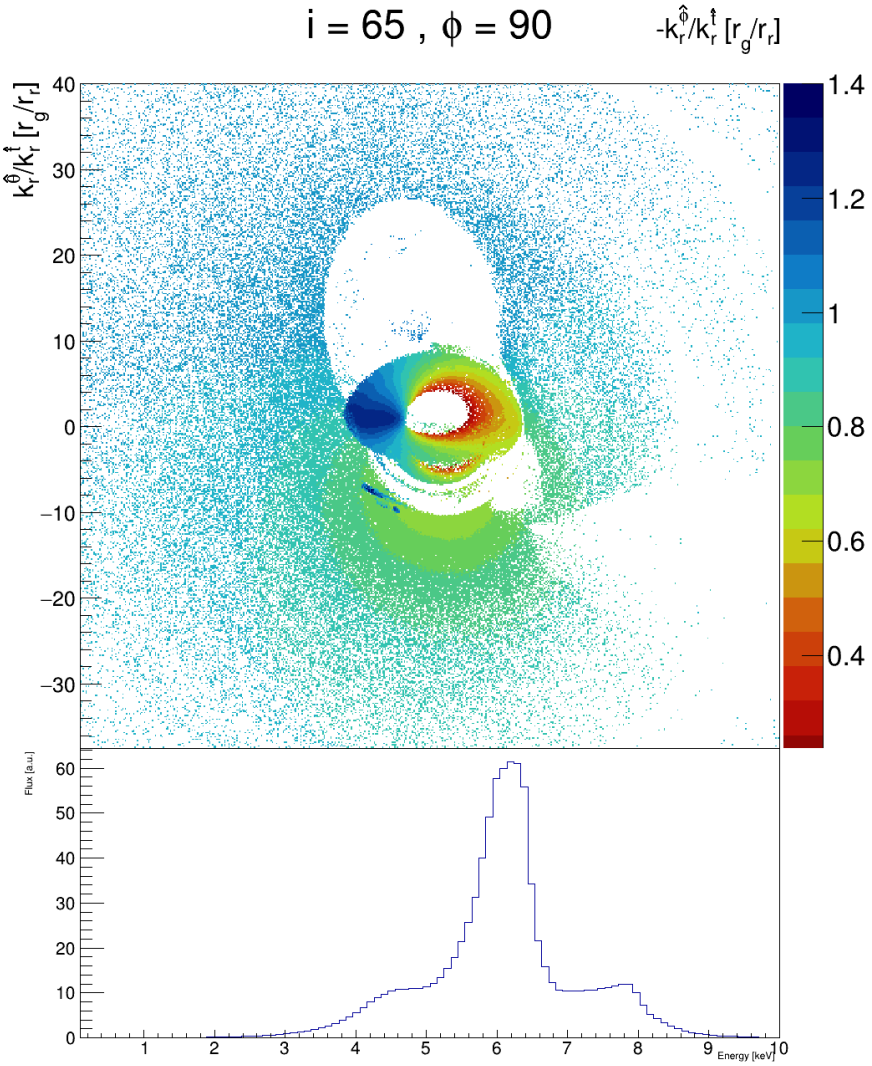

Fig. 5.19: The integrated Fe-Kα over 80% of the duration of the tearing event for an inclination of $i = 65°$ and $\Phi = 90°$. This is the integrated profile of Figure 5.18, and shows the same moment in time as Figure 5.17. The Bardeen-Petterson alignment is viewed facing the outer disk.

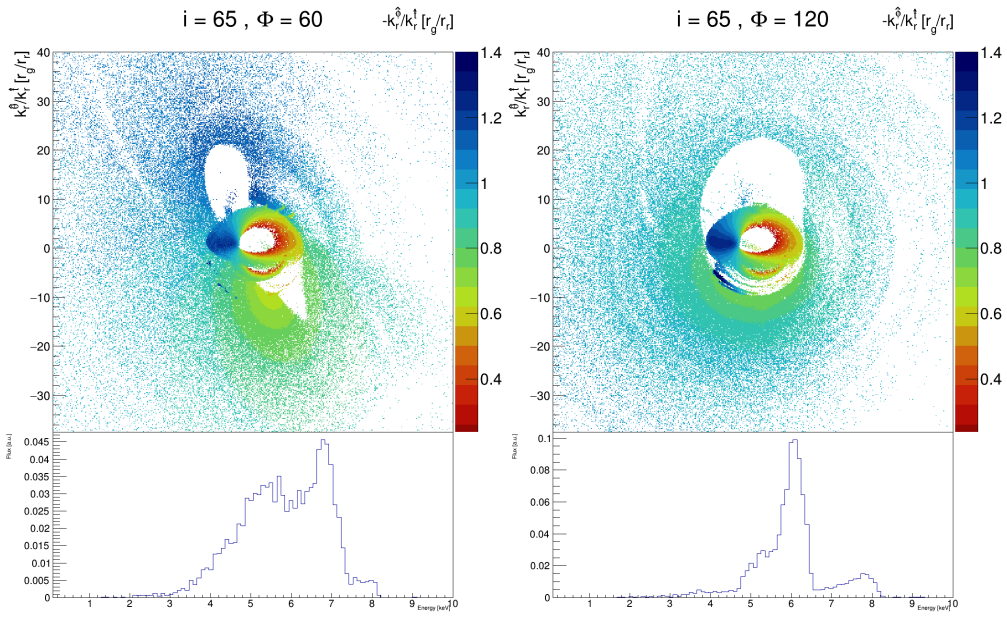

Fig. 5.20: Doppler maps and Fe-Kα line profiles for an inclination of $i = 65°$ at azimuths of $\Phi = 60°$ and $120°$ for the same moment in time (unintegrated). Here, the disk is in Bardeen-Petterson alignment. For a given breaking radius and outer disk tilt, the Fe-Kα profile changes drastically as the observer azimuth rotates at fixed inclination.

observed.

The centroid is found by first normalizing the line profile and then bin averaging the total counts per energy bin by the total counts in the line profile. The centroid evolution is shown for two inclinations and azimuths in Figure 5.21. The centroid as a function of time is then taken to Fourier space and its PSD is computed identically to the PSDs in Section 5.2.

The PSDs shown in Figures 5.22-5.24 show remarkable consistency over the two inclinations and azimuths examined. There is a broad peak in the PSD at ~ 3.5 Hz, the same frequency as the lfQPO previously observed in the thermal emission. There also appear to be peaks at 6, 8, and 10 Hz, frequencies which all correspond to Lense-Thirring precession frequencies within the precessing inner disk. These peaks remain through different averages of the FFTs in PSD computation, while the higher frequency noise shifts inconsistently. The 3.5 Hz oscillation is fit with a Lorentzian as done for previous PSDs. The fit has a quality factor of ~ 12

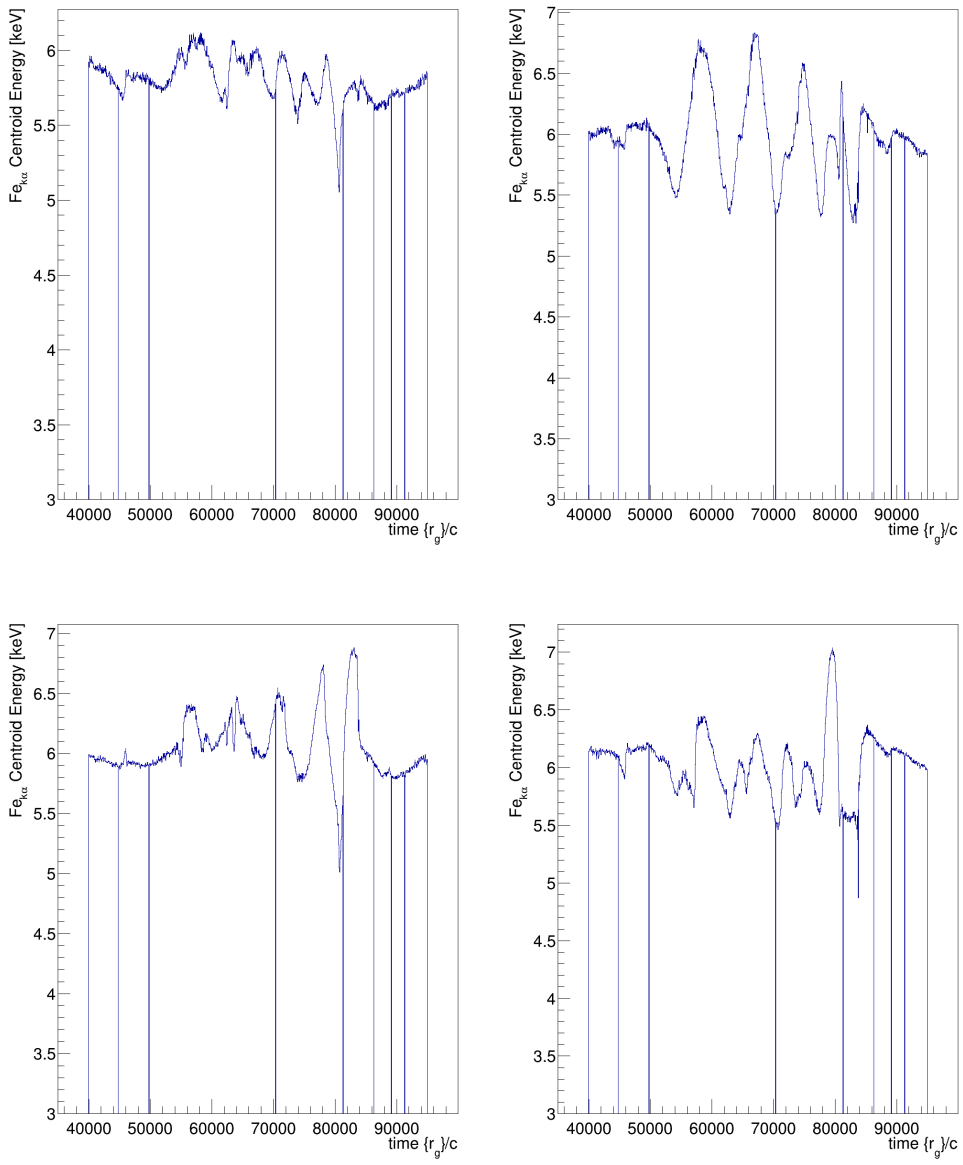

Fig. 5.21: Fe-Kα centroid over the duration of the tearing event for inclinations of $i = 25°$ (top) and 65° (bottom) and azimuths of $\Phi = 120°$ and 210°. The apparent gaps in the data are frame loss in the computation, which each correspond to $\sim 50 r_g/c$ of data loss. These losses are negligible and do not affect the result.

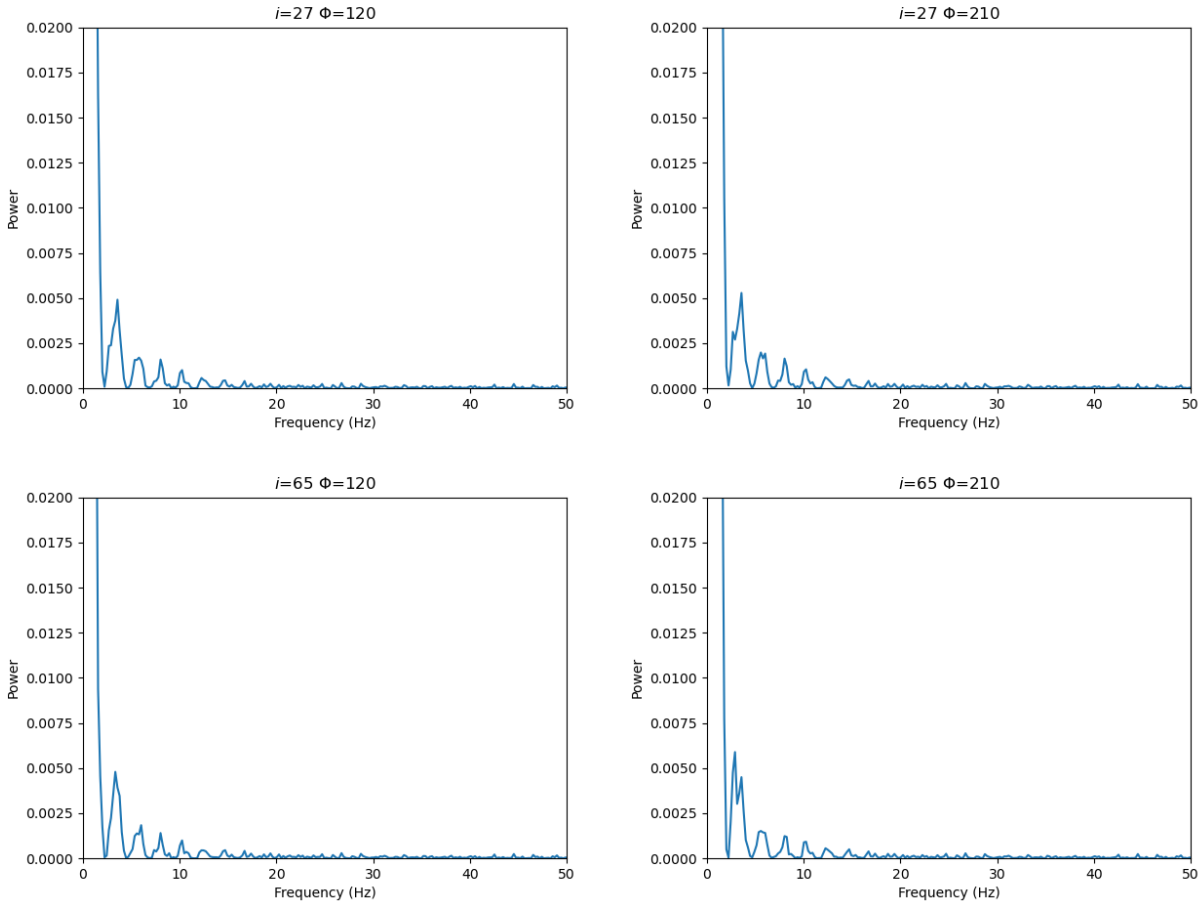

Fig. 5.22: Raw Power spectral density of the Fe-Kα centroid for the inclinations in Figure 5.21. The PSDs are highly consistent over the two inclinations and azimuths shown. There is a broad, high peak visible at all azimuths for both inclinations located at ~ 3.5 Hz, the same frequency as the lfQPO observed in the thermal emission. There are subsequent smaller oscillations at ~ 6, 8, and $10 - 11$ Hz.

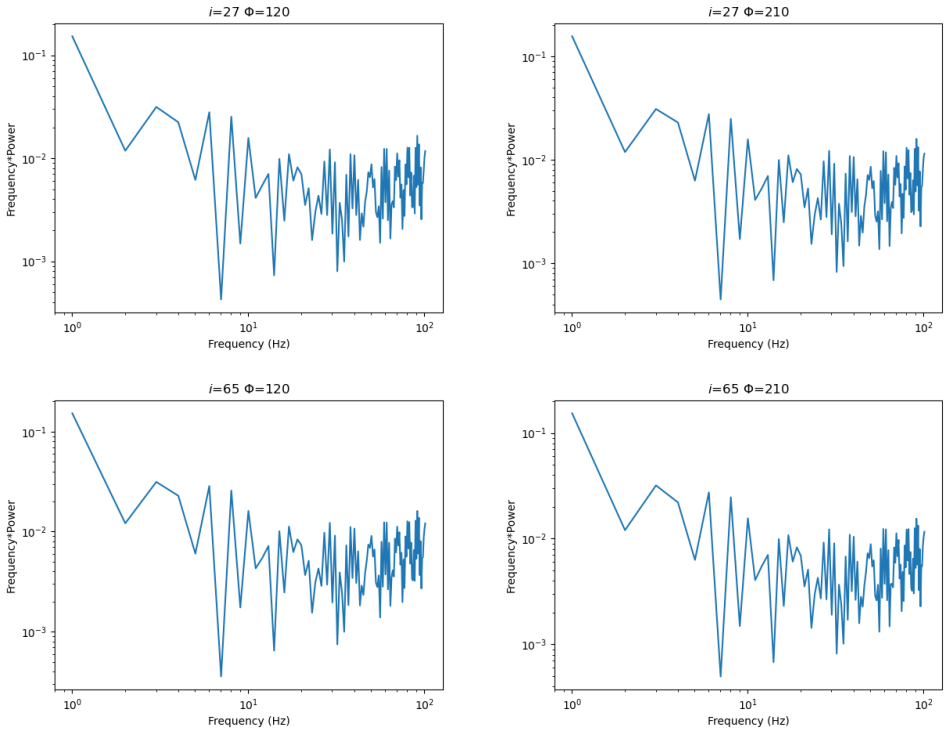

Fig. 5.23: Power spectral density of the Fe-Kα centroid for the inclinations in Figure 5.21 in log-log form with $\nu \times Power$ on the Y-axis and the X-axis extended to cover ν up to 100 Hz. The PSDs are highly consistent over the two inclinations and azimuths shown. There is a broad peak visible at all azimuths for both inclinations located at $\sim$ 3.5 Hz, the same frequency as the lfQPO observed in the thermal emission.

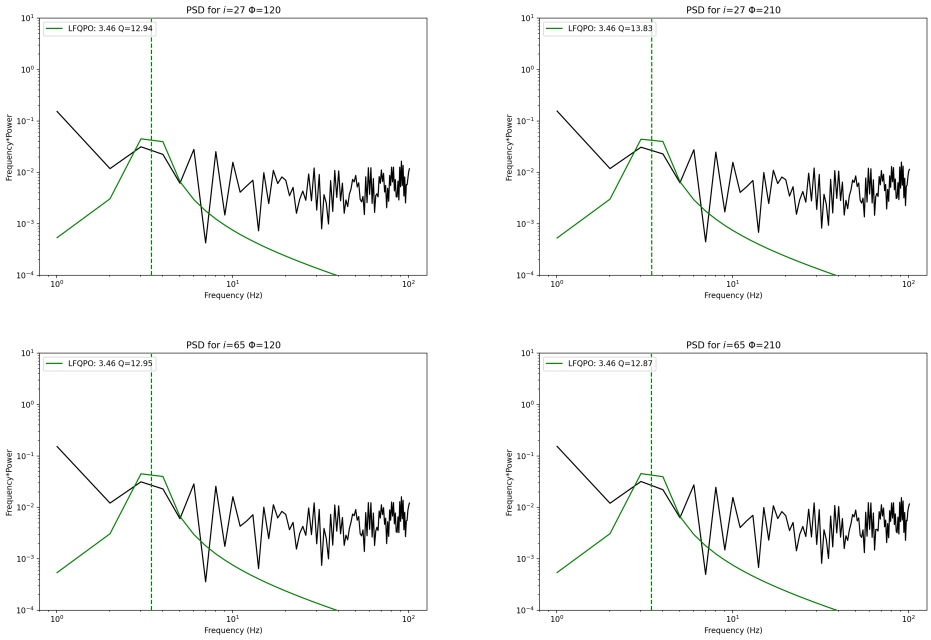

Fig. 5.24: Lorentzian fits of the Fe-Kα centroid in log-log and $\nu\times$Powser space.

5.3.3 Discussion

The orbital motion of the warped and precessing accretion disk has a strong effect on the shape of the Fe-Kα line frame by frame. Integrating this emission over the duration of the tearing event yields line profiles that can be remarkably different than those of their individual constituent frames. This tearing event has a duration of ~ 4 wall clock seconds for a $10M_{\odot}$ black hole, and as the duration scales linearly with mass, it may be possible to detect misalignment and warps spectroscopically in AGN. In the case of stellar mass black holes, discerning these events with line profiles alone is next to impossible given the low fluxes and long integration times required. But, long duration observations of known hfQPO emitters allow for time domain analysis of the shift in the Fe-Kα centroid frequency as has been completed by Ingram et al [37]. This work shows that modulation in the Fe-Kα centroid can occur from the precession of the inner disk and occurs at the frequency of the lfQPO induced by this precession, which is approximately the Lense-Thirring precession frequency of the outer edge of the precessing disk. The coronal emission modeled here is of constant output over the duration of the precession cycle and in the frame of a ZAMO it emits without boosts to increase/decrease reflection from the disk. showing that modulations in $\dot{M}$ and thus in L are not required for the production of lfQPOs.

5.4 Thermal Emission and Polarization

As was shown in Chapter 2, deviations from the thin disk model can have strong impact on the polarization spectra of the thermal emission of accreting stellar mass black holes. As the geometric thickness increases, so too does the measured polarization degree and angle. Abarr and Krawczynski [99] have examined the polarization spectra of geometrically thin accretion disks in Bardeen-Petterson alignment. Their results show that while at low

energies (in the outer, misaligned disk) the polarization degree and angle match that of a thin disk, at high energies the degree is typically lower. Further, the polarization angle exhibits dynamic behavior depending on the viewing angle, with it matching the thin disk case when the observer orientation is such that there is no apparent rotation between the angular momentum vectors of the inner and outer disks and being offset by the rotation angle for all other observers.

Ingram et al [132] have shown that Lense-Thirring precession of the inner disk in stellar mass black holes is expected to modulate the polarization degree and angle on a frequency equal to the QPO frequency induced by the precesesion. They find higher RMS modulation of the polarization degree and a lower modulation of the angle as the inclination of the observer increases. The analysis that follows examines the polarization degree and angle of the thermal emission from the accretion disk at various times during the course of the tearing event, as well as their behavior over the full duration of the tearing event. An analysis is presented on the modulation of the polarization degree and angle as it relates to the hfQPO and lfQPO observed in the thermal emission.

5.4.1 Polarization Degree and Angle During Precession and Bardeen-Petterson Alignment

Like the Fe-Kα line shown above, the polarization degree and angle show significant variation for a given inclination and azimuth over the duration of the tearing event. There are two physical mechanisms driving these variations. Firstly, the orbital motion of the disk as the inner and outer disks precess at different rates affects the boosting profile and lensed emission towards the observer. As described in Chapter 2, increased boosting towards the observer can effectively lower the polarization of the emission, while increased boosting away from the

observer can raise the polarization. Lensing acts to rotate the polarization vector. A second effect is that of the disk geometry. As the inner and outer disks warp and precess relative to one another the polarization is expected to change based on the amount of scattering occuring. This increased surface area available for scattering is the driving force of the increased polarization observed in the slim disks discussed in Chapter 2. The concavity (or convexity) of the disk increases (or decreases) the amount of scattering occuring.

The following figures will show disk images with polarization overlaid and the polarization degree and angle as functions of energy for the two inclinations. The plots will look at three distinct times during the tearing event. $t \simeq 50,000 r_g/c$ is shortly after the tearing event starts and the inner disk is differentially precessing and out of alignment. $t \simeq 70,000 r_g/c$ is more than half way through the event and there are two distinct inner sub-disks, one that is precessing and one that is in Bardeen-Petterson alignment. Finally, $t \simeq 80,000 r_g/c$ is a period of Bardeen-Petterson alignment shortly before the inner disk is accreted away and the entire misaligned disk reforms.

Figures 5.25 - 5.26 show the disk when the inner region is misaligned and precessing. At $i = 27°$, the high energy emission from the inner-most regions of the flow is highly polarized, while its angle is nearly horizontal. The section of the image above the black hole's shadow is the far side of the inner disk warped away from the observer, and the section below the black hole shadow is warped out of the page towards the observer. The high polarization above and low polarization below in the image is due to this geometry. At an inclination of $i = 65°$ the observer's line of sight is nearly aligned with the edge of the outer disk, obscuring the inner regions and lowering the polarization.

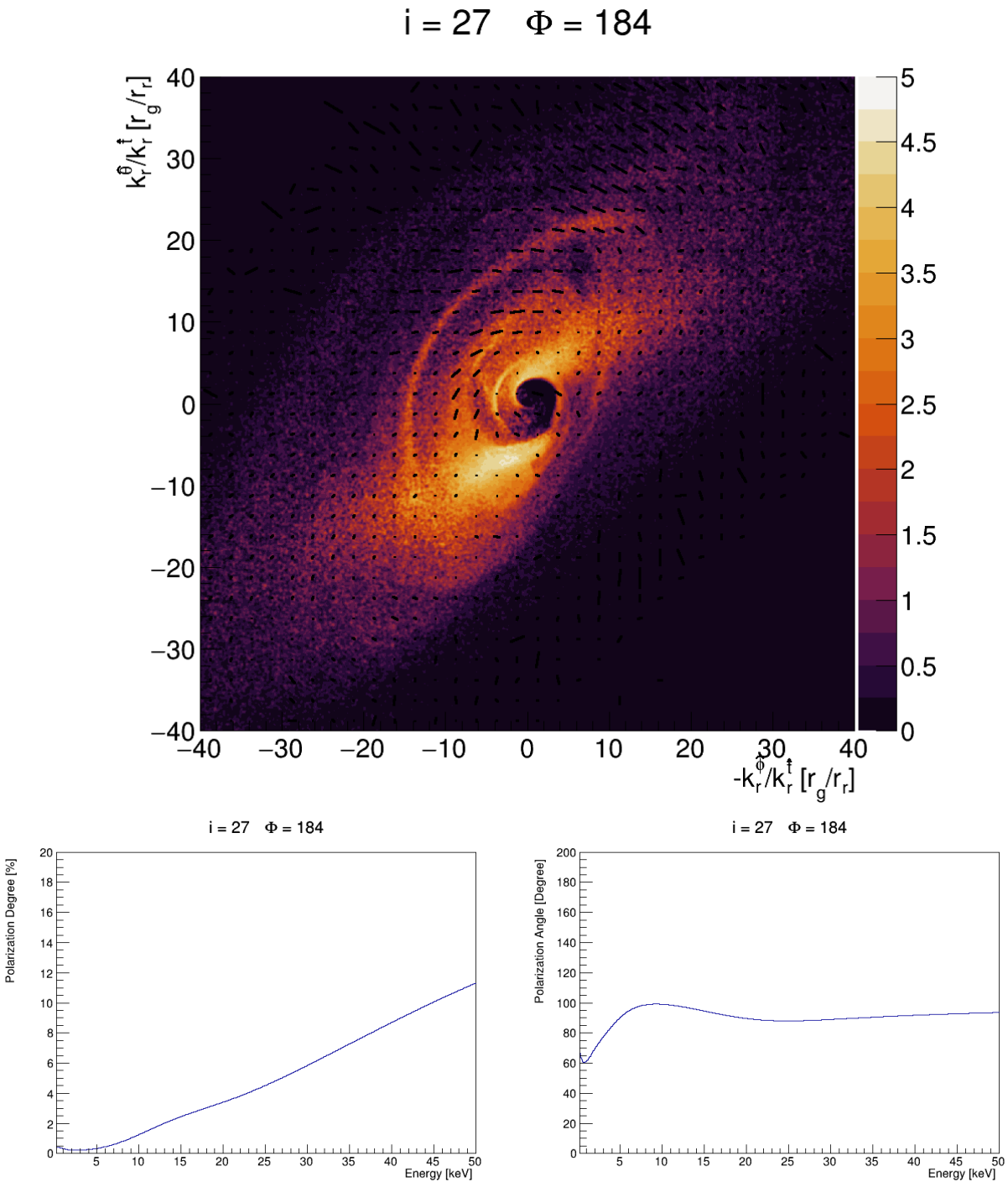

Fig. 5.25: Disk image, polarization degree and polarization angle for an inclination of $i = 27°$ and an azimuth of $\Phi = 184°$ at a time shortly after the tearing event begins, $t \simeq 50,000 r_g/c$. Here the inner disk is misaligned and precessing.

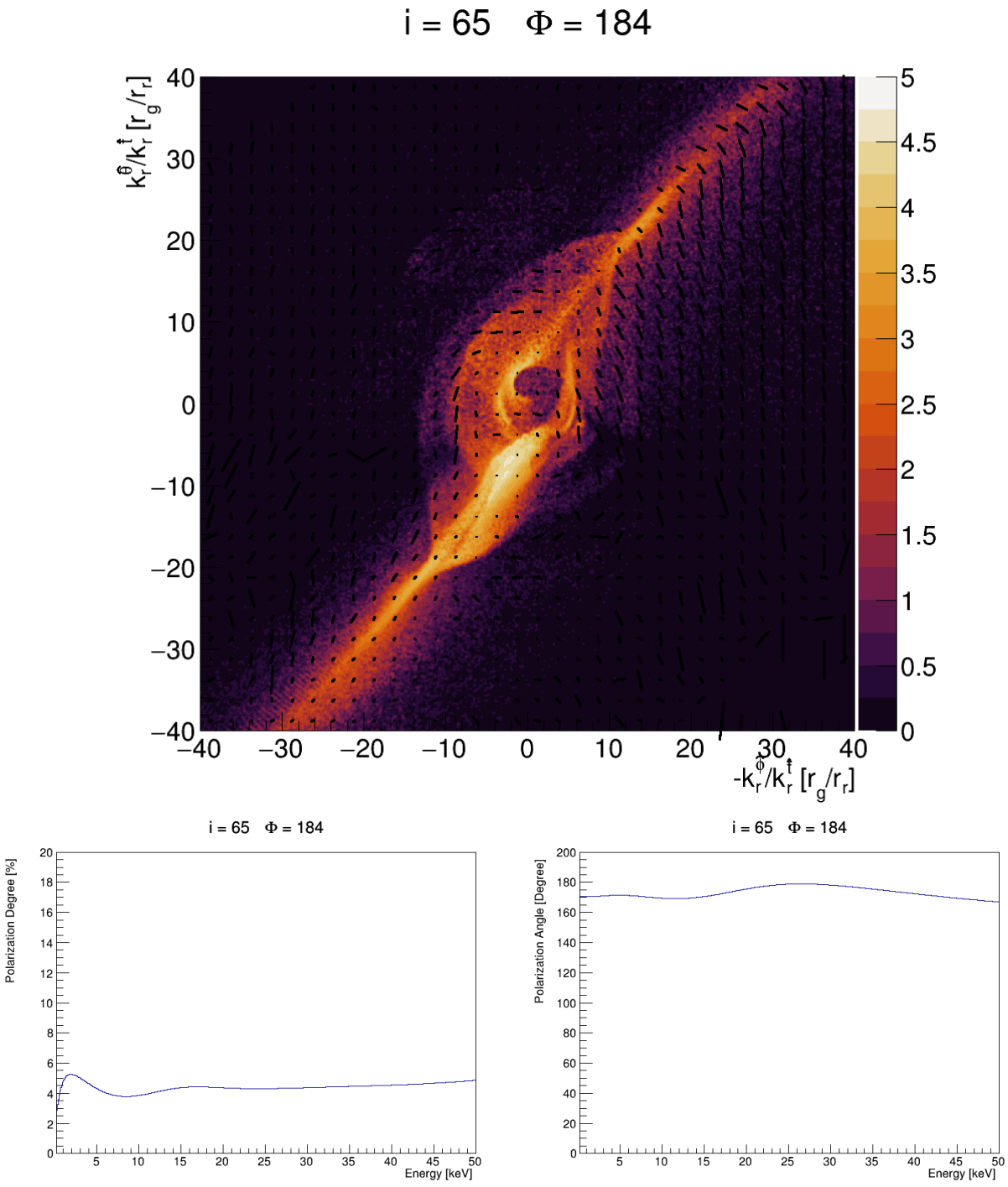

Fig. 5.26: Disk image, polarization degree and polarization angle for an inclination of $i = 65°$ and an azimuth of $\Phi = 184°$ at a time shortly after the tearing event begins, $t \simeq 50,000 r_g/c$. Here the inner disk is misaligned and precessing.

In Figures 5.27 - 5.28 there are two inner sub-disks, the inner-most disk is Bardeen-Petterson aligned and the other is still precessing. These two inner sub-disks are not disconnected from each other as the inner disk system is from the outer disk, but are connected by a smooth warp. At $i = 27°$, the inner, hot disk is unobscured and the polarization angle is nearly aligned with the black hole spin in this inner region. As shown in Section 5.3, θ components of momentum have a stronger effect at this low inclination, lowering the polarization at high energies compared to $i = 65°$. At this higher inclination, the polarization is a factor ~ 3 higher.

Figures 5.29 - 5.30 show the disk in Bardeen-Petterson alignment near the end of the tearing cycle. At this azimuth the observer can see the face of the outer and inner disks clearly. At all energies the polarization is approximately orthogonal to the black hole spin, while the polarization degree peaks near the middle to outer region of the inner disk. At $i = 65°$ the observer sees more reflection from the inner disk off of the outer disk. Here, the polarization pattern on the map in the inner regions where the orbit of the plasma is roughly Kerplerian approximately follows that of a thin disk. Boosted emission (left side) is depolarized and emission from the receding edge has higher polarization. The polarization angle in outer disk also matches well the results of Abarr and Krawczynski (see Figure 2 in [99]).

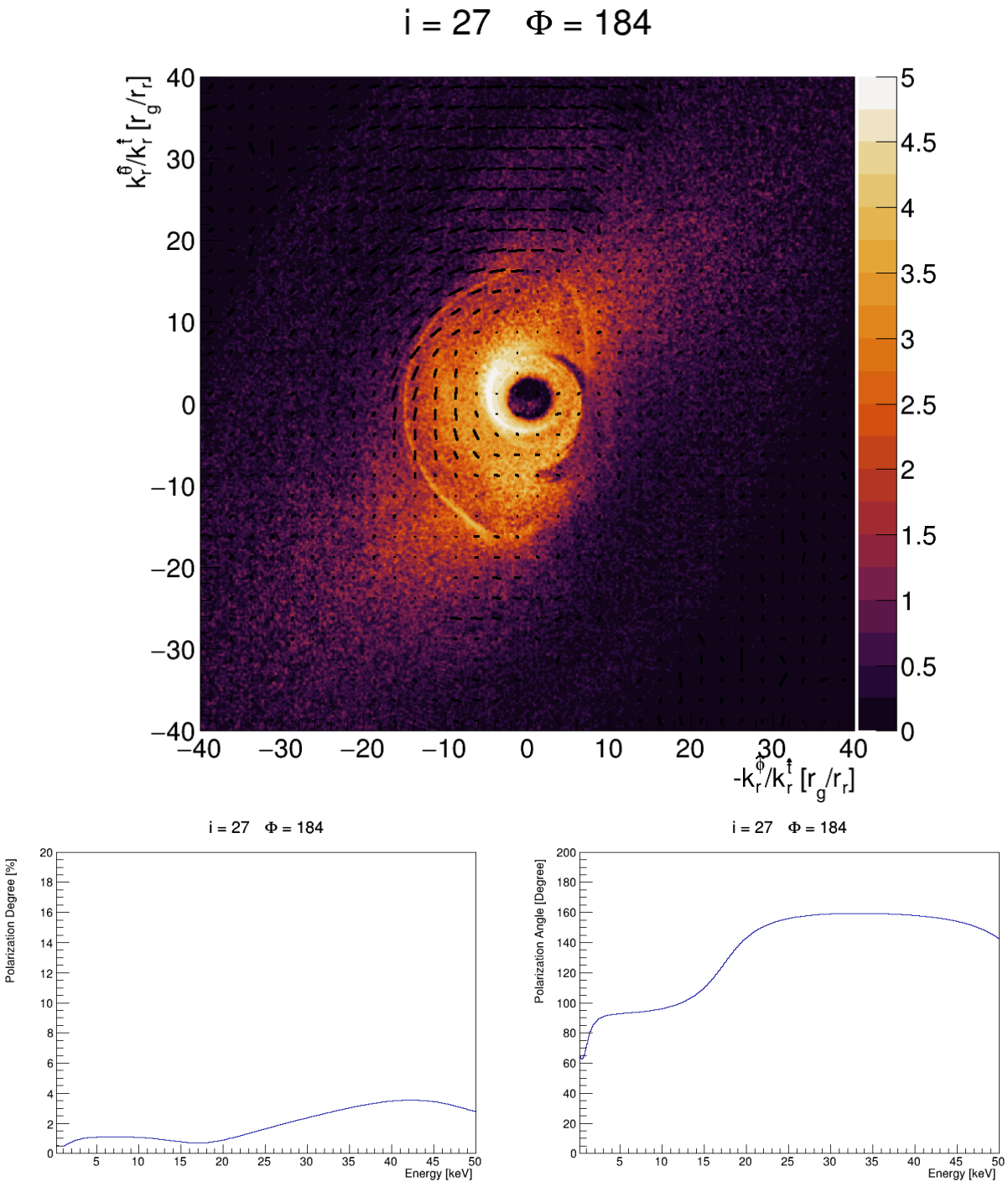

Fig. 5.27: Disk image, polarization degree, and polarization angle for $i = 27°$ and $\Phi = 184°$ at $t \simeq 70,000 r_g/c$. The innermost disk is in Bardeen-Petterson alignment, and the second inner disk is precessing..

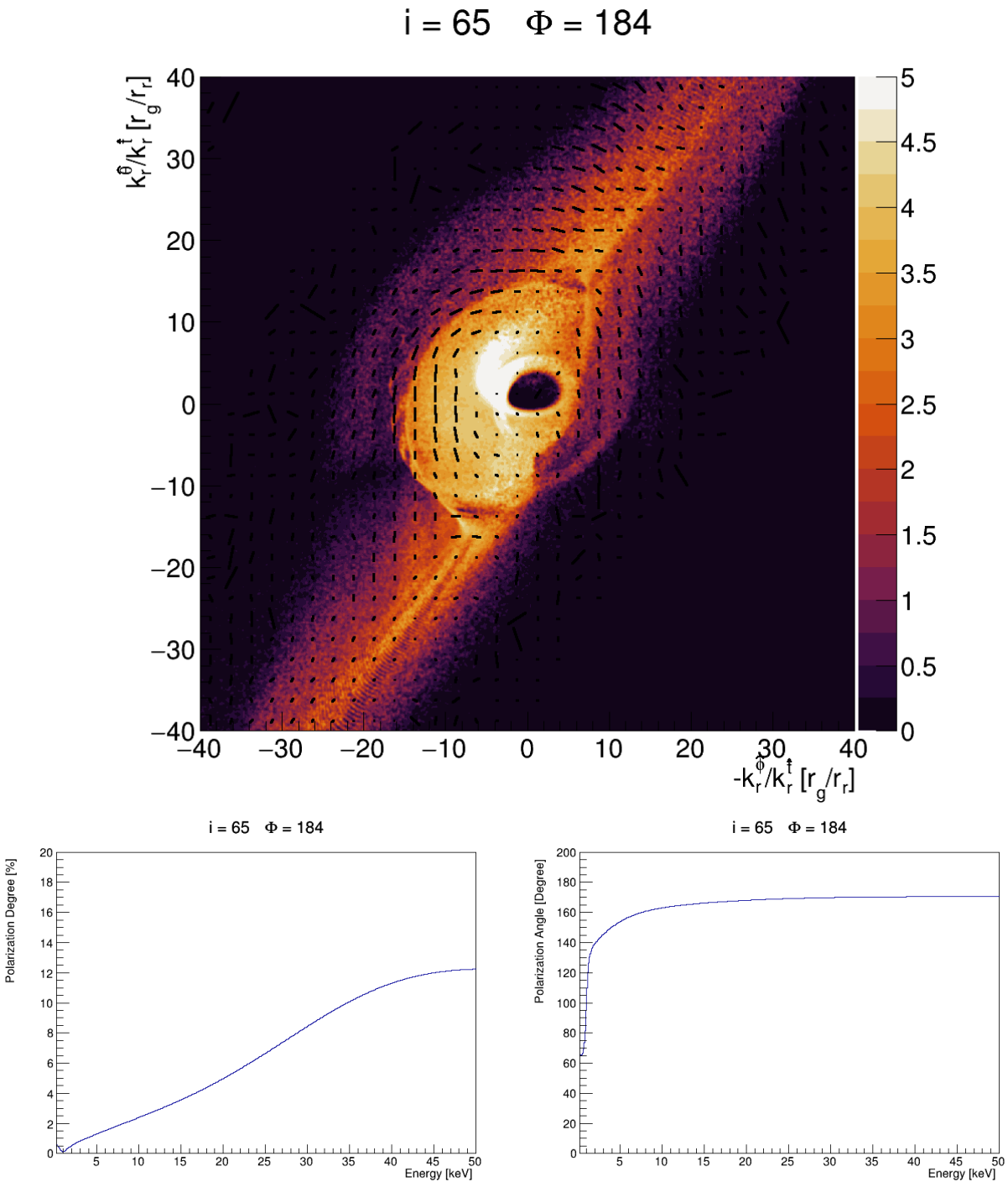

Fig. 5.28: Disk image, polarization degree, and polarization angle for $i = 65°$ and $\Phi = 184°$ at $t \simeq 70,000 r_g/c$. Here there are two inner sub-disks. The innermost disk is in Bardeen-Petterson alignment, and the second inner disk is precessing.

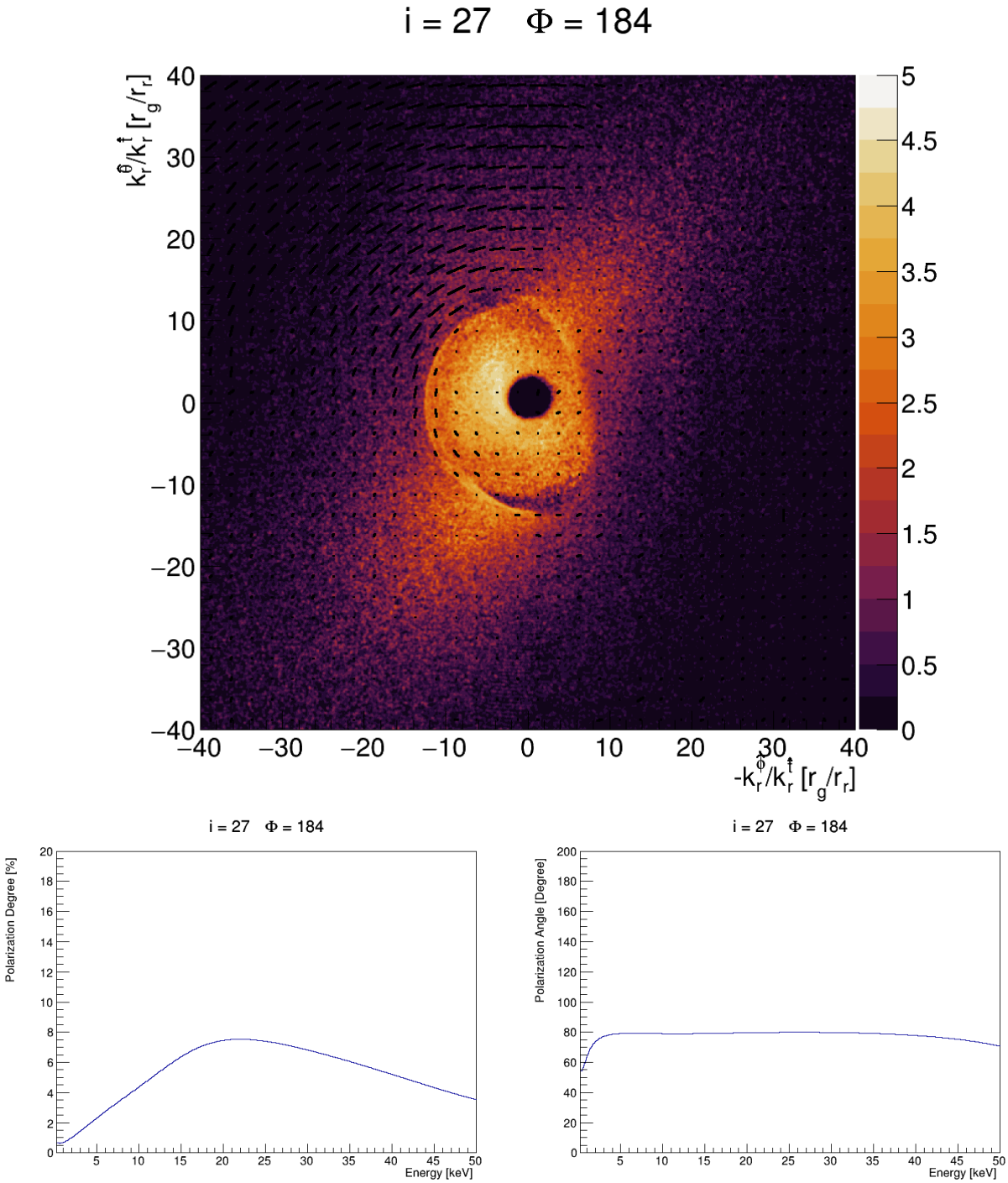

Fig. 5.29: Disk image, polarization degree, and polarization angle for $i = 65°$ and $\Phi = 184°$ at $t \simeq 80,000 r_g/c$. Here the disk is in Bardeen-Petterson alignment.

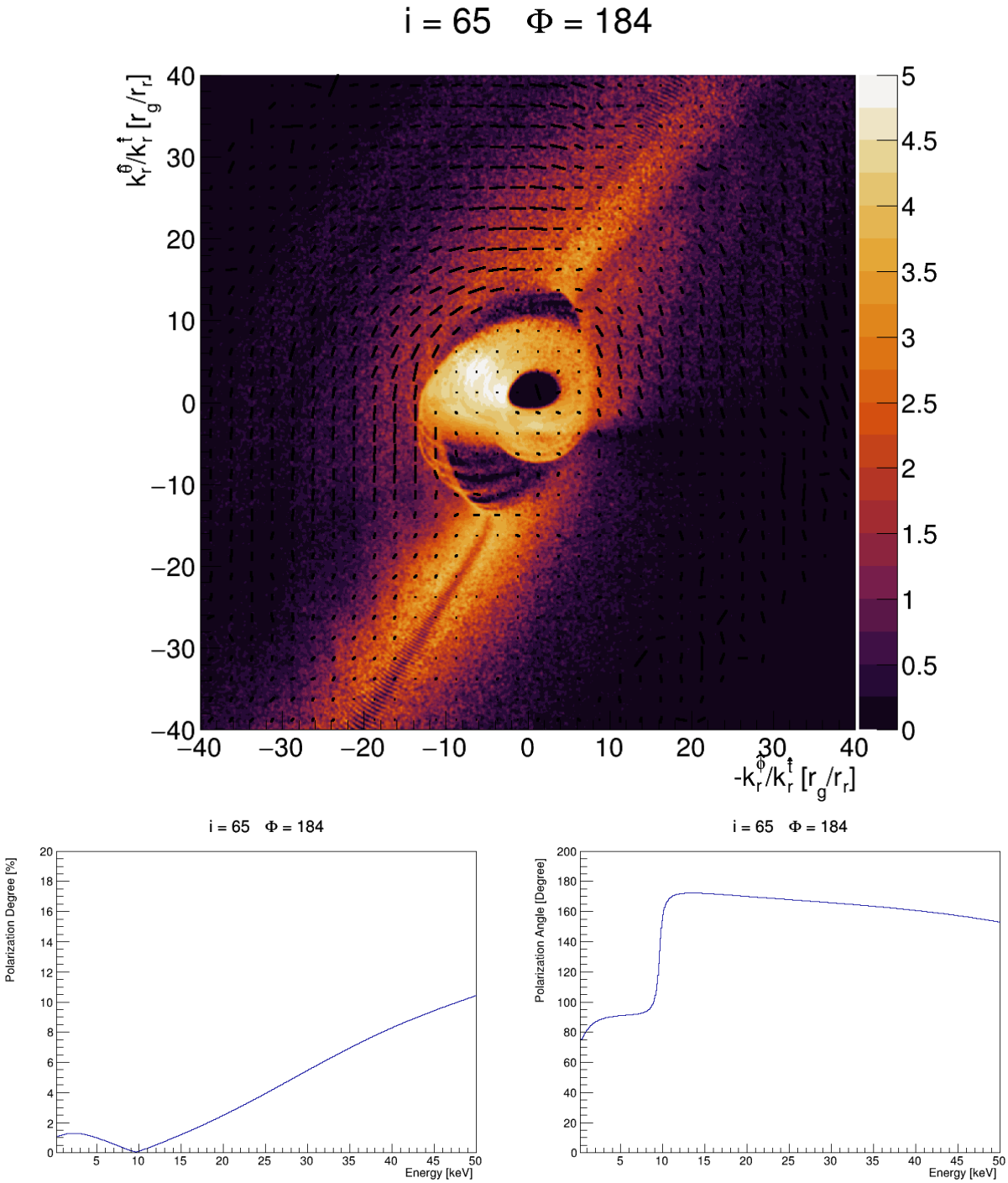

Fig. 5.30: Disk image, polarization degree, and polarization angle for $i = 65°$ and $\Phi = 184°$ at $t \simeq 80,000 r_g/c$. Here the disk is in Bardeen-Petterson alignment.

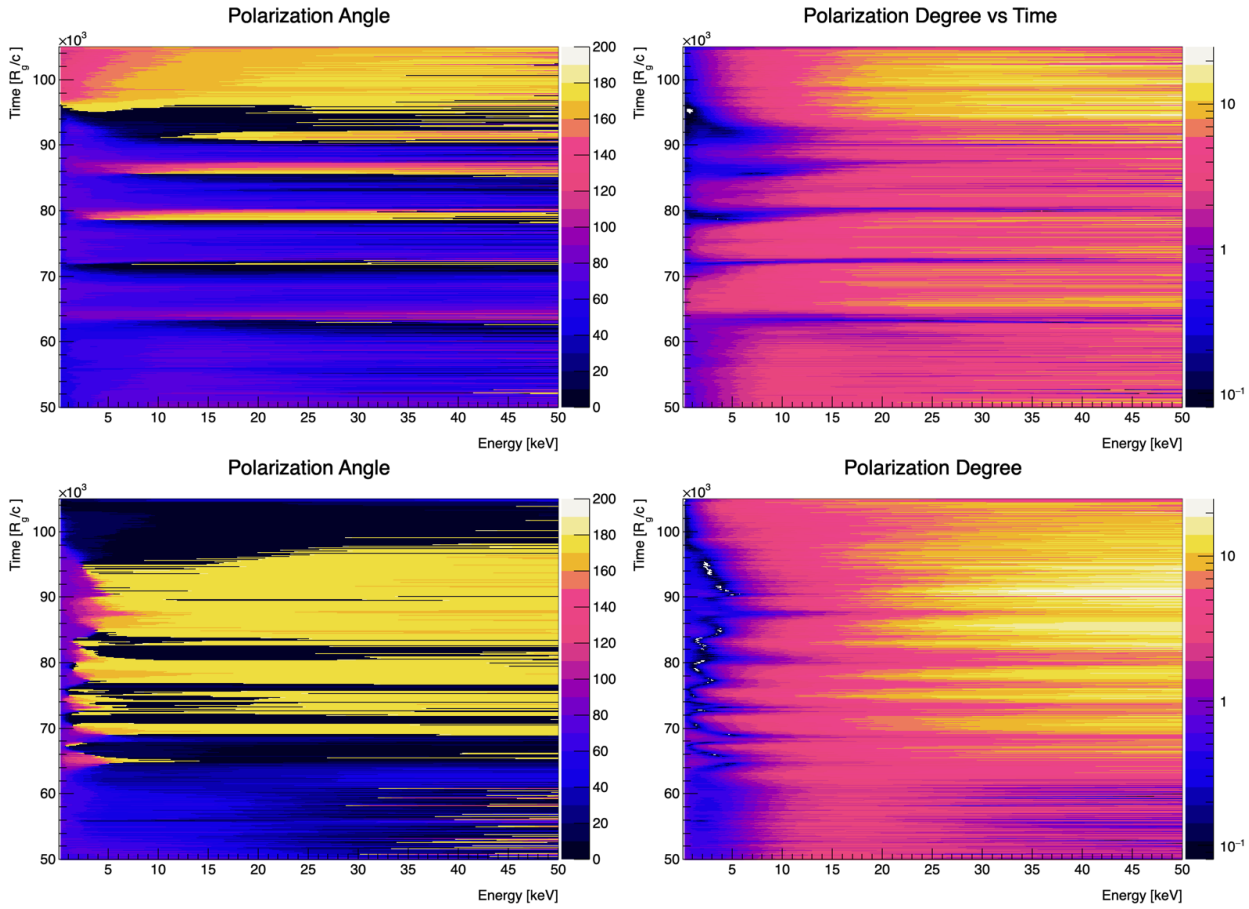

Fig. 5.31: Maps of Polarization angle (right) and degree (left) for inclinations of $i = 27°$ (top) and $i = 65°$ (bottom) at an azimuth of $\Phi = 124°$.

Over this brief selection of the data the polarization angle and degree are diverse both between different frames at a fixed inclination and between inclinations at a fixed frame. In order to evaluate the the behavior more efficiently, maps have been constructed showing the polarization degree and angle as functions of energy and time for different observers (Figures 5.31 - 5.32). There is an apparent periodicity in both the polarization angle and degree at low inclinations. At high inclinations, the periodicity in the polarization angle smooths out (note that 180° and 0° are the same polarization angle) while the pattern in the polarization degree grows stronger.

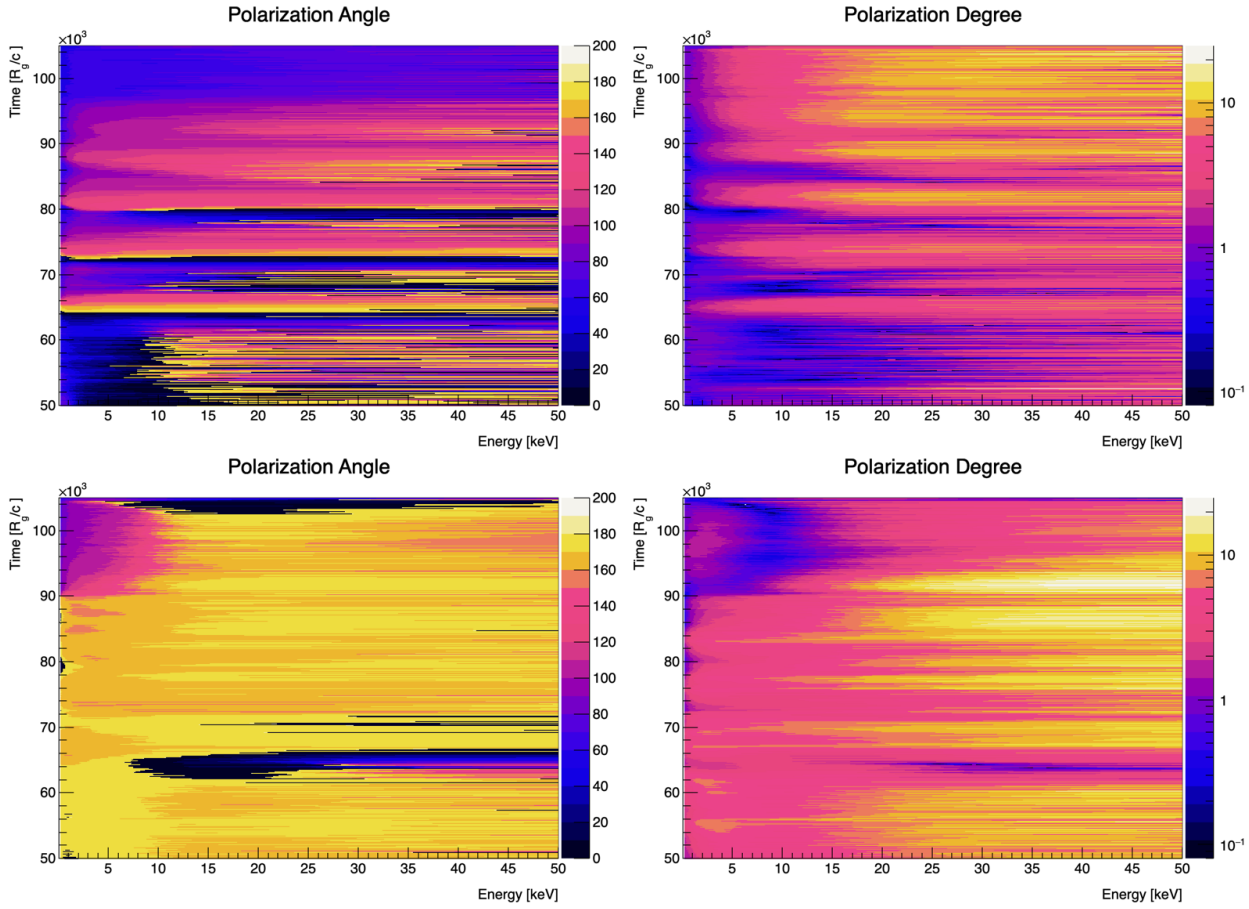

Fig. 5.32: Maps of Polarization angle (right) and degree (left) for inclinations of $i = 27°$ (top) and $i = 65°$ (bottom) at an azimuth of $\Phi = 214°$.

In order to quantify this periodicity, the signals are taken to Fourier space where their power spectral density is computed. Considered here are polarization degrees and angles corresponding to energies of $20 \leq E_{obs} \leq 30$ keV. These signals are averaged and Fourier transformed and the PSDs computed identically to the preceding analysis. Evaluating the PSD shows a low frequency oscillation in both the polarization degree and angle occurring between $\sim 2 \leq \nu \leq 4$ Hz, corresponding to the Lense-Thirring precession frequency in the outer edge of the inner disk. This analysis is recent, and considering the errors on the polarization degree and angle noted in Section 4.6, requires further examination. But the result, if verified, would not be surprising given the signals found in the thermal emission and Fe-Kα line.

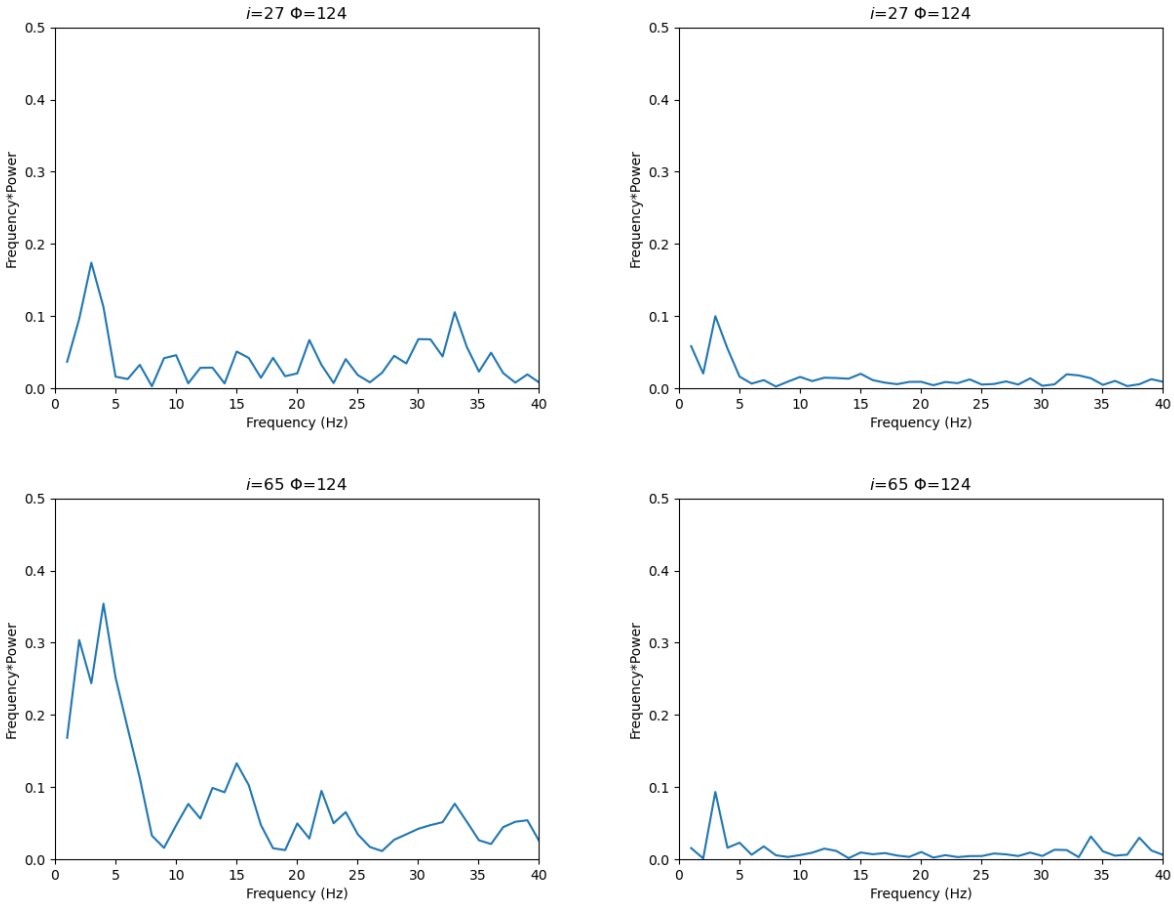

Fig. 5.33: Raw power spectral density for polarization angle (right) and degree (left) for inclinations of $i = 27°$ (top) and $i = 65°$ (bottom) at an azimuth of $\Phi = 124°$.

5.4.2 Discussion

The non-Keplerian velocity profile of the disk, its dynamical and highly variable geometry, and its emission profile all have a strong impact on the polarization signatures observed. From the velocity profile, blue (red) shifting increases (decreases) the polarization degree in areas of where the velocity of the disk is large and approaching (receding from) the observer. The velocity profile in this warped and precessing disk shifts this polarization pattern from the areas of the disk that would be approaching (receding from) the observer in the Keplerian, equatorially aligned case. The warped geometry itself can increase (decrease) the polarization from scattering in the convex (concave) regions of of the disk. The precession also has an effect as the inner disk, the source of high energy highly polarized emission, is shadowed by the outer disk. In all, these effects combine to create dynamic signals in the polarization degree and angle. Plotting these signals over the duration of the tearing event reveals episodic variability in both, which when taken to Fourier space reveal oscillations with a frequency matching that of the Lense-Thirring precession of the inner disk. These are new results, and higher fidelity simulations which will yield reduced statistical errors are in progress and will be described in a forthcoming publication.

Chapter 6

Summary and Future Outlook

This thesis has detailed work I have completed on modeling the X-ray emission from black hole accretion disks that deviate from the standard thin disk model. Chapter 2 showed the polarization of slim accretion disks, which are expected to arise at accretion rates exceeding $\sim 30\%$ of the Eddington limit where thermal pressures build as matter infalls towards the black hole faster than it can efficiently radiate away its thermal energy. My results showed that as the thickness of the disk increases, so too does the polarization degree and angle.

Chapter 3 reviewed the GRMHD code *H-AMR* and examined the data set of a highly inclined, thin accretion disk undergoing tearing events. The dynamics of the disk during these tearing cycles were reviewed in detail. This data set serves as the foundation for the work that follows in Chapter 5. Chapter 4 detailed the development of a General Relativistic raytracing code used to read in the data from *H-AMR* and post process its emitted radiation. Care was taken to outline the subtle details of the code and the theoretical framework on which it is built. The code was compared against the standard thin disk in Boyer-Linquist coordinates for thermal emission and using an axially aligned lamppost. In this comparison, errors in the calculation of the polarization degree and angle were noted and possible sources of the error were identified. Minimizing these errors is a high priority for future work, but their presence does not undermine the validity of the results shown in Sections 5.2 and 5.3.

Chapter 5 showed the results of raytracing the GRMHD data set of Chapter 3. Section 5.2 showed that a 55 Hz oscillation in $\dot{M}_r$ at the tearing radius translated into a 57 Hz high frequency quasi-periodic oscillation in the thermal emission from the disk. This hfQPO was accompanied by a 2 : 1 harmonic at 115 Hz for some observers. There was an additional 89 Hz signal at a 3 : 2 ratio to the hfQPO fundamental frequency, which upon evaluating the bolometric lightcurve in Fourier space seems to in fact be the first harmonic of a slightly lower frequency (44 Hz) hfQPO emanating from the inner edge of the outer disk during the tearing cycle. This 44 Hz hfQPO signal, if it is indeed the source of the 89 Hz signal, is somehow washed out in the observer lightcurves. Determining the robustness of this particular conclusion is an ongoing effort. There was an additional low frequency QPO found in the data at $\sim$ 3 Hz, corresponding to the Lense-Thirring precession frequency at $10r_g$. This signal and the fundamental hfQPO signal at 57 Hz are visible to all observer inclinations and azimuths.

Next, the Fe-Kα line from a co-roating lamppost was examined. The diversity of line profiles was explored in some detail, as well as the integrated total of these profiles over the course of the tearing event for a variety of azimuths across two observer inclinations. The variety of Fe-Kα line profiles spurred an exploration of the behavior of the line centroid, which when taken to Fourier space revealed the presence of an lfQPO at $\sim$ 3Hz caused by the precession of the inner disk. This result shows that an lfQPO signal can be due solely to precession, no modulation of the accretion rate and/or luminosity is required, further substantiating long held theories on the possible origin of these signals. Finally, the polarization signals from this evolving disk structure were examined. These signals - like the Fe-Kα line - show a diversity of behaviors across different azimuths and inclinations. At a few carefully chosen frames, the results agree to an extent with previous work on the polarization signals from Keplerian disks in Bardeen-Petterson alignment [99]. Maps were

made of the polarization angle and degree, revealing an apparent periodicity in each signal. The signals were then brought to Fourier space where low frequency $\sim 2-4$ Hz oscillations were found in each. This analysis is new, and simulations with much higher resolution and lower statistical errors are in currently in progress to verify this result.

There are some shortcomings to this work, the most notable of which is the discrepancy in the polarization spectra between the thin disk in Boyer-Lindquist coordinates and that in Kerr-Schild. Reducing the statistical errors to bring these results into alignment is of high priority moving forward. This notwithstanding, these results lay the groundwork for a litany of exciting future projects. One of which I am most excited about, and which stands to have a meaningful impact on the field, is the incorporation of data from the two-temperature, fully radiative version of *H-AMR* which recently began running. Once integrated, the Kerr-Schild version of xTrack will emit photons from the true photosphere of the disk, allow those photons to seed a corona generated from first principles and Comptonize, subsequently reflecting off or fluorescing in the disk. Another exciting prospect which the aforementioned TTGRRMHD data set will aid is developing a model to measure spin based on hfQPO frequencies. The tearing radius is determined by the spin, inclination, and thickness of the disk. If high resolution spectral measurements can constrain the accretion rate and the state of the disk allowing an estimation of its thickness, and orbital measurements can estimate the inclination of the binary giving a measure of the disk misalignment, then the frequency of hfQPOs could stand as a viable measure of black hole spin. It would also be worthwhile to incorporate older *H-AMR* data sets which did not show oscillatory signals in $\dot{M}$ or $\dot{M}_r$ but did show precession to determine if there are lfQPO and hfQPO oscillations in the spectral output. These works can and will be computed with minimal effort given the current status of the code.

APPENDICES

Appendix A

Tetrads

In classical Euclidean space any vector element of any space can be described in any basis. Consider a space $\mathbf{S^n}$ having n elements, and let $B = \{\vec{b}_0, \vec{b}_1, ..., \vec{b}_n\}$ be a set of n vectors such that $B \in \mathbf{S}$. If the elements of B are linearly independent and span $\mathbf{S}$ then B is a basis of $\mathbf{S}$. Thus, any vector $\vec{v} \in \mathbf{S}$ may be written in terms of the basis B such that $\vec{v} = \{v_1, v_2, ..., v_3\} = a_1\vec{b}_1 + a_2\vec{b}_2 + ...a_n\vec{b}_n$ where $a_1...a_n$ are scalar constants. The vector $\vec{v}$ in basis B is given by $\vec{a} = \{a_1, a_2, ..., a_n\}$. The basis B is not unique, however, and there may exist other bases which also properly span $\mathbf{S}$. Consider another set of n linearly independent vectors, $D = \{\vec{d}_0, \vec{d}_1, ..., \vec{d}_n\}$ which also span $\mathbf{S}$. We may describe $\vec{v} = \{v_1, v_2, ..., v_3\} = a_1\vec{b}_1 + a_2\vec{b}_2 + ...a_n\vec{b}_n = c_1\vec{d}_1 + c_2\vec{d}_2 + ...c_n\vec{d}_n$. Regardless of which basis we choose, the fundamental properties of $\vec{v}$, for example $|\vec{v}|$ or the direction of $\vec{v}$, remain unchanged. Most importantly, the transformation to a basis is reversible. Letting $\vec{v} = a_1\vec{b}_1 + a_2\vec{b}_2 + ...a_n\vec{b}_n = B\vec{a}$, then $\vec{a} = B^{-1}\vec{v}$ where B^{-1} is the inverse of B, such that $BB^{-1} = 1$

In order to fully illustrate the utility of our choice of choice of basis, consider two vectors in Euclidean space, $\vec{A}$ and $\vec{D}$, described by the same orthonormal basis $E = \vec{e}_1, \vec{e}_2, ...\vec{e}_n$, as $\vec{A} = E\vec{a} = \vec{e}_\mu a^\mu$ and $\vec{D} = E\vec{d} = \vec{e}_\nu d^\nu$. Here the switch is made to scripted notation, with $\vec{e}_\alpha$ referring to one vector in the basis E and a^α referring to one component of the vector $\vec{a}$. The dot product of $\vec{A}$ and $\vec{D}$ is $\vec{A} \cdot \vec{D} = \vec{e}_\mu a^\mu \vec{e}_\nu d^\nu = a^\mu d^\nu (\vec{e}_\mu \vec{e}_\nu)$. By definition, $\vec{e}_\mu \vec{e}_\nu = 0$

for all $\mu \neq \nu$ and $\vec{e}_\mu \vec{e}_\nu = 1$ for all $\mu = \nu$. If the requirement is placed on the basis that $\vec{e}_\mu \vec{e}_\nu = -1$ for $\mu = \nu = 0$, the basis describes a space that is locally Lorentzian (i.e., respects Lorentz transformations and thus conserves Lorentz invariance). Additionally, if $\vec{e}_\mu \vec{e}_\nu = 1$ for $\mu = \nu = 1, 2, 3$, the basis recovers the metric of Minkowski, which describes locally flat space time $\vec{e}_\mu \vec{e}_\nu = \eta_{\mu\nu}$.

It follows that one can write any metric for any space in terms of the outer product of an orthonormal basis with itself, and can be shown that any set of mutually orthonormal vectors tangent to a space constitute a basis of that space. In concert with the fact that any point in spacetime can be described as locally flat on some interval, one can construct a tetrad and thus a metric from any set of vectors which satisfy these conditions. This choice of mutually orthonormal tangents which together form a tetrad is what is meant by choosing a 'frame.' The tangents cannot be chosen arbitrarily, however. The zeroth component of the tetrad, corresponding to the dimension of time, must be properly timelike (i.e., $|\mathbf{e_t}| = -\mathbf{1}$), and the spatial tangents must be properly spacelike. The Kerr metric, for example, can be written in terms of the Boyer-Lindquist basis vectors, $g_{\mu\nu} = \mathbf{e}_\mu \mathbf{e}_\nu$, where each $\mathbf{e}_\mu$ corresponds to the Boyer-Lindquist tangent vector ∂_μ. A tetrad describing the rest frame of an equatorial accretion disk can then be built from these tangent vectors, and by extension from the metric itself. We first assume that the zeroth tangent is proportional to the velocity of the accretion flow, which orbits with Keplerian frequency Ω_k,

$$\mathbf{e_{\tilde{t}}} \propto \partial_\mathbf{t} + \mathbf{\Omega_k} \partial_\phi. \tag{A.1}$$

There are no r or θ components of momentum, thus

$$\mathbf{e_{\tilde{r}}} \propto \partial_\mathbf{r} \tag{A.2}$$

and

$$\mathbf{e}_{\tilde{\theta}} \propto \partial_{\theta}. \tag{A.3}$$

The last tangent vector must be mutually orthogonal to all others, so it must have a form

$$\mathbf{e}_{\tilde{\phi}} \propto \alpha\partial_{\mathbf{t}} + \beta\partial_{\phi}. \tag{A.4}$$

These four basis vectors constitute a tetrad and allow us to transform into and out of the frame of the disk. We can describe a photon wave vector, $\mathbf{k}^{\mu}$, in a general frame as the product of this basis and the wave vector in the plasma frame, which is denoted with a tilde,

$$\mathbf{k}^{\nu} = \mathbf{e}^{\nu}{}_{\tilde{\mu}}\mathbf{k}^{\tilde{\mu}}. \tag{A.5}$$

As above, we can use the inverse of this tetrad, $\bar{\mathbf{e}}_{\nu}{}^{\tilde{\mu}}$, to find the wave vector in the plasma frame, $\mathbf{k}^{\tilde{\mu}}$,

$$\mathbf{k}^{\tilde{\mu}} = \bar{\mathbf{e}}_{\nu}{}^{\tilde{\mu}}\mathbf{k}^{\nu} \tag{A.6}$$

For an equatorial disk in the Kerr Metric in Boyer-Lindquist coordinates, the orthogonalization of these tangents can be done by hand. However, a disk geometry that deviates from the equatorial disk, or the use of a different coordinate system, adds non-trivial complexity to the system of equations. In such cases, the solution is to turn to an algorithmic approach to orthogonalization.

The Graham-Schmidt process allows one to take a finite set of k linearly independent vectors v^k in an n-dimensional subspace $\mathcal{S}^k$ (where $k \leq n$, $v^k \in \mathcal{S}^k$, and $\mathcal{S}^k \subset \mathcal{R}^n$) and reduce them to a linearly independent k-dimensional set of vectors $\mathcal{B}^k$ which span $\mathcal{S}^k$. This is achieved by choosing some vector in the set v^k as a starting point and letting it be the

first vector in the orthogonal basis $\mathcal{B}^k$. Let that initial vector be $v^1 = b^1$. The next vector in the basis is found by subtracting the projection of b^1 onto v^2 from v^2, this yields a vector $b^2 \perp b^1$. This process is repeated for all v^k. The projection operator is

$$\mathcal{P}_b^\mu(v) = \frac{b_\mu v^\nu}{b_\mu b^\nu} b^\mu \tag{A.7}$$

The entire algorithm can written as

$$b^k = v^k - \sum_{i=1}^{k-1} \mathcal{P}_{b^k}(v^k), \tag{A.8}$$

where each vector b^k is normalized after it is computed and before the algorithm continues. It is worth noting that applying Graham-Schmidt to a set of tangents will by definition produce an orthonormal set of vectors which are Lorentzian, but care must be taken in choosing the both the tangents and the order of the orthogonalization to ensure that the resultant basis correctly describes the frame of interest. An easy check to ensure that the basis is a proper tetrad of the frame is to transform the input vector $\mathbf{e}_{\tilde{t}} = u^\mu$, which is the four velocity of the frame, into its own rest-frame and check that $u^\mu_{rf} = \bar{\mathbf{e}}_\nu^{\tilde{\mu}} \cdot \mathbf{u}^\mu = (\mathbf{1}, \mathbf{0}, \mathbf{0}, \mathbf{0})$. If this condition is satisfied, the tetrad properly describes the frame.

Bibliography

[1] T. Muñoz-Darias, R. P. Fender, S. E. Motta, and T. M. Belloni. Black hole-like hysteresis and accretion states in neutron star low-mass X-ray binaries. *MNRAS,*, 443(4):3270–3283, October 2014.

[2] Tomaso M. Belloni and Sara E. Motta. Transient Black Hole Binaries. In Cosimo Bambi, editor, *Astrophysics of Black Holes: From Fundamental Aspects to Latest Developments*, volume 440 of *Astrophysics and Space Science Library*, page 61, January 2016.

[3] A. Einstein. Die Grundlage der allgemeinen Relativitätstheorie. *Annalen der Physik*, 354(7):769–822, January 1916.

[4] K. Schwarzschild. On the Gravitational Field of a Mass Point According to Einstein's Theory. *Abh. Konigl. Preuss. Akad. Wissenschaften Jahre 1906,92, Berlin,1907*, 1916:189–196, January 1916.

[5] David Finkelstein. Past-future asymmetry of the gravitational field of a point particle. *Phys. Rev.*, 110:965–967, May 1958.

[6] Charles W. Misner, Kip S. Thorne, and John Archibald Wheeler. *Gravitation*. 1973.

[7] Roy P. Kerr. Gravitational Field of a Spinning Mass as an Example of Algebraically Special Metrics. *Phys. Rev. Lett.,*, 11(5):237–238, September 1963.

[8] C. T. Bolton. Identification of Cygnus X-1 with HDE 226868. *Nature,*, 235(5336):271–273, February 1972.

[9] B. Louise Webster and Paul Murdin. Cygnus X-1-a Spectroscopic Binary with a Heavy Companion ? *Nature,*, 235(5332):37–38, January 1972.

[10] J. M. Corral-Santana, J. Casares, T. Muñoz-Darias, F. E. Bauer, I. G. Martínez-Pais, and D. M. Russell. BlackCAT: A catalogue of stellar-mass black holes in X-ray transients. *A&A,*, 587:A61, March 2016.

[11] B. P. Abbott, R. Abbott, T. D. Abbott, M. R. Abernathy, F. Acernese, K. Ackley, C. Adams, T. Adams, P. Addesso, R. X. Adhikari, V. B. Adya, C. Affeldt, M. Agathos, K. Agatsuma, N. Aggarwal, O. D. Aguiar, L. Aiello, A. Ain, P. Ajith, B. Allen, A. Allocca, P. A. Altin, S. B. Anderson, W. G. Anderson, K. Arai, M. C. Araya, C. C. Arceneaux, J. S. Areeda, N. Arnaud, K. G. Arun, S. Ascenzi, G. Ashton, M. Ast, S. M. Aston, P. Astone, P. Aufmuth, C. Aulbert, S. Babak, P. Bacon, M. K. M. Bader, P. T. Baker, F. Baldaccini, G. Ballardin, S. W. Ballmer, J. C. Barayoga, S. E. Barclay, B. C. Barish, D. Barker, F. Barone, B. Barr, L. Barsotti, M. Barsuglia, D. Barta, J. Bartlett, I. Bartos, R. Bassiri, A. Basti, J. C. Batch, C. Baune, V. Bavigadda, M. Bazzan, M. Bejger, A. S. Bell, B. K. Berger, G. Bergmann, C. P. L. Berry, D. Bersanetti, A. Bertolini, J. Betzwieser, S. Bhagwat, R. Bhandare, I. A. Bilenko, G. Billingsley, J. Birch, R. Birney, O. Birnholtz, S. Biscans, A. Bisht, M. Bitossi, C. Biwer, M. A. Bizouard, J. K. Blackburn, C. D. Blair, D. G. Blair, R. M. Blair, S. Bloemen, O. Bock, M. Boer, G. Bogaert, C. Bogan, A. Bohe, C. Bond, F. Bondu,

R. Bonnand, B. A. Boom, R. Bork, V. Boschi, S. Bose, Y. Bouffanais, A. Bozzi, C. Bradaschia, P. R. Brady, V. B. Braginsky, M. Branchesi, J. E. Brau, T. Briant, A. Brillet, M. Brinkmann, V. Brisson, P. Brockill, J. E. Broida, A. F. Brooks, D. A. Brown, D. D. Brown, N. M. Brown, S. Brunett, C. C. Buchanan, A. Buikema, T. Bulik, H. J. Bulten, A. Buonanno, D. Buskulic, C. Buy, R. L. Byer, M. Cabero, L. Cadonati, G. Cagnoli, C. Cahillane, J. Calderón Bustillo, T. Callister, E. Calloni, J. B. Camp, K. C. Cannon, J. Cao, C. D. Capano, E. Capocasa, F. Carbognani, S. Caride, J. Casanueva Diaz, C. Casentini, S. Caudill, M. Cavaglià, F. Cavalier, R. Cavalieri, G. Cella, C. B. Cepeda, L. Cerboni Baiardi, G. Cerretani, E. Cesarini, S. J. Chamberlin, M. Chan, S. Chao, P. Charlton, E. Chassande-Mottin, B. D. Cheeseboro, H. Y. Chen, Y. Chen, C. Cheng, A. Chincarini, A. Chiummo, H. S. Cho, M. Cho, J. H. Chow, N. Christensen, Q. Chu, S. Chua, S. Chung, G. Ciani, F. Clara, J. A. Clark, F. Cleva, E. Coccia, P. F. Cohadon, A. Colla, C. G. Collette, L. Cominsky, M. Constancio, A. Conte, L. Conti, D. Cook, T. R. Corbitt, N. Cornish, A. Corsi, S. Cortese, C. A. Costa, M. W. Coughlin, S. B. Coughlin, J. P. Coulon, S. T. Countryman, P. Couvares, E. E. Cowan, D. M. Coward, M. J. Cowart, D. C. Coyne, R. Coyne, K. Craig, J. D. E. Creighton, J. Cripe, S. G. Crowder, A. Cumming, L. Cunningham, E. Cuoco, T. Dal Canton, S. L. Danilishin, S. D'Antonio, K. Danzmann, N. S. Darman, A. Dasgupta, C. F. Da Silva Costa, V. Dattilo, I. Dave, M. Davier, G. S. Davies, E. J. Daw, R. Day, S. De, D. DeBra, G. Debreczeni, J. Degallaix, M. De Laurentis, S. Deléglise, W. Del Pozzo, T. Denker, T. Dent, V. Dergachev, R. De Rosa, R. T. DeRosa, R. DeSalvo, R. C. Devine, S. Dhurandhar, M. C. Díaz, L. Di Fiore, M. Di Giovanni, T. Di Girolamo, A. Di Lieto, S. Di Pace, I. Di Palma, A. Di Virgilio, V. Dolique, F. Donovan, K. L. Dooley, S. Doravari, R. Douglas, T. P. Downes, M. Drago, R. W. P. Drever, J. C. Driggers, M. Ducrot, S. E. Dwyer, T. B. Edo, M. C. Edwards, A. Effler, H. B. Eggenstein,

P. Ehrens, J. Eichholz, S. S. Eikenberry, W. Engels, R. C. Essick, T. Etzel, M. Evans, T. M. Evans, R. Everett, M. Factourovich, V. Fafone, H. Fair, S. Fairhurst, X. Fan, Q. Fang, S. Farinon, B. Farr, W. M. Farr, M. Favata, M. Fays, H. Fehrmann, M. M. Fejer, E. Fenyvesi, I. Ferrante, E. C. Ferreira, F. Ferrini, F. Fidecaro, I. Fiori, D. Fiorucci, R. P. Fisher, R. Flaminio, M. Fletcher, H. Fong, J. D. Fournier, S. Frasca, F. Frasconi, Z. Frei, A. Freise, R. Frey, V. Frey, P. Fritschel, V. V. Frolov, P. Fulda, M. Fyffe, H. A. G. Gabbard, S. Gaebel, J. R. Gair, L. Gammaitoni, S. G. Gaonkar, F. Garufi, G. Gaur, N. Gehrels, G. Gemme, P. Geng, E. Genin, A. Gennai, J. George, L. Gergely, V. Germain, Abhirup Ghosh, Archisman Ghosh, S. Ghosh, J. A. Giaime, K. D. Giardina, A. Giazotto, K. Gill, A. Glaefke, E. Goetz, R. Goetz, L. Gondan, G. González, J. M. Gonzalez Castro, A. Gopakumar, N. A. Gordon, M. L. Gorodetsky, S. E. Gossan, M. Gosselin, R. Gouaty, A. Grado, C. Graef, P. B. Graff, M. Granata, A. Grant, S. Gras, C. Gray, G. Greco, A. C. Green, P. Groot, H. Grote, S. Grunewald, G. M. Guidi, X. Guo, A. Gupta, M. K. Gupta, K. E. Gushwa, E. K. Gustafson, R. Gustafson, J. J. Hacker, B. R. Hall, E. D. Hall, H. Hamilton, G. Hammond, M. Haney, M. M. Hanke, J. Hanks, C. Hanna, M. D. Hannam, J. Hanson, T. Hardwick, J. Harms, G. M. Harry, I. W. Harry, M. J. Hart, M. T. Hartman, C. J. Haster, K. Haughian, J. Healy, A. Heidmann, M. C. Heintze, H. Heitmann, P. Hello, G. Hemming, M. Hendry, I. S. Heng, J. Hennig, J. Henry, A. W. Heptonstall, M. Heurs, S. Hild, D. Hoak, D. Hofman, K. Holt, D. E. Holz, P. Hopkins, J. Hough, E. A. Houston, E. J. Howell, Y. M. Hu, S. Huang, E. A. Huerta, D. Huet, B. Hughey, S. Husa, S. H. Huttner, T. Huynh-Dinh, N. Indik, D. R. Ingram, R. Inta, H. N. Isa, J. M. Isac, M. Isi, T. Isogai, B. R. Iyer, K. Izumi, T. Jacqmin, H. Jang, K. Jani, P. Jaranowski, S. Jawahar, L. Jian, F. Jiménez-Forteza, W. W. Johnson, N. K. Johnson-McDaniel, D. I. Jones, R. Jones, R. J. G. Jonker, L. Ju, Haris K, C. V. Kalaghatgi, V. Kalogera, S. Kandhasamy,

G. Kang, J. B. Kanner, S. J. Kapadia, S. Karki, K. S. Karvinen, M. Kasprzack, E. Katsavounidis, W. Katzman, S. Kaufer, T. Kaur, K. Kawabe, F. Kéfélian, M. S. Kehl, D. Keitel, D. B. Kelley, W. Kells, R. Kennedy, J. S. Key, F. Y. Khalili, I. Khan, S. Khan, Z. Khan, E. A. Khazanov, N. Kijbunchoo, Chi-Woong Kim, Chunglee Kim, J. Kim, K. Kim, N. Kim, W. Kim, Y. M. Kim, S. J. Kimbrell, E. J. King, P. J. King, J. S. Kissel, B. Klein, L. Kleybolte, S. Klimenko, S. M. Koehlenbeck, S. Koley, V. Kondrashov, A. Kontos, M. Korobko, W. Z. Korth, I. Kowalska, D. B. Kozak, V. Kringel, B. Krishnan, A. Królak, C. Krueger, G. Kuehn, P. Kumar, R. Kumar, L. Kuo, A. Kutynia, B. D. Lackey, M. Landry, J. Lange, B. Lantz, P. D. Lasky, M. Laxen, A. Lazzarini, C. Lazzaro, P. Leaci, S. Leavey, E. O. Lebigot, C. H. Lee, H. K. Lee, H. M. Lee, K. Lee, A. Lenon, M. Leonardi, J. R. Leong, N. Leroy, N. Letendre, Y. Levin, J. B. Lewis, T. G. F. Li, A. Libson, T. B. Littenberg, N. A. Lockerbie, A. L. Lombardi, L. T. London, J. E. Lord, M. Lorenzini, V. Loriette, M. Lormand, G. Losurdo, J. D. Lough, C. Lousto, H. Lück, A. P. Lundgren, R. Lynch, Y. Ma, B. Machenschalk, M. MacInnis, D. M. Macleod, F. Magaña-Sandoval, L. Magaña Zertuche, R. M. Magee, E. Majorana, I. Maksimovic, V. Malvezzi, N. Man, I. Mandel, V. Mandic, V. Mangano, G. L. Mansell, M. Manske, M. Mantovani, F. Marchesoni, F. Marion, S. Márka, Z. Márka, A. S. Markosyan, E. Maros, F. Martelli, L. Martellini, I. W. Martin, D. V. Martynov, J. N. Marx, K. Mason, A. Masserot, T. J. Massinger, M. Masso-Reid, S. Mastrogiovanni, F. Matichard, L. Matone, N. Mavalvala, N. Mazumder, R. McCarthy, D. E. McClelland, S. McCormick, S. C. McGuire, G. McIntyre, J. McIver, D. J. McManus, T. McRae, S. T. McWilliams, D. Meacher, G. D. Meadors, J. Meidam, A. Melatos, G. Mendell, R. A. Mercer, E. L. Merilh, M. Merzougui, S. Meshkov, C. Messenger, C. Messick, R. Metzdorff, P. M. Meyers, F. Mezzani, H. Miao, C. Michel, H. Middleton, E. E. Mikhailov, L. Milano, A. L. Miller, A. Miller, B. B. Miller, J. Miller, M. Millhouse,

Y. Minenkov, J. Ming, S. Mirshekari, C. Mishra, S. Mitra, V. P. Mitrofanov, G. Mitselmakher, R. Mittleman, A. Moggi, M. Mohan, S. R. P. Mohapatra, M. Montani, B. C. Moore, C. J. Moore, D. Moraru, G. Moreno, S. R. Morriss, K. Mossavi, B. Mours, C. M. Mow-Lowry, G. Mueller, A. W. Muir, Arunava Mukherjee, D. Mukherjee, S. Mukherjee, N. Mukund, A. Mullavey, J. Munch, D. J. Murphy, P. G. Murray, A. Mytidis, I. Nardecchia, L. Naticchioni, R. K. Nayak, K. Nedkova, G. Nelemans, T. J. N. Nelson, M. Neri, A. Neunzert, G. Newton, T. T. Nguyen, A. B. Nielsen, S. Nissanke, A. Nitz, F. Nocera, D. Nolting, M. E. N. Normandin, L. K. Nuttall, J. Oberling, E. Ochsner, J. O'Dell, E. Oelker, G. H. Ogin, J. J. Oh, S. H. Oh, F. Ohme, M. Oliver, P. Oppermann, Richard J. Oram, B. O'Reilly, R. O'Shaughnessy, D. J. Ottaway, H. Overmier, B. J. Owen, A. Pai, S. A. Pai, J. R. Palamos, O. Palashov, C. Palomba, A. Pal-Singh, H. Pan, Y. Pan, C. Pankow, F. Pannarale, B. C. Pant, F. Paoletti, A. Paoli, M. A. Papa, H. R. Paris, W. Parker, D. Pascucci, A. Pasqualetti, R. Passaquieti, D. Passuello, B. Patricelli, Z. Patrick, B. L. Pearlstone, M. Pedraza, R. Pedurand, L. Pekowsky, A. Pele, S. Penn, A. Perreca, L. M. Perri, H. P. Pfeiffer, M. Phelps, O. J. Piccinni, M. Pichot, F. Piergiovanni, V. Pierro, G. Pillant, L. Pinard, I. M. Pinto, M. Pitkin, M. Poe, R. Poggiani, P. Popolizio, E. Porter, A. Post, J. Powell, J. Prasad, V. Predoi, T. Prestegard, L. R. Price, M. Prijatelj, M. Principe, S. Privitera, R. Prix, G. A. Prodi, L. Prokhorov, O. Puncken, M. Punturo, P. Puppo, M. Pürrer, H. Qi, J. Qin, S. Qiu, V. Quetschke, E. A. Quintero, R. Quitzow-James, F. J. Raab, D. S. Rabeling, H. Radkins, P. Raffai, S. Raja, C. Rajan, M. Rakhmanov, P. Rapagnani, V. Raymond, M. Razzano, V. Re, J. Read, C. M. Reed, T. Regimbau, L. Rei, S. Reid, D. H. Reitze, H. Rew, S. D. Reyes, F. Ricci, K. Riles, M. Rizzo, N. A. Robertson, R. Robie, F. Robinet, A. Rocchi, L. Rolland, J. G. Rollins, V. J. Roma, J. D. Romano, R. Romano, G. Romanov, J. H. Romie, D. Rosińska, S. Rowan, A. Rüdiger,

P. Ruggi, K. Ryan, S. Sachdev, T. Sadecki, L. Sadeghian, M. Sakellariadou, L. Salconi, M. Saleem, F. Salemi, A. Samajdar, L. Sammut, E. J. Sanchez, V. Sandberg, B. Sandeen, J. R. Sanders, B. Sassolas, B. S. Sathyaprakash, P. R. Saulson, O. E. S. Sauter, R. L. Savage, A. Sawadsky, P. Schale, R. Schilling, J. Schmidt, P. Schmidt, R. Schnabel, R. M. S. Schofield, A. Schönbeck, E. Schreiber, D. Schuette, B. F. Schutz, J. Scott, S. M. Scott, D. Sellers, A. S. Sengupta, D. Sentenac, V. Sequino, A. Sergeev, Y. Setyawati, D. A. Shaddock, T. Shaffer, M. S. Shahriar, M. Shaltev, B. Shapiro, P. Shawhan, A. Sheperd, D. H. Shoemaker, D. M. Shoemaker, K. Siellez, X. Siemens, M. Sieniawska, D. Sigg, A. D. Silva, A. Singer, L. P. Singer, A. Singh, R. Singh, A. Singhal, A. M. Sintes, B. J. J. Slagmolen, J. R. Smith, N. D. Smith, R. J. E. Smith, E. J. Son, B. Sorazu, F. Sorrentino, T. Souradeep, A. K. Srivastava, A. Staley, M. Steinke, J. Steinlechner, S. Steinlechner, D. Steinmeyer, B. C. Stephens, S. Stevenson, R. Stone, K. A. Strain, N. Straniero, G. Stratta, N. A. Strauss, S. Strigin, R. Sturani, A. L. Stuver, T. Z. Summerscales, L. Sun, S. Sunil, P. J. Sutton, B. L. Swinkels, M. J. Szczepańczyk, M. Tacca, D. Talukder, D. B. Tanner, M. Tápai, S. P. Tarabrin, A. Taracchini, R. Taylor, T. Theeg, M. P. Thirugnanasambandam, E. G. Thomas, M. Thomas, P. Thomas, K. A. Thorne, E. Thrane, S. Tiwari, V. Tiwari, K. V. Tokmakov, K. Toland, C. Tomlinson, M. Tonelli, Z. Tornasi, C. V. Torres, C. I. Torrie, D. Töyrä, F. Travasso, G. Traylor, D. Trifirò, M. C. Tringali, L. Trozzo, M. Tse, M. Turconi, D. Tuyenbayev, D. Ugolini, C. S. Unnikrishnan, A. L. Urban, S. A. Usman, H. Vahlbruch, G. Vajente, G. Valdes, M. Vallisneri, N. van Bakel, M. van Beuzekom, J. F. J. van den Brand, C. Van Den Broeck, D. C. Vander-Hyde, L. van der Schaaf, J. V. van Heijningen, A. A. van Veggel, M. Vardaro, S. Vass, M. Vasúth, R. Vaulin, A. Vecchio, G. Vedovato, J. Veitch, P. J. Veitch, K. Venkateswara, D. Verkindt, F. Vetrano, A. Viceré, S. Vinciguerra, D. J. Vine, J. Y. Vinet, S. Vitale, T. Vo, H. Vocca,

C. Vorvick, D. V. Voss, W. D. Vousden, S. P. Vyatchanin, A. R. Wade, L. E. Wade, M. Wade, M. Walker, L. Wallace, S. Walsh, G. Wang, H. Wang, M. Wang, X. Wang, Y. Wang, R. L. Ward, J. Warner, M. Was, B. Weaver, L. W. Wei, M. Weinert, A. J. Weinstein, R. Weiss, L. Wen, P. Weßels, T. Westphal, K. Wette, J. T. Whelan, S. E. Whitcomb, B. F. Whiting, R. D. Williams, A. R. Williamson, J. L. Willis, B. Willke, M. H. Wimmer, W. Winkler, C. C. Wipf, H. Wittel, G. Woan, J. Woehler, J. Worden, J. L. Wright, D. S. Wu, G. Wu, J. Yablon, W. Yam, H. Yamamoto, C. C. Yancey, H. Yu, M. Yvert, A. ZadroŻny, L. Zangrando, M. Zanolin, J. P. Zendri, M. Zevin, L. Zhang, M. Zhang, Y. Zhang, C. Zhao, M. Zhou, Z. Zhou, X. J. Zhu, M. E. Zucker, S. E. Zuraw, J. Zweizig, LIGO Scientific Collaboration, and Virgo Collaboration. Binary Black Hole Mergers in the First Advanced LIGO Observing Run. *Physical Review X*, 6(4):041015, October 2016.

[12] Richard. M. Plotkin, Elena Gallo, and Peter G. Jonker. The X-Ray Spectral Evolution of Galactic Black Hole X-Ray Binaries toward Quiescence. *ApJ,*, 773(1):59, August 2013.

[13] Malcolm S. Longair. *High Energy Astrophysics*. 2011.

[14] George B. Rybicki and Alan P. Lightman. *Radiative Processes in Astrophysics*. 1986.

[15] David Pooley, Jeffrey A. Blackburne, Saul Rappaport, and Paul L. Schechter. X-Ray and Optical Flux Ratio Anomalies in Quadruply Lensed Quasars. I. Zooming in on Quasar Emission Regions. *ApJ,*, 661(1):19–29, May 2007.

[16] G. Chartas, C. S. Kochanek, X. Dai, S. Poindexter, and G. Garmire. X-Ray Microlensing in RXJ1131-1231 and HE1104-1805. *ApJ,*, 693(1):174–185, March 2009.

[17] X. Dai, C. S. Kochanek, G. Chartas, S. Kozłowski, C. W. Morgan, G. Garmire, and E. Agol. The Sizes of the X-ray and Optical Emission Regions of RXJ 1131-1231. *ApJ,*, 709(1):278–285, January 2010.

[18] A. C. Fabian, A. Zoghbi, R. R. Ross, P. Uttley, L. C. Gallo, W. N. Brandt, A. J. Blustin, T. Boller, M. D. Caballero-Garcia, J. Larsson, J. M. Miller, G. Miniutti, G. Ponti, R. C. Reis, C. S. Reynolds, Y. Tanaka, and A. J. Young. Broad line emission from iron K- and L-shell transitions in the active galaxy 1H0707-495. *Nature,*, 459(7246):540–542, May 2009.

[19] E. Kara, A. C. Fabian, E. M. Cackett, G. Miniutti, and P. Uttley. Revealing the X-ray source in IRAS 13224-3809 through flux-dependent reverberation lags. *MNRAS,*, 430(2):1408–1413, April 2013.

[20] E. Kara, E. M. Cackett, A. C. Fabian, C. Reynolds, and P. Uttley. The curious time lags of PG 1244+026: discovery of the iron K reverberation lag. *MNRAS,*, 439:L26–L30, March 2014.

[21] E. Kara, J. F. Steiner, A. C. Fabian, E. M. Cackett, P. Uttley, R. A. Remillard, K. C. Gendreau, Z. Arzoumanian, D. Altamirano, S. Eikenberry, T. Enoto, J. Homan, J. Neilsen, and A. L. Stevens. The corona contracts in a black-hole transient. *Nature,*, 565(7738):198–201, January 2019.

[22] Henric Krawczynski, Fabio Muleri, Michal Dovčiak, Alexandra Veledina, Nicole Rodriguez Cavero, Jiri Svoboda, Adam Ingram, Giorgio Matt, Javier A. Garcia, Vladislav Loktev, Michela Negro, Juri Poutanen, Takao Kitaguchi, Jakub Podgorný, John Rankin, Wenda Zhang, Andrei Berdyugin, Svetlana V. Berdyugina, Stefano Bianchi, Dmitry Blinov, Fiamma Capitanio, Niccolò Di Lalla, Paul Draghis, Sergio Fabiani,

Masato Kagitani, Vadim Kravtsov, Sebastian Kiehlmann, Luca Latronico, Alexander A. Lutovinov, Nikos Mandarakas, Frédéric Marin, Andrea Marinucci, Jon M. Miller, Tsunefumi Mizuno, Sergey V. Molkov, Nicola Omodei, Pierre-Olivier Petrucci, Ajay Ratheesh, Takeshi Sakanoi, Andrei N. Semena, Raphael Skalidis, Paolo Soffitta, Allyn F. Tennant, Phillipp Thalhammer, Francesco Tombesi, Martin C. Weisskopf, Joern Wilms, Sixuan Zhang, Iván Agudo, Lucio A. Antonelli, Matteo Bachetti, Luca Baldini, Wayne H. Baumgartner, Ronaldo Bellazzini, Stephen D. Bongiorno, Raffaella Bonino, Alessandro Brez, Niccolò Bucciantini, Simone Castellano, Elisabetta Cavazzuti, Stefano Ciprini, Enrico Costa, Alessandra De Rosa, Ettore Del Monte, Laura Di Gesu, Alessandro Di Marco, Immacolata Donnarumma, Victor Doroshenko, Steven R. Ehlert, Teruaki Enoto, Yuri Evangelista, Riccardo Ferrazzoli, Shuichi Gunji, Kiyoshi Hayashida, Jeremy Heyl, Wataru Iwakiri, Svetlana G. Jorstad, Vladimir Karas, Jeffery J. Kolodziejczak, Fabio La Monaca, Ioannis Liodakis, Simone Maldera, Alberto Manfreda, Alan P. Marscher, Herman L. Marshall, Ikuyuki Mitsuishi, Chi-Yung Ng, Stephen L. O'Dell, Chiara Oppedisano, Alessandro Papitto, George G. Pavlov, Abel L. Peirson, Matteo Perri, Melissa Pesce-Rollins, Maura Pilia, Andrea Possenti, Simonetta Puccetti, Brian D. Ramsey, Roger W. Romani, Carmelo Sgrò, Patrick Slane, Gloria Spandre, Toru Tamagawa, Fabrizio Tavecchio, Roberto Taverna, Yuzuru Tawara, Nicholas E. Thomas, Alessio Trois, Sergey Tsygankov, Roberto Turolla, Jacco Vink, Kinwah Wu, Fei Xie, and Silvia Zane. Polarized x-rays constrain the disk-jet geometry in the black hole x-ray binary Cygnus X-1. *Science*, 378(6620):650–654, November 2022.

[23] F. Kislat, B. Clark, M. Beilicke, and H. Krawczynski. Analyzing the data from X-ray polarimeters with Stokes parameters. *Astroparticle Physics*, 68:45–51, August 2015.

[24] Subrahmanyan Chandrasekhar. *Radiative transfer*. 1960.

[25] A. Zee. *Einstein Gravity in a Nutshell*. 2013.

[26] Jeremy D. Schnittman and Julian H. Krolik. X-ray Polarization from Accreting Black Holes: The Thermal State. *ApJ,*, 701(2):1175–1187, August 2009.

[27] Li-Xin Li, Ramesh Narayan, and Jeffrey E. McClintock. Inferring the Inclination of a Black Hole Accretion Disk from Observations of its Polarized Continuum Radiation. *ApJ,*, 691(1):847–865, January 2009.

[28] K. S. Long, G. A. Chanan, and R. Novick. The X-ray polarization of the CYG sources. *ApJ,*, 238:710–716, June 1980.

[29] M. Beilicke, W. R. Binns, J. Buckley, R. Cowsik, P. Dowkontt, A. Garson, Q. Guo, M. H. Israel, K. Lee, H. Krawczynski, M. G. Baring, S. Barthelmy, T. Okajima, J. Schnittman, J. Tueller, Y. Haba, H. Kunieda, H. Matsumoto, T. Miyazawa, and K. Tamura. The Hard X-ray Polarimeter X-Calibur - Design and Tests. *arXiv e-prints*, page arXiv:1109.6850, September 2011.

[30] Fabian Kislat, Quincy Abarr, Hisamitsu Awaki, Richard Bose, Dana Braun, Gianluigi de Geronimo, Paul Dowkontt, Enoto Teruaki, Manel Errando, Yasushi Fukazawa, Akihiro Furusawa, Thomas Gadson, Ephraim Gau, Victor Guarino, Shuichi Gunji, Kiyoshi Hayashida, Scott Heatwole, Fumiya Imazato, Kazunori Ishibashi, Manabu Ishida, Nirmal K. Iyer, Keon Harmon, Wataru Kamogawa, Mózsi Kiss, Takao Kitaguchi, Henric Krawczynski, R. James Lanzi, Lindsey Lisalda, Yoshitomo Maeda, Hiroto Matake, Hironori Matsumoto, Taisei Mineta, Takuya Miyazawa, Tsunefumi Mizuno, Takashi Okajima, Mark Pearce, Zachary Peterson, Brian Rauch, Nicole Rodriguez Cavero,

Felix Ryde, Yoshitaka Saito, Sean Spooner, Theodor-Adrian Stana, David Stuchlik, Hiromitsu Takahashi, Tomoshi Takeda, Mai Takeo, Toru Tamagawa, Hiroshi Tsunemi, Nagomi Uchida, Yuusuke Uchida, Keisuke Uchiyama, Andrew West, Eric Wulf, and Yuto Yoshida. The Next-Generation Hard X-ray Polarimeter XL-Calibur. In *AAS/High Energy Astrophysics Division*, volume 54 of *AAS/High Energy Astrophysics Division*, page 204.02, April 2022.

[31] Martin Weisskopf. The Imaging X-Ray Polarimetry Explorer (IXPE). In *43rd COSPAR Scientific Assembly. Held 28 January - 4 February*, volume 43, page 1647, January 2021.

[32] P. Casella, T. Belloni, and L. Stella. The ABC of Low-Frequency Quasi-periodic Oscillations in Black Hole Candidates: Analogies with Z Sources. *ApJ,*, 629(1):403–407, August 2005.

[33] Adam Ingram and Michiel van der Klis. An exact analytic treatment of propagating mass accretion rate fluctuations in X-ray binaries. *MNRAS,*, 434(2):1476–1485, September 2013.

[34] S. E. Motta, P. Casella, M. Henze, T. Muñoz-Darias, A. Sanna, R. Fender, and T. Belloni. Geometrical constraints on the origin of timing signals from black holes. *MNRAS,*, 447(2):2059–2072, February 2015.

[35] L. M. Heil, P. Uttley, and M. Klein-Wolt. Inclination-dependent spectral and timing properties in transient black hole X-ray binaries. *MNRAS,*, 448(4):3348–3353, April 2015.

[36] Adam Ingram, Chris Done, and P. Chris Fragile. Low-frequency quasi-periodic os-

cillations spectra and Lense-Thirring precession. *MNRAS,*, 397(1):L101–L105, July 2009.

[37] Adam Ingram, Michiel van der Klis, Matthew Middleton, Chris Done, Diego Altamirano, Lucy Heil, Phil Uttley, and Magnus Axelsson. A quasi-periodic modulation of the iron line centroid energy in the black hole binary H1743-322. *MNRAS,*, 461(2):1967–1980, September 2016.

[38] S. Motta, J. Homan, T. Muñoz Darias, P. Casella, T. M. Belloni, B. Hiemstra, and M. Méndez. Discovery of two simultaneous non-harmonically related quasi-periodic oscillations in the 2005 outburst of the black hole binary GRO J1655-40. *MNRAS,*, 427(1):595–606, November 2012.

[39] M. Kalamkar, P. Casella, P. Uttley, K. O'Brien, D. Russell, T. Maccarone, M. van der Klis, and F. Vincentelli. Detection of the first infra-red quasi-periodic oscillation in a black hole X-ray binary. *MNRAS,*, 460(3):3284–3291, August 2016.

[40] P. Gandhi, V. S. Dhillon, M. Durant, A. C. Fabian, A. Kubota, K. Makishima, J. Malzac, T. R. Marsh, J. M. Miller, T. Shahbaz, H. C. Spruit, and P. Casella. Rapid optical and X-ray timing observations of GX339-4: multicomponent optical variability in the low/hard state. *MNRAS,*, 407(4):2166–2192, October 2010.

[41] R. I. Hynes, C. A. Haswell, W. Cui, C. R. Shrader, K. O'Brien, S. Chaty, D. R. Skillman, J. Patterson, and Keith Horne. The remarkable rapid X-ray, ultraviolet, optical and infrared variability in the black hole XTE J1118+480. *MNRAS,*, 345(1):292–310, October 2003.

[42] R. P. Fender, J. Homan, and T. M. Belloni. Jets from black hole X-ray binaries:

testing, refining and extending empirical models for the coupling to X-rays. *MNRAS,*, 396(3):1370–1382, July 2009.

[43] E. H. Morgan, R. A. Remillard, and J. Greiner. RXTE Observations of QPOs in the Black Hole Candidate GRS 1915+105. *ApJ,*, 482(2):993–1010, June 1997.

[44] T. M. Belloni and D. Altamirano. Discovery of a 34 Hz quasi-periodic oscillation in the X-ray emission of GRS 1915+105. *MNRAS,*, 432(1):19–22, June 2013.

[45] Jeffrey E. McClintock, Rebecca Shafee, Ramesh Narayan, Ronald A. Remillard, Shane W. Davis, and Li-Xin Li. The Spin of the Near-Extreme Kerr Black Hole GRS 1915+105. *ApJ,*, 652(1):518–539, November 2006.

[46] D. Altamirano and T. Belloni. Discovery of High-frequency Quasi-periodic Oscillations in the Black Hole Candidate IGR J17091-3624. *ApJ,*, 747(1):L4, March 2012.

[47] Tod E. Strohmayer. Discovery of a 450 HZ Quasi-periodic Oscillation from the Microquasar GRO J1655-40 with the Rossi X-Ray Timing Explorer. *ApJ,*, 552(1):L49–L53, May 2001.

[48] T. M. Belloni, A. Sanna, and M. Méndez. High-frequency quasi-periodic oscillations in black hole binaries. *MNRAS,*, 426(3):1701–1709, November 2012.

[49] Ronald A. Remillard and Jeffrey E. McClintock. X-Ray Properties of Black-Hole Binaries. *ARA&A,*, 44(1):49–92, September 2006.

[50] N. I. Shakura and R. A. Sunyaev. Black holes in binary systems. Observational appearance. *A&A,*, 24:337–355, 1973.

[51] I. D. Novikov and K. S. Thorne. Astrophysics of black holes. In *Black Holes (Les Astres Occlus)*, pages 343–450, January 1973.

[52] Don N. Page and Kip S. Thorne. Disk-Accretion onto a Black Hole. Time-Averaged Structure of Accretion Disk. *ApJ,*, 191:499–506, July 1974.

[53] Andrea Martocchia and Giorgio Matt. Iron Kalpha line intensity from accretion discs around rotating black holes. *MNRAS,*, 282(4):L53–L57, October 1996.

[54] Anderson Caproni, Zulema Abraham, and Herman J. Mosquera Cuesta. Bardeen-Petterson Effect and the Disk Structure of the Seyfert Galaxy NGC 1068. *ApJ,*, 638(1):120–124, February 2006.

[55] R. M. Hjellming and M. P. Rupen. Episodic ejection of relativistic jets by the X-ray transient GRO J1655 - 40. *Nature,*, 375(6531):464–468, June 1995.

[56] Alexander Tchekhovskoy, Brian D. Metzger, Dimitrios Giannios, and Luke Z. Kelley. Swift J1644+57 gone MAD: the case for dynamically important magnetic flux threading the black hole in a jetted tidal disruption event. *MNRAS,*, 437(3):2744–2760, January 2014.

[57] A. L. Kinney, H. R. Schmitt, C. J. Clarke, J. E. Pringle, J. S. Ulvestad, and R. R. J. Antonucci. Jet Directions in Seyfert Galaxies. *ApJ,*, 537(1):152–177, July 2000.

[58] Marek A. Abramowicz and P. Chris Fragile. Foundations of Black Hole Accretion Disk Theory. *Living Reviews in Relativity*, 16(1):1, January 2013.

[59] X. Chen, M. A. Abramowicz, J.-P. Lasota, R. Narayan, and I. Yi. Unified description of accretion flows around black holes. *ApJ,*, 443:L61–L64, April 1995.

[60] R. Narayan, R. Mahadevan, and E. Quataert. *Advection-dominated accretion around black holes*, pages 148–182. 2010.

[61] Ramesh Narayan and Jeffrey E. McClintock. Advection-dominated accretion and the black hole event horizon. *New A Rev.,*, 51(10-12):733–751, May 2008.

[62] Charles F. Gammie, Jonathan C. McKinney, and Gábor Tóth. HARM: A Numerical Scheme for General Relativistic Magnetohydrodynamics. *ApJ,*, 589(1):444–457, May 2003.

[63] José A. Font. Numerical Hydrodynamics and Magnetohydrodynamics in General Relativity. *Living Reviews in Relativity*, 11(1):7, September 2008.

[64] Steven A. Balbus and John F. Hawley. Instability, turbulence, and enhanced transport in accretion disks. *Reviews of Modern Physics*, 70(1):1–53, January 1998.

[65] Scott C. Noble, Julian H. Krolik, and John F. Hawley. Direct Calculation of the Radiative Efficiency of an Accretion Disk Around a Black Hole. *ApJ,*, 692(1):411–421, February 2009.

[66] Steven A. Balbus and John F. Hawley. A Powerful Local Shear Instability in Weakly Magnetized Disks. I. Linear Analysis. *ApJ,*, 376:214, July 1991.

[67] John F. Hawley and Julian H. Krolik. Magnetically Driven Jets in the Kerr Metric. *ApJ,*, 641(1):103–116, April 2006.

[68] Shigenobu Hirose, Julian H. Krolik, Jean-Pierre De Villiers, and John F. Hawley. Magnetically Driven Accretion Flows in the Kerr Metric. II. Structure of the Magnetic Field. *ApJ,*, 606(2):1083–1097, May 2004.

[69] Jonathan C. McKinney. General relativistic magnetohydrodynamic simulations of the jet formation and large-scale propagation from black hole accretion systems. *MNRAS,*, 368(4):1561–1582, June 2006.

[70] Kristen A. Miller and James M. Stone. The Formation and Structure of a Strongly Magnetized Corona above a Weakly Magnetized Accretion Disk. *ApJ,*, 534(1):398–419, May 2000.

[71] M. Liska, A. Tchekhovskoy, and E. Quataert. Large-scale poloidal magnetic field dynamo leads to powerful jets in GRMHD simulations of black hole accretion with toroidal field. *MNRAS,*, 494(3):3656–3662, May 2020.

[72] Adam Ingram and Chris Done. A physical model for the continuum variability and quasi-periodic oscillation in accreting black holes. *MNRAS,*, 415(3):2323–2335, August 2011.

[73] P. Chris Fragile and Peter Anninos. Hydrodynamic Simulations of Tilted Thick-Disk Accretion onto a Kerr Black Hole. *ApJ,*, 623(1):347–361, April 2005.

[74] Ken B. Henisey, Omer M. Blaes, and P. Chris Fragile. Variability from Non-axisymmetric Fluctuations Interacting with Standing Shocks in Tilted Black Hole Accretion Disks. *ApJ,*, 761(1):18, December 2012.

[75] Jason Dexter and P. Chris Fragile. Observational Signatures of Tilted Black Hole Accretion Disks from Simulations. *ApJ,*, 730(1):36, March 2011.

[76] Christopher J. Nixon and Andrew R. King. Broken discs: warp propagation in accretion discs. *MNRAS,*, 421(2):1201–1208, April 2012.

[77] Chris Nixon, Andrew King, Daniel Price, and Juhan Frank. Tearing up the Disk: How Black Holes Accrete. *ApJ,*, 757(2):L24, October 2012.

[78] M. T. P. Liska, K. Chatterjee, D. Issa, D. Yoon, N. Kaaz, A. Tchekhovskoy, D. van Eijnatten, G. Musoke, C. Hesp, V. Rohoza, S. Markoff, A. Ingram, and M. van der

Klis. H-AMR: A New GPU-accelerated GRMHD Code for Exascale Computing with 3D Adaptive Mesh Refinement and Local Adaptive Time Stepping. *ApJS,*, 263(2):26, December 2022.

[79] M. Liska, C. Hesp, A. Tchekhovskoy, A. Ingram, M. van der Klis, and S. Markoff. Formation of precessing jets by tilted black hole discs in 3D general relativistic MHD simulations. *MNRAS,*, 474(1):L81–L85, February 2018.

[80] M. Liska, C. Hesp, A. Tchekhovskoy, A. Ingram, M. van der Klis, S. B. Markoff, and M. Van Moer. Disc tearing and Bardeen-Petterson alignment in GRMHD simulations of highly tilted thin accretion discs. *MNRAS,*, 507(1):983–990, October 2021.

[81] G. Musoke, M. Liska, O. Porth, Michiel van der Klis, and Adam Ingram. Disc tearing leads to low and high frequency quasi-periodic oscillations in a GRMHD simulation of a thin accretion disc. *MNRAS,*, 518(2):1656–1671, January 2023.

[82] P. Varniere, F. Casse, and F. H. Vincent. Rossby wave instability and high-frequency quasi-periodic oscillations in accretion discs orbiting around black holes. *A&A,*, 625:A116, May 2019.

[83] Brooks E. Kinch, Jeremy D. Schnittman, Timothy R. Kallman, and Julian H. Krolik. Fe Kα Profiles from Simulations of Accreting Black Holes. *ApJ,*, 826(1):52, July 2016.

[84] Jeremy D. Schnittman and Julian H. Krolik. A Monte Carlo Code for Relativistic Radiation Transport around Kerr Black Holes. *ApJ,*, 777(1):11, November 2013.

[85] Brooks E. Kinch, Jeremy D. Schnittman, Scott C. Noble, Timothy R. Kallman, and Julian H. Krolik. Spin and Accretion Rate Dependence of Black Hole X-Ray Spectra. *ApJ,*, 922(2):270, December 2021.

[86] C. D. Levermore. Relating Eddington factors to flux limiters. *J. Quant. Spec. Radiat. Transf.,*, 31(2):149–160, February 1984.

[87] Aleksander Sądowski, Ramesh Narayan, Alexander Tchekhovskoy, and Yucong Zhu. Semi-implicit scheme for treating radiation under M1 closure in general relativistic conservative fluid dynamics codes. *MNRAS,*, 429(4):3533–3550, March 2013.

[88] Aleksander Sądowski. Thin accretion discs are stabilized by a strong magnetic field. *MNRAS,*, 459(4):4397–4407, July 2016.

[89] Danilo Morales Teixeira, Mark J. Avara, and Jonathan C. McKinney. General relativistic radiation magnetohydrodynamic simulations of thin magnetically arrested discs. *MNRAS,*, 480(3):3547–3561, November 2018.

[90] Brandon Curd and Ramesh Narayan. GRRMHD simulations of MAD accretion discs declining from super-Eddington to sub-Eddington accretion rates. *MNRAS,*, 518(3):3441–3461, January 2023.

[91] M. T. P. Liska, G. Musoke, A. Tchekhovskoy, O. Porth, and A. M. Beloborodov. Formation of Magnetically Truncated Accretion Disks in 3D Radiation-transport Two-temperature GRMHD Simulations. *ApJ,*, 935(1):L1, August 2022.

[92] James M. Bardeen and Jacobus A. Petterson. The Lense-Thirring Effect and Accretion Disks around Kerr Black Holes. *ApJ,*, 195:L65, January 1975.

[93] H. Krawczynski. Tests of General Relativity in the Strong-gravity Regime Based on X-Ray Spectropolarimetric Observations of Black Holes in X-Ray Binaries. *ApJ,*, 754:133, August 2012.

[94] Janie K. Hoormann, Banafsheh Beheshtipour, and Henric Krawczynski. Testing general relativity's no-hair theorem with x-ray observations of black holes. *Phys. Rev. D,*, 93(4):044020, Feb 2016.

[95] Banafsheh Beheshtipour, Henric Krawczynski, and Julien Malzac. The X-Ray Polarization of the Accretion Disk Coronae of Active Galactic Nuclei. *ApJ,*, 850(1):14, Nov 2017.

[96] H. Krawczynski, G. Chartas, and F. Kislat. The Effect of Microlensing on the Observed X-Ray Energy Spectra of Gravitationally Lensed Quasars. *ApJ,*, 870(2):125, Jan 2019.

[97] Henric Krawczynski and George Chartas. Modeling of the Microlensed Fe Kα Emission from the Quasar RX J1131-1231. In *AAS/High Energy Astrophysics Division #16*, AAS/High Energy Astrophysics Division, page 106.16, Aug 2017.

[98] G. Chartas, H. Krawczynski, Lukas Zalesky, C. Kochanek, X. Dai, C. Morgan, and A. Mosquera. Measuring the innermost stable circular orbits of supermassive black holes. *The Astrophysical Journal*, 837, 09 2016.

[99] Quincy Abarr and Henric Krawczynski. The Polarization of X-Rays from Warped Black Hole Accretion Disks. *ApJ,*, 889(2):111, February 2020.

[100] Quincy Abarr and Henric Krawczynski. The Iron Line Profile from Warped Black Hole Accretion Disks. *ApJ,*, 906(1):28, January 2021.

[101] M.A. Abramowicz, B. Czerny, J.P. Lasota, and Ewa Szuszkiewicz. Slim accretion disks. *Astrophys. J.*, 332, 09 1988.

[102] Wei-Min Gu. Radiation Pressure-supported Accretion Disks: Vertical Structure, Energy Advection, and Convective Stability. *ApJ,*, 753(2):118, July 2012.

[103] Bozena Czerny. Slim Accretion Disks: Theory and Observational Consequences. *Universe*, 5(5):131, May 2019.

[104] Shafqat Riaz, Dimitry Ayzenberg, Cosimo Bambi, and Sourabh Nampalliwar. Reflection spectra of thick accretion disks. *arXiv e-prints*, page arXiv:1908.04969, Aug 2019.

[105] Corbin Taylor and Christopher S. Reynolds. Exploring the Effects of Disk Thickness on the Black Hole Reflection Spectrum. *ApJ,*, 855(2):120, Mar 2018.

[106] Jiachen Jiang, Askar B. Abdikamalov, Cosimo Bambi, and Christopher S. Reynolds. Black hole spin measurements based on a thin disc model with finite thickness - I. An example study of MCG-06-30-15. *MNRAS,*, 514(3):3246–3259, August 2022.

[107] Corbin Taylor and Christopher S. Reynolds. X-Ray Reverberation from Black Hole Accretion Disks with Realistic Geometric Thickness. *ApJ,*, 868(2):109, December 2018.

[108] Corbin Taylor and Christopher S. Reynolds. X-Ray Reverberation from Black Hole Accretion Disks with Realistic Geometric Thickness. *ApJ,*, 868(2):109, Dec 2018.

[109] J. R. Cash and Alan H. Karp. A variable order runge-kutta method for initial value problems with rapidly varying right-hand sides. *ACM Trans. Math. Softw.*, 16(3):201â222, sep 1990.

[110] Toshiya Shimura and Fumio Takahara. On the Spectral Hardening Factor of the X-Ray Emission from Accretion Disks in Black Hole Candidates. *ApJ,*, 445:780, June 1995.

[111] Alexander Tchekhovskoy. HARMPI: 3D massively parallel general relativictic MHD code. Astrophysics Source Code Library, record ascl:1912.014, December 2019.

[112] M. J. Berger and P. Colella. Local Adaptive Mesh Refinement for Shock Hydrodynamics. *Journal of Computational Physics*, 82(1):64–84, May 1989.

[113] Dinshaw S. Balsara. Divergence-Free Adaptive Mesh Refinement for Magnetohydrodynamics. *Journal of Computational Physics*, 174(2):614–648, December 2001.

[114] L. G. Fishbone and V. Moncrief. Relativistic fluid disks in orbit around Kerr black holes. *ApJ,*, 207:962–976, August 1976.

[115] J. Frank, A. King, and D. J. Raine. *Accretion Power in Astrophysics: Third Edition*. January 2002.

[116] James B. Hartle. *Gravity : an introduction to Einstein's general relativity*. 2003.

[117] Richard P. Nelson and John C. B. Papaloizou. Hydrodynamic simulations of the Bardeen-Petterson effect. *MNRAS,*, 315(3):570–586, July 2000.

[118] M. A. Nowak and D. E. Lehr. Stable oscillations of black hole accretion discs. In M. A. Abramowicz, G. Björnsson, and J. E. Pringle, editors, *Theory of Black Hole Accretion Disks*, pages 233–253, January 1998.

[119] G. Lodato and J. E. Pringle. The evolution of misaligned accretion discs and spinning black holes. *MNRAS,*, 368(3):1196–1208, May 2006.

[120] R. P. Kerr and A. Schild. Republication of: A new class of vacuum solutions of the Einstein field equations. *General Relativity and Gravitation*, 41(10):2485–2499, October 2009.

[121] G. C. Debney, R. P. Kerr, and A. Schild. Solutions of the Einstein and Einstein-Maxwell Equations. *Journal of Mathematical Physics*, 10(10):1842–1854, October 1969.

[122] Herbert Balasin and Herbert Nachbagauer. Distributional energy–momentum tensor of the Kerr–Newman spacetime family. *Classical and Quantum Gravity*, 11(6):1453–1461, June 1994.

[123] J. M. Bardeen. Properties of Black Holes Relevant to Their Observation (invited Paper). In C. Dewitt-Morette, editor, *Gravitational Radiation and Gravitational Collapse*, volume 64, page 132, January 1974.

[124] Tim Johannsen and Dimitrios Psaltis. Metric for rapidly spinning black holes suitable for strong-field tests of the no-hair theorem. *Phys. Rev. D,*, 83(12):124015, June 2011.

[125] Akshay K. Kulkarni, Robert F. Penna, Roman V. Shcherbakov, James F. Steiner, Ramesh Narayan, Aleksander Sä Dowski, Yucong Zhu, Jeffrey E. McClintock, Shane W. Davis, and Jonathan C. McKinney. Measuring black hole spin by the continuum-fitting method: effect of deviations from the Novikov-Thorne disc model. *MNRAS,*, 414(2):1183–1194, June 2011.

[126] James M. Bardeen, William H. Press, and Saul A. Teukolsky. Rotating Black Holes: Locally Nonrotating Frames, Energy Extraction, and Scalar Synchrotron Radiation. *ApJ,*, 178:347–370, December 1972.

[127] I. M. George and A. C. Fabian. X-ray reflection from cold matter in Active Galactic Nuclei and X-ray binaries. *MNRAS,*, 249:352, March 1991.

[128] James C. A. Miller-Jones, Arash Bahramian, Jerome A. Orosz, Ilya Mandel, Lijun Gou, Thomas J. Maccarone, Coenraad J. Neijssel, Xueshan Zhao, Janusz Ziółkowski, Mark J. Reid, Phil Uttley, Xueying Zheng, Do-Young Byun, Richard Dodson, Victoria Grinberg, Taehyun Jung, Jeong-Sook Kim, Benito Marcote, Sera Markoff, María J.

Rioja, Anthony P. Rushton, David M. Russell, Gregory R. Sivakoff, Alexandra J. Tetarenko, Valeriu Tudose, and Joern Wilms. Cygnus X-1 contains a 21-solar mass black hole—Implications for massive star winds. *Science*, 371(6533):1046–1049, March 2021.

[129] R. P. Fender, S. T. Garrington, D. J. McKay, T. W. B. Muxlow, G. G. Pooley, R. E. Spencer, A. M. Stirling, and E. B. Waltman. MERLIN observations of relativistic ejections from GRS 1915+105. *MNRAS,*, 304(4):865–876, April 1999.

[130] Daniela Huppenkothen, Matteo Bachetti, Abigail L. Stevens, Simone Migliari, Paul Balm, Omar Hammad, Usman Mahmood Khan, Himanshu Mishra, Haroon Rashid, Swapnil Sharma, Evandro Martinez Ribeiro, and Ricardo Valles Blanco. Stingray: A Modern Python Library for Spectral Timing. *ApJ,*, 881(1):39, August 2019.

[131] Daniela Huppenkothen, Matteo Bachetti, Abigail Stevens, Simone Migliari, Paul Balm, Omar Hammad, Usman Mahmood Khan, Himanshu Mishra, Haroon Rashid, Swapnil Sharma, Evandro Martinez Ribeiro, and Ricardo Valles Blanco. stingray: A modern python library for spectral timing. *Journal of Open Source Software*, 4(38):1393, 2019.

[132] Adam Ingram, Thomas J. Maccarone, Juri Poutanen, and Henric Krawczynski. Polarization Modulation from Lense-Thirring Precession in X-Ray Binaries. *ApJ,*, 807(1):53, July 2015.